The Electronic Structures of Cobalt-containing Diatomic Molecules

by

Jingfei Yao

A thesis
presented to the University of Waterloo
in fulfilment of the
thesis requirement for the degree of
Master of Science
in
Chemistry

Waterloo, Ontario, Canada, 2016

Author's Declaration

I hereby declare that I am the sole author of this thesis. This is a true copy of the thesis, including any required final revisions, as accepted by my examiners.

I understand that my thesis may be made electronically available to the public.

Jingfei Yao

Abstract

Theoretical investigations of the electronic structures of several metal-containing diatomic species (*i.e.,* Co_2^+, Co^+•RG (RG=He, Ar, Kr), Au^+Ar, and Ag^+Ar) have been conducted. In this study, two categories of methods have been utilized for the calculations: single reference methods, including density functional theory (DFT, TD-DFT) and coupled cluster theory (CCSD, EOM-CCSD), and multireference methods, such as multireference configuration interaction (MRCI) and multireference equation-of-motion coupled cluster theory (MREOM-CCSD).

Preliminary results for the potential energy curves (PBEs) of Co_2^+ as calculated with DFT and EOM-CCSD yields two anomalous results: discontinuous PECs and negative excitation energies. These two results indicate that single reference methods are not adequate for description of the Co_2^+ system, and that multireference methods should be employed. MRCI calculations which employed the Davidson correction remedied the negative excitation energies issue, but the PECs remained discontinuous at this level of theory. The MREOM-CCSD method produced exclusively positive excitation energies and continuous PECs. The dissociation thresholds (D_0) for the ground states of Co^+•Ar, Co^+•Kr, Ag^+•Ar, and Au^+•Ar were calculated to be 0.3872 eV, 0.5443 eV, 0.1931 eV, and 0.3696 eV, respectively by MREOM-T|T^+|SXD/Def2-TZVPPD. These calculations included corrections for spin-orbit coupling (SOC), basis set superposition error (BSSE), and zero-point energy (ZPE). However, the theoretically calculated dissociation thresholds of Co^+•Ar and Co^+•Kr are approximately 0.11 eV lower than the experimentally determined values of 0.5097 eV and 0.6701 eV, respectively. These discrepancies could due to the unsuitable selection of the complete active space (CAS) and/or the basis set in the calculation, or the validity of the experimental measurement.

Acknowledgements

I would firstly like acknowledge my supervisor Dr. W. Scott Hopkins for the chance of graduate study in his group and all his help, support and guidance during my two years of graduate studies. Thanks as well to Dr. Marcel Nooijen for all his guidance and valuable suggestions, which helped me a lot during this research. I would also like to thank Dr. Robert Le Roy for his help and support in the LEVEL program.

I would like to show my thanks to the committee members - Dr. W. Scott Hopkins, Dr. Marcel Nooijen and Dr. Germán Sciaini - for guiding me through this thesis process and for the reading and editing this report.

Furthermore, I would like to show my gratitude to all Hopkins group members and all the friends I met and worked with. Thanks Ce Zhou, Stephen Walker and Patrick Carr for help with writing my thesis.

Last but not Least, I would like to show my appreciation to my family for their continuing support.

Table of Content

List of Figures

List of Tables

List of Abbreviations

Basis Set Superposition Error	BSSE
Coupled Cluster	CC
Coupled Cluster with Single and Double excitations	CCSD
Configuration Interaction	CI
Configuration Interaction with Single excitation	CIS
Configuration Interaction with Double excitation	CID
Configuration Interaction with Single and Double excitations	CISD
Complete Active Space	CAS
Complete Active Space Self-Consistent Field	CASSCF
Davidson Correction	DC
Density Functional Theory	DFT
Diagonalization Space	DS
Equation of Motion Coupled Cluster	EOM-CC
Excited State	ES
Gaussian Type Orbitals	GTOs
Generalized Gradient Approximation	GGA
Ground State	GS
Hartree Fock	HF
Kinetic Energy	KE
Local Density Approximation	LDA

Micro-Channel Plate Detector	MCP
Multireference	MR
Multireference Equation of Motion Coupled Cluster	MR-EOM-CC
MREOM with excitation operators T,S,X,D	MREOM-T|SXD
Multireference Configuration Interaction	MRCI
MRCI with Davidson-type extensivity correction	MRCI+Q
National Institute of Stands and Technology	NIST
Potential Energy Curves	PECs
Rare Gas	RG
Restricted Active Space	RAS
Restricted Active Space Self-Consistent Field	RASSCF
Slater Type Orbitals	STOs
Self-Consistent Field	SCF
Single Reference	SR
Spin-orbit Coupling	SOC
Split Valance Basis set	SVBS
Time-Dependent Density Functional Theory	TD-DFT
Velocity Map Image	VMI
Zero Point Energy	ZPE

Chapter 1: Introduction

Exploration of the electronic structure of transition metal-containing species is challenging due to the high density of states and significant spin-orbit coupling interactions[1]. This complexity of the electronic structures of transition metal-containing molecules leads to rich physicochemical properties, and therefore, applications in a variety of fields. Among these transition metal-containing species, cobalt-containing complexes can be used as pigments[2], materials for energy storage[3], petrochemical catalysts[4], and magnetic materials[5]. All of these applications make cobalt chemistry an attractive subject for experimentalists and theoreticians.

1.1 Cobalt Containing Dimer Systems

Owing to the complexity of the electronic structures of cobalt-containing species, research has predominantly focused on small molecules such as Co_2^+ and Co^+•RG (RG=Ar, Kr) diatomic molecules. The previous experimental exploration of Co_2^+ is illustrated on section 1.1.1 while the investigation of Co^+•RG is described in section 1.1.2.

1.1.1 Co_2^+ System

Early investigations by Russon and co-workers measured the dissociation energy of Co_2^+ spectroscopically[6]. They used a laser to vaporize a cobalt target, thereby forming ions, which were transported using an argon seeded helium carrier gas. Metal clusters were formed when the ions passed through a high-pressure collision region before expansion into a low-pressure environment. The resulting metal cluster beam, which consisted of neutral, cationic, and anionic species, was then sent through a two-dimensional turning quadrupole for mass selection. The selected ions were then accelerated by a Wiley-McLaren time-of-flight source into a photodissociation chamber. A pulsed dye laser was then used to photodissociate the mass-selected species (e.g., Co_2^+) and the Co^+ signal was measured by a microchannel plate (MCP)[6]. Figure 1 shows photofragmentation yield as a function of dissociation laser wavenumber[6]. A sharp photodissociation threshold, assigned as the D_0'' threshold, is observed for Co_2^+ at 22300.0±5.0 cm^{-1} (2.765±0.001eV)[6]. This assignment assumes that the Co_2^+ is excited from the $v''=0$ state, and that after dissociation, ground state products are formed.

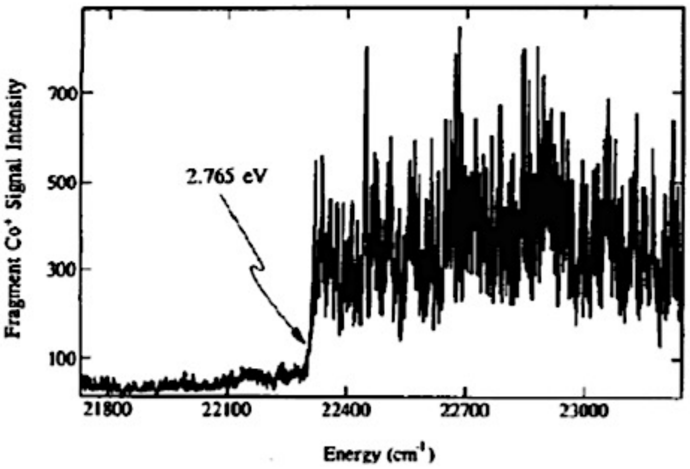

Figure 1: The dissociation threshold of Co_2^+. [6]

1.1.2 Co^+•RG (RG=Ar, Kr) system

The photofragmentation excitation spectra of Co^+•RG (RG= Ar, Kr) were measured by Brucat and co-workers in the 13500-18000 cm^{-1} region using the mass-selected photodissociation method[7]. They generated cobalt rare-gas diatomic ions: Co^+•Ar and Co^+•Kr in a laser-driven-plasma supersonic-expansion ion source (Figure 2)[8]. This supersonic expansion, which occurs in a He carrier gas that is seeded with 1% Ar (Kr), cools the ions, facilitates clustering, and produces the ground state (v=0) diatomic molecules (among other species). These ions were then accelerated and mass-selected by a time-of-flight (TOF) mass spectrometer. Before the selected Co^+•RG species entered to the electrostatic sector, a tunable Nd^{+3}:YAG pumped dye laser was used to induce photodissociation. The resulting Co^+ signal was measured and amplified by a microchannel plate (MCP) electron multiplier. Thus, photofragmentation excitation spectra, which is the relative fragmentation yield as a function of laser frequency, were obtained.[8]

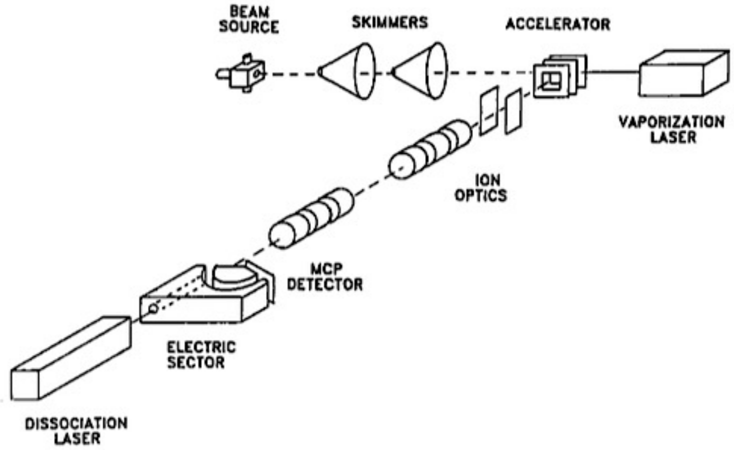

Figure 2. Sketch of the experimental apparatus used in Brucat's study[8]

The photofragmentation excitation spectrum of Co^+•Kr is shown in Figure 3. The spectrum exhibits sharp vibronic features, which correspond to three vibronic band systems of Co^+•Kr: $X(v = 0) \rightarrow A$, $X(v = 0) \rightarrow B$, and $X(v = 0) \rightarrow C$. Co^+•Ar exhibits an electronic spectrum that is very similar to that of Co^+•Kr.[8]

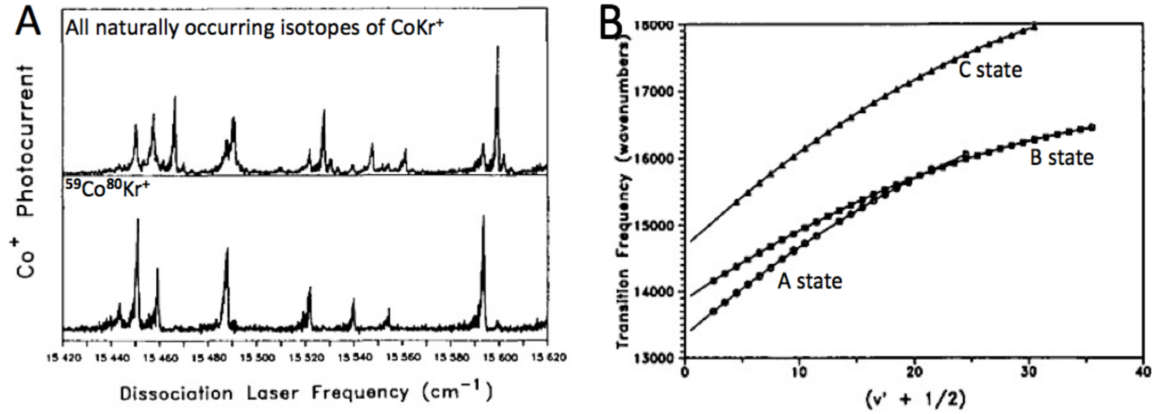

Figure 3. (A)The 15420 - 15620 cm^{-1} region of the electronic spectrum of Co^{+}•Kr. The isotopic shifts in the spectra can be used to deduce the absolute vibrational number. (B) The observed vibrational band origins of $X(v = 0) \rightarrow A$, $X(v = 0) \rightarrow B$, and $X(v = 0) \rightarrow C$ plotted as a function of excited state vibrational quantum number. The asymptote gives the dissociation threshold.[8]

To model the vibrational energy levels of a diatomic molecule, the potential $V(r) = D - C_n/r^n$ near the dissociation limit can be formulated as:

$$[D - E(v)]^{(n-2)/2n} = [(n-2)/2n](v_D - v)K \qquad \text{Equation 1}$$

where D is the dissociation energy, $E(v)$ is the energy of vth vibrational level, v_D is the maximum vibrational quantum level allowed, n is a limiting long-range inverse-power of interactions, and K is a combination of fundamental constants.

Equation 1 can be re-written as follows:[8]

$$D - E(v) = \left(\frac{(n-2)K}{2n}\right)^{\frac{2n}{n-2}} (v_D - v)^{\frac{2n}{n-2}} \qquad \text{Equation 2}$$

Taking the derivative of the vibrational energy with respect to the vibrational quantum number yields,

$$-\frac{dE_v}{dv} = \left(\frac{(n-2)K}{2n}\right)^{\frac{2n}{n-2}} \cdot \frac{2n}{n-2} \cdot (v_D - v)^{\frac{n+2}{n-2}} \cdot (-1) \qquad \text{Equation 3}$$

where the $-\frac{dE_v}{dv}$ approximately equals to ΔG_v, the vibrational level spacing:

$$\Delta G_v = [E(v+1) - E(v-1)]/2 \qquad \text{Equation 4}$$

Elimination of the $(v_D - v)$ term by substituting Equation 1 into Equation 3 yields:

$$\Delta G_v = \left(\frac{(n-2)K}{2n}\right)^{\frac{2n}{n-2}} \cdot \frac{2n}{n-2}\left(\frac{2n}{(n-2)K}\right) \cdot [D - E(v)]^{(n+2)/2n} \qquad \text{Equation 5}$$

Using this approach, the n value is determined to be 4 for the Co^+•Ar system. By substituting n=4 to Equation 5, simplifying and raising both sides of the equation to the power of 4/3, we arrive at:[8]

$$\Delta G_v{}^{4/3} = [D - E(v)]K^{4/3} \qquad \text{Equation 6}$$

Thus, a plot of $\Delta G_v{}^{4/3}$ versus transition frequency near dissociation can be used to extrapolate D of each state for Co^+•Ar system (see Figure 4). This treatment yields D_0 = 1.9531 eV for the A state, D_0 = 1.9131 eV for the B state, and D_0 = 2.1523 eV for the C state.[8] The dissociation energy of ground state can then be calculated from the observed dissociation limits and the known energy levels of the Co^+.[9]

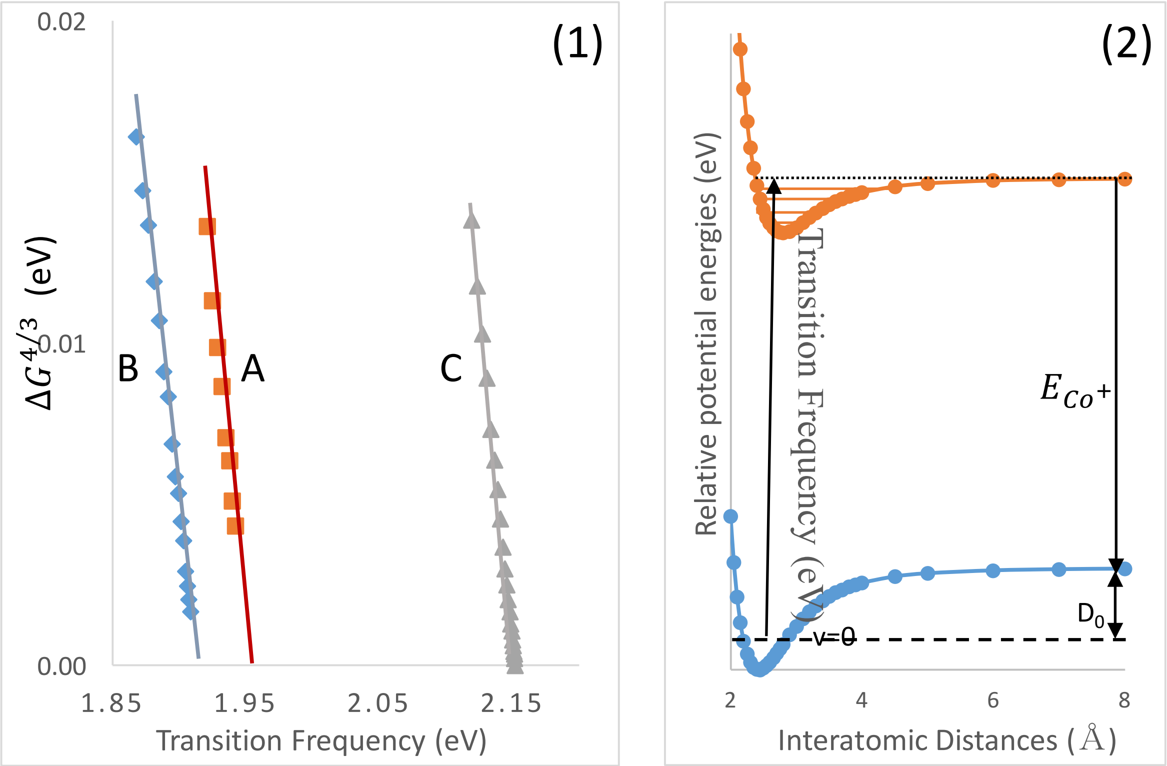

Figure 4. (1) is a plot of the derivative of the vibrational energies with respect to vibrational index to the 4/3 power versus transition frequency for A, B, and C excited states of $Co^+ \cdot Ar$.(2) is a schematic diagram showing how one can calculate the ground state dissociation energy of $Co^+ \cdot Ar$ from the excited state dissociation threshold and the internal energy of the Co^+ cation.[9]

As can be seen in Figure 4(1), the x-intercepts of the A, B, and C trend lines are dissociation thresholds for the A, B, C states of Co^+•Ar. These correlate with the separated atom limits associated with the a^1D_2, b^3F_2, and a^3P_2 states of Co^+, which occur at internal energies of 1.4446 eV, 1.4037 eV, and 1.6441 eV, respectively. Thus, one arrives at a ground state dissociation energy of D_0(Co^+•Ar) = 0.5097 eV (see Table 1). Similar treatment of Co^+•Kr yields D_0(Co^+•Kr) = 0.6695 eV.[8]

Table 1. The dissociation thresholds for the excited states of $Co^+ \cdot Ar$, the corresponding internal excitations of Co^+, the resulting ground state dissociation energy of $Co^+ \bullet Ar$.[8, 9]

$Excited\ states\ of\ Co^+ \cdot Ar$	D_0(eV)	E_{Co^+}(eV)	$E_{G.S.:X^3\Delta_3}(eV)$
A ($A^1\Delta_2$) : $Co^+(a^1D_2) + Ar(^1S)$	1.9531	1.4446	0.5085
B : $Co^+(b^3F_2) + Ar(^1S)$	1.9131	1.4037	0.5094
C : $Co^+(a^3P_2) + Ar(^1S)$	2.1523	1.6441	0.5082

1.2 Computational Investigation on Small Transition Metal Containing Systems

The calculations of the electronic structure of transition metal clusters (even dimers) presents a challenge for computational chemistry because of the significant multireference character of these systems.[10] This is demonstrated in Table 2, where C_0^2, which is the weight of the leading configuration in the CASSCF wavefunction, represents the multireference character of several homonuclear transition metal diatomic molecules. In general, a molecular system whose C_0^2 is less than 0.90 is regarded to possess high multireference character.[11]

Table 2. C_0^2 values for first row transition metal homodimers as calculated at the CASSCF/cc-PVTZ-DK level of theory.[10]

Molecules	Sc_2	Ti_2	V_2	Cr_2	Mn_2	Fe_2	Co_2	Ni_2	Cu_2
Dominant state in the ground state	$^5\Sigma_u^-$	$^1\Delta_g$	$^3\Sigma_g^-$	$^1\Sigma_g^+$	$^{11}\Pi_u$	$^7\Delta_u$	$^5\Delta_g$	$^3\Sigma_g^-$	$^1\Sigma_g^+$
C_0^2	0.500	0.793	0.706	0.614	0.881	0.482	0.513	0.518	0.969

Many efforts have been taken to solve the multireference calculation of transition metals. For example, the reaction energy of Co^+ + H_2O obtained from multireference treatment is more accurate than that obtained from single reference calculations (see Table 3).[12] This is also demonstrated in calculations of TlH, where r_e and D_e are in much better agreement with experimentally determined values when calculated using multireference methods.[13]

Table 3. A comparison of molecular properties for two transition metal systems as calculated using multireference and single reference methods.[12, 13]

Reaction: $Co^+ + H_2O \longrightarrow CoOH_2^+$

Methods	Reaction Energies (kcal/mol)
B3LYP/cc-PVTZ	-40.4
MR-SDCI(+Q)/cc-PVTZ	-38.2
Experiment	-38.5

TlH dimer

	R_e (Å)	ω_e (cm^{-1})	D_e (eV)
B3LYP/6-311++G(3df)[b]	1.92	1324	3.688
GRECP-MR-SDCI(+Q)[a]/ [4, 4, 4, 3, 2]	1.870	1420	2.049
Experiment	1.872	1391	2.06

a: Generalized Relativistic Effective Core Potential- Multireference Single- and Double-excitation Configuration Interaction, and [4,4,4,3,2] is a user-defined basis set.[13]

b: This single reference calculation is done in this work.

Compared to open-shell systems, the ground state multireference character of close-shell systems near equilibrium is not significant. However, multireference treatment of excited states and near-threshold geometries might still be necessary for closed-shell species. For example, Table 4 gives the results of multireference calculations that were conducted by

Huntington for a series of closed-shell transition metal complexes.[14] In general, multireference methods out-perform single reference calculations of electronic excitation energies.

Table 4. The lowest excitation energies (eV) for five transition metal complexes.[14]

Molecules	MR-EOM/ Def2-SVP	MR-EOM/ Def2-TZVPP	EOM-CCSD(T)/ Wachters+F for TM while cc-PVDZ for others	Experiment
$Ni(CO)_4$	5.09	5.08	5.01	4.6
$Fe(CO)_5$	4.90	4.87	5.17	4.4
$Cr(CO)_6$	4.97	4.91	4.95	4.4
ferrocene	2.70	2.71	3.06	2.81
CpNiNO	2.71	2.81	2.93	2.68

Chapter 2: Single-Reference Calculations of Cobalt-containing Diatomic Molecules

2.1 Introduction

Ab initio calculations have become an important augmentation to experimental work in modern chemistry research. Theoretical calculations have several advantages over experimentation. First of all, calculations can be conducted without concern for unintended environmental, health, or safety effects. In addition, the initial conditions of calculations are entirely user-defined, giving tremendous flexibility to the construction of the molecule and its environment. Moreover, computational studies are (usually) relatively inexpensive in comparison with experiment. Despite these advantages, deficiencies still exist. For example, the validity and reliability of a computer simulation usually needs to be examined in the context of experimental results. Other drawbacks are associated with computational resources such as memory, the number of available processors, and the amount of time the calculation requires. This computational time can be the most expensive drawback because of the way that it scales with the number of orbitals included in the basis set. If N is the number of orbitals, the total amount of CPU time required to do the calculation scales as N^6 for a CCSD calculation.

The goal of *ab initio* calculations is to solve the Schrödinger equation, the fundamental model of quantum mechanics, using numerical methods. There are three major types of *ab initio* electronic structure calculation methods: Hartree-Fock (HF) methods, post-HF methods [*e.g.,* configuration interaction-(CI), coupled cluster with single and double excitations-(CCSD)], and multireference methods (*e.g.,* multireference configuration interaction-MRCI and multireference coupled cluster-MRCC). These methods describe the total wavefunction of a system with a slater determinant. Density functional theory (DFT), which describes the wavefunction of the system using its electron density, is also (usually) considered an *ab initio* method, even though some parameters in the functionals are derived from empirical data.

In this chapter, the electronic states of Co_2^+ are explored using single reference DFT and CCSD methods. In section 2.2, the fundamental theory of a basis set (section 2.2.1), HF (section 2.2.2), DFT (section 2.2.3), CI (section 2.2.4) and CC (section 2.2.5) methods are summarized, respectively. The computational details and results are shown in sections 2.3 and 2.4, and concluding remarks follow in section 2.5.

2.2 Theory

2.2.1 Basis set

Ab initio calculations attempt to solve the the Schrödinger equation:

$$\hat{H}\Psi = E\Psi \qquad \text{Equation 7}$$

where $\hat{H}$ is the Hamiltonian operator, E is the associated energy, and Ψ is the associated wavefunction. Except for a few cases (*e.g.*, hydrogen system, particle-in-a-box, and harmonic oscillator), the Schrödinger equation cannot be solved exactly. Instead, the electron distributions in atoms and molecules are approximated with linear combinations of a set of spatial basis functions (φ_i). This combination of spatial functions, called the basis set, is described by:[15]

$$\Psi_i(\vec{r}) = \sum_i C_i \varphi_i(\vec{r}) \qquad \text{Equation 8}$$

where Ψ_i: atomic orbitals φ_i: basis functions C_i: weighting coefficient

To fully describe a quantum system, the spin of the electron(s) must also be considered. This can be represented in two orthonormal functions, $\alpha(\omega)$(*a.k.a.*, spin up) and $\beta(\omega)$ (*a.k.a.,* spin down).[15] Thus, a new wavefunction called the spin orbital wavefunction (χ_i), which combines the spatial distribution and the electron spin, can be constructed: [15]

$$\chi_i(\vec{r}) = \begin{cases} \varphi_i(\vec{r})\alpha(\omega) \\ \varphi_i(\vec{r})\beta(\omega) \end{cases} \qquad \text{Equation 9}$$

where χ_i are the spin orbitals, φ_i is the spatial wavefunction, $\alpha(\omega)$ are the spin-up orbitals, $\beta(\omega)$ are the spin-down orbitals. Consequently, the wavefunction of a system as described in Equation 8 is better represented by including the spin orbitals:

$$\Psi_i(\vec{r}) = \sum_i c_i\, \chi_i(\vec{r}) \qquad \text{Equation 10}$$

2.2.1.1 Slater-type orbitals and Gaussian-type orbitals

Among many types of basis sets, two have come to dominate the area of *ab initio* molecular calculations; Slater-type-orbitals (STOs) and Gaussian-type-orbitals (GTOs). Slater-type orbitals (STOs) have the form[16]:

$$\chi(\vec{r}) = \chi_{(\zeta,n,l,m;r,\theta,\phi)}(\vec{r}) = N r^{n-1} e^{-\zeta r} Y_{lm}(\theta,\phi) \qquad \text{Equation 11}$$

where *N* is a normalization constant, ζ is the orbital exponent, r, θ, ϕ are spherical coordinates, and n, l, m are the principal, angular, and magnetic quantum numbers; respectively. In this equation, the $Y_{lm}(\theta, \phi)$ term are the spherical harmonics and the $r^{n-1}e^{-\zeta r}$ term describes the radial distribution of the function. As is shown in Figure 5, the principle quantum number, n, is associated with size and number of radial nodes. whereas the ζ introduces flexibility to control how diffuse the orbital is; a large exponent yields a “tight” (small radius) orbital, whereas a small exponent yields a more diffuse (large radius) orbital.[17]

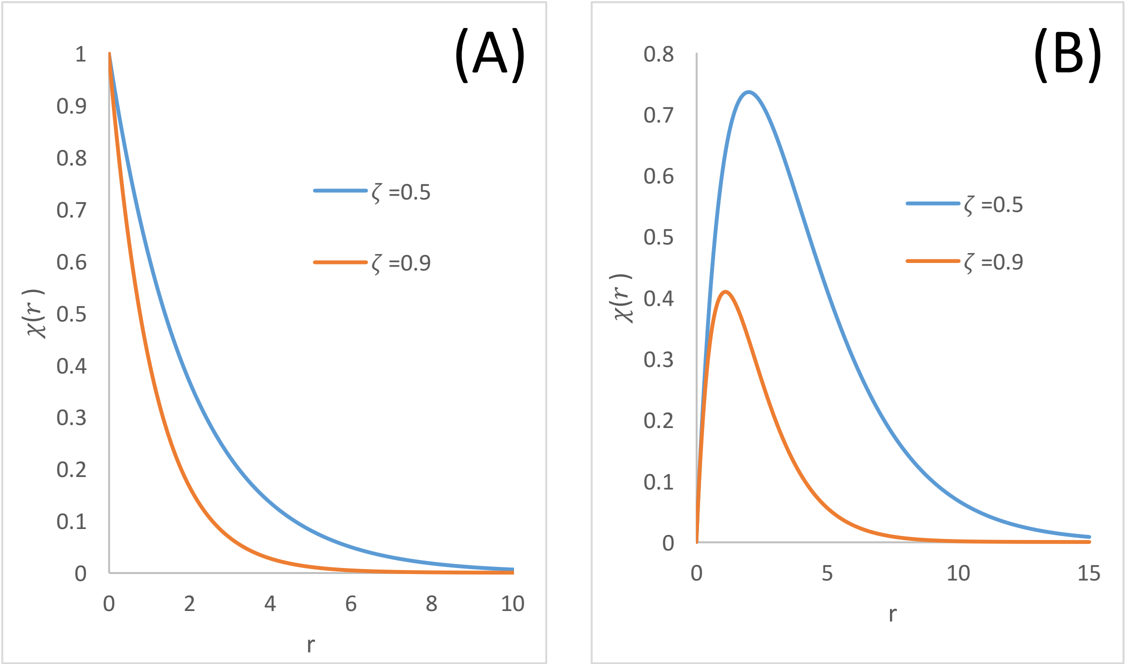

Figure 5. The radial distributions of (A) two 1s-type orbitals and (B) two 2p-type orbitals, each with different zeta exponents.

While STOs are advantageous in that they may be directly related to atomic orbitals (viz. an intuitive physical interpretation), the use of STOs requires numerical calculation of a large number of integrals, thus leading to slow speeds of computation.[14] This problem led to the development of Gaussian-type orbitals (GTOs) of the form:[18]

$$\chi(\vec{r}) = \chi_{(\zeta,n,l,m;r,\theta,\phi)}(\vec{r}) = \mathrm{N}r^{n-1}e^{-\alpha r^{2}}Y_{lm}(\theta,\phi) \qquad \text{Equation 12}$$

where N is a normalization constant, α is the orbital exponent, r, θ, ϕ are spherical coordinates, n, l, m are the principal, angular, and magnetic quantum numbers, respectively. The property of GTOs that makes them so desirable for use in quantum calculations is that the product of two Gaussian functions at two different centers can be represented by a single Gaussian function located at some point between these two centers (see Figure 6). Consider two s-type orbitals of a diatomic molecule like H_2 as an example. The two-center two-electron orbital can be represented by Gaussian type functions of the form:[18]

$$\chi(\overrightarrow{\mathrm{r_A}})\chi(\overrightarrow{\mathrm{r_B}}) = \mathrm{N}^2 \mathrm{e}^{-\alpha \mathrm{r_A}^2} \mathrm{e}^{-\alpha \mathrm{r_B}^2} \qquad \text{Equation 13}$$

where $\overrightarrow{r_A}$ and $\overrightarrow{r_B}$ are the position of the electrons relative to nuclei A and B, respectively. Replacing $\overrightarrow{r_B}$ vector by an internuclear vector $\vec{R}$ and $\overrightarrow{r_A}$ (*i.e.,* $\overrightarrow{r_B} = \vec{R} - \overrightarrow{r_A}$), Equation 13 becomes:[18]

$$\chi(\overrightarrow{r_A})\chi(\overrightarrow{r_B}) = N^2 e^{-\frac{1}{2}\alpha R^2} e^{-2\alpha\left|\overrightarrow{r_A}-\frac{1}{2}\vec{R}\right|^2} \qquad \text{Equation 14}$$

Thus, the integrals in the two-center two-electron system become integrals in a single-center two-electron system. This is much easier to evaluate, thus leading to a significant decrease the computational cost.[18] Despite their more efficient computational performance, GTOs are a poorer model of the wavefunction at the nuclei due to the nature of Gaussian-type orbitals' functions. However, this drawback is tolerable when dealing with systems (like cobalt) wherein the core electrons are unimportant in determining chemical properties.[18]

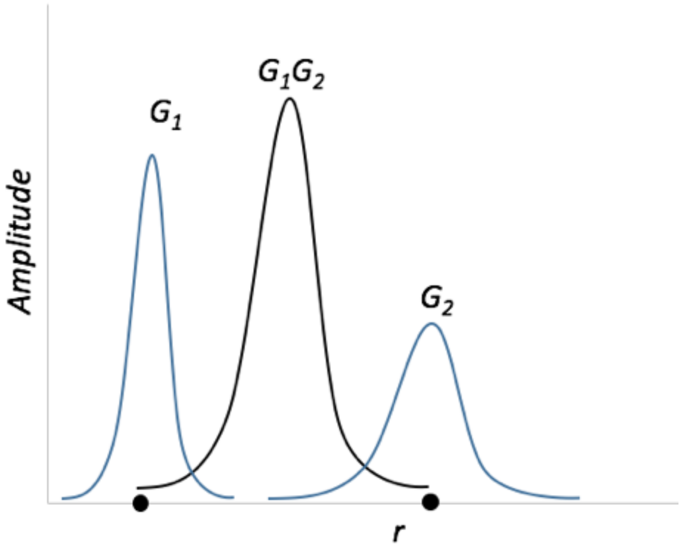

Figure 6: The product of two Gaussian (G_1, G_2) is itself a Gaussian lying between the two original functions.[19]

The "minimal basis set" is a linear combination of "primitive" single zeta Gaussian functions. To pursue the higher accuracy, multiple-zeta basis sets are used. The "multiplicity" in the zeta nomenclature (*e.g.*, triple zeta) refers to the number of basis functions applied to replace each basis function in minimal basis set. To balance the accuracy and the computational demand when a large basis set is required, split valence basis sets (SV basis set) can be used. Split valence basis sets increase the "zeta multiplicity" of the valence orbitals, but leave the core orbitals unaltered. The underlying reasoning for this approach lies in the fact that the valance orbitals affect chemical properties much more than do the core orbitals.[17] This modification requires less computational effort and as such the calculations are faster. For example, the basis functions of the oxygen atom in the double-zeta basis set decrease from 10 [$2\times5\ (1s, 2s, 2p_x, 2p_y, 2p_z)$] to 9 [1s +$2\times4\ (2s, 2p_x, 2p_y, 2p_z)$] in the split-valance basis set.[20]

The notation employed for the split-valence basis sets of John Pople is X-YZg, where X represents the number of inner shell GTOs, Y represents the number of inner valence GTOs, Z represents the number of outer valance GTOs, and g indicates that GTOs are used. For a more accurate model of the wavefunction, polarization and diffuse functions should also be included in the basis set. Polarization functions, which are functions that model higher angular momentum orbitals, can be included in the basis set to polarize the electron densities (*i.e.*, introduce geometric variation/asymmetry) by introducing hybridization/mixing.[17] For instance, p-type GTOs can be added to the hydrogen atom basis set to mix with the s-type GTOs to yield non-spherical electron density distributions. Similarly, s- and p-type GTOs can be polarized by adding d-type GTOs to the atom. Diffuse functions, which have a very small orbital exponent and, therefore, a very large radial distribution, are added to introduce diffuse, long-range character/behavior to valence orbitals.[17] It is especially necessary to add diffuse functions to the basis sets of transition metal-containing species, to correctly model their large, diffuse valence d-orbitals.[17] It is also recommended to use diffuse and polarizable functions to model anions and to more accurately capture non-covalent interactions. A good description of several common GTO basis sets is given in Appendix 6.

2.2.1.2 Basis Set Superposition Error (BSSE)

Owing to the fact that the calculations must use finite basis sets, basis set superposition error (BSSE) is an important concern. BSSE occurs when the basis wavefunctions of two atoms overlap with one another, leading to over compensation of the bond order and, therefore, the artificial strengthening of the intermolecular (interatomic) interaction compared to the infinite basis set limit. Before accounting for BSSE, the dissociation energy of a system composed of two moieties, A and B, is calculated as follows:[21]

$$\Delta E_{AB} = [E_A(\chi_A) + E_B(\chi_B)] - E_{AB}(\chi_{AB}) \qquad \text{Equation 15}$$

where the $E_A(\chi_A)$ and $E_B(\chi_B)$ are the energies of fragments A and B in their own basis set, respectively, and $E_{AB}(\chi_{AB})$ is the energy of the molecule AB. Obviously, the basis sets for these three energy calculations are not consistent. For a consistent calculation, all the fragments should be optimized under the same basis:

$$\Delta E_{AB}^{true} = [E_A(\chi_{AB}) + E_B(\chi_{AB})] - E_{AB}(\chi_{AB}) \qquad \text{Equation 16}$$

To account for this difference between ΔE_{AB} and ΔE_{AB}^{true} (*i.e.*, the BSSE), the counterpoise correction energy (δ^{CP})[21] can be defined as:

$$\delta^{CP} = \Delta E_{AB}^{true} - \Delta E_{AB} = [E_A(\chi_{AB}) - E_A(\chi_A)] + [E_B(\chi_{AB}) - E_B(\chi_B)] \qquad \text{Equation 17}$$

Physically, δ^{CP} represents the extra stabilizing energy generated by the inclusion of the basis set from fragment B in the calculation of fragment A (and vice versa). Based on this definition, the corrected binding energy is:

$$\Delta \mathrm{E}_{\mathrm{AB}}^{\mathrm{CP}} = \Delta \mathrm{E}_{\mathrm{AB}} + \delta^{\mathrm{CP}} \qquad \text{Equation 18}$$

2.2.2 Hartree-Fock and Density Functional Theory

2.2.2.1 Hartree-Fock Theory

In the Hartree-Fock (HF) method, the wavefunction of the system is modeled with a single Slater Determinant.[18] This is an antisymmetric determinant (to account for the fermionic property of electrons) composed of spin orbitals, χ_i.

$$\Psi(\mathrm{x}_1, \mathrm{x}_2, \ldots, \mathrm{x}_N) = (N!)^{-1/2} \begin{vmatrix} \chi_i(\mathrm{x}_1) & \chi_j(\mathrm{x}_1) & \cdots & \chi_k(\mathrm{x}_1) \\ \chi_i(\mathrm{x}_2) & \chi_j(\mathrm{x}_2) & \cdots & \chi_k(\mathrm{x}_2) \\ \vdots & \vdots & & \vdots \\ \chi_i(\mathrm{x}_N) & \chi_j(\mathrm{x}_N) & \cdots & \chi_k(\mathrm{x}_N) \end{vmatrix} \qquad \text{Equation 19}$$

where $(N!)^{-1/2}$ is a normalization factor, $\chi_i(\mathrm{x}_N)$ describes the occupation of the *i*th spin orbital by the Nth electron. Generally, the determinant is shortened in the Dirac notation representing the orbital occupation of individual electrons:[15]

$$\Psi(\mathrm{x}_1, \mathrm{x}_2, \ldots, \mathrm{x}_N) = |\chi_i \chi_j \ldots \chi_k\rangle \qquad \text{Equation 20}$$

The Hamiltonian, $\widehat{H}$, (see Equation 21) can operate on the Hartree-Fock wavefunction ($\widehat{H}\Psi_{HF} = E\Psi_{HF}$) to obtain the total energy.[15]

$$\widehat{H} = -\sum_{i=1}^{N} \frac{1}{2}\nabla_i^2 - \sum_{A=1}^{M} \frac{1}{2M_A}\nabla_A^2 - \sum_{i=1}^{N}\sum_{A=1}^{M} \frac{Z_A}{r_{iA}} + \sum_{i=1}^{N}\sum_{j>i}^{N} \frac{1}{r_{ij}} + \sum_{A=1}^{M}\sum_{B>A}^{M} \frac{Z_A Z_B}{R_{AB}} \qquad \text{Equation 21}$$

where *i, j* stands for the electrons (from 1to *N*), *A, B* stands for the nuclei (from 1 to *M*), and r_{ij} and R_{AB} are the distance between the electrons and the nuclei, respectively.

After application of the Born-Oppenheimer approximation, which assumes that the nuclei in a molecule are fixed on the electronic time scale, the electronic Hamiltonian becomes:[15]

$$\widehat{H}_{elec} = -\sum_{i=1}^{N} \frac{1}{2}\nabla_i^2 - \sum_{i=1}^{N}\sum_{A=1}^{M} \frac{Z_A}{r_{iA}} + \sum_{i=1}^{N}\sum_{j>i}^{N} \frac{1}{r_{ij}} \qquad \text{Equation 22}$$

$$= \quad \sum_{i=1}^{N} \hat{h}_i \quad + \quad \sum_{i=1}^{N} \sum_{j>i}^{N} \frac{1}{r_{ij}}$$

$$= \quad \hat{\mathcal{O}}_1 \quad + \quad \hat{\mathcal{O}}_2$$

where $\hat{\mathcal{O}}_1$ is operator describing the kinetic energy (KE) and the potential energy of electron *i* (describes the Coulomb attraction between the electrons and the nuclei), and $\hat{\mathcal{O}}_2$ is the operator describing the average potential experienced by the *i*th electron due to the presence of the other electrons (*i.e.,* repulsion between electrons).[15] The ground state energy of a system can be calculated by:

$$\hat{\mathrm{H}}_{\mathrm{elec}}|\Psi_0\rangle = \mathrm{E}_0|\Psi_0\rangle \rightarrow \langle\Psi_0|\hat{\mathrm{H}}_{\mathrm{elec}}|\Psi_0\rangle = \mathrm{E}_0\langle\Psi_0|\Psi_0\rangle \rightarrow \mathrm{E}_0 = \langle\Psi_0|\hat{\mathrm{H}}_{\mathrm{elec}}|\Psi_0\rangle \quad \text{Equation 23}$$

In terms of the above operators $\hat{\mathcal{O}}_1$ and $\hat{\mathcal{O}}_2$:

$$\mathrm{E}_0 = \langle\Psi_0|\hat{\mathcal{O}}_1 + \hat{\mathcal{O}}_2\ |\Psi_0\rangle = \langle\Psi_0|\hat{\mathcal{O}}_1|\Psi_0\rangle \quad + \quad \langle\Psi_0|\hat{\mathcal{O}}_2|\Psi_0\rangle \quad \text{Equation 24}$$

$$= 2\sum_{\mathrm{i}}^{\mathrm{N}}\langle\chi_i|\hat{h}|\chi_i\rangle \;+\; \sum_{j}^{M}\sum_{i\neq j}^{N} 2\langle\chi_i\chi_i|\chi_j\chi_j\rangle - \langle\chi_i\chi_j|\chi_j\chi_i\rangle$$

$$= 2\sum_{\mathrm{i}}^{\mathrm{N}}\langle\chi_i|\hat{h}|\chi_i\rangle \;+\; \sum_{j}^{M}\sum_{i\neq j}^{N} 2\hat{\mathrm{J}} - \hat{\mathrm{K}}$$

where $\langle\Psi_0|\hat{\mathcal{O}}_1|\Psi_0\rangle = 2\sum_{\mathrm{i}}^{\mathrm{N}}\langle\chi_i|\hat{h}|\chi_i\rangle$ are one-electron integrals, and $\langle\Psi_0|\hat{\mathcal{O}}_2|\Psi_0\rangle = \sum_{j}^{M}\sum_{i\neq j}^{N} 2\langle\chi_i\chi_i|\chi_j\chi_j\rangle - \langle\chi_i\chi_j|\chi_j\chi_i\rangle = \sum_{j}^{M}\sum_{i\neq j}^{N} 2\hat{\mathrm{J}} - \hat{\mathrm{K}}$ are the two-electrons integrals, $\hat{\mathrm{J}}$ is the coulomb integral, and $\hat{\mathrm{K}}$ is the exchange integral.

To solve for the energy, the iterative self-consistent-field (SCF) method is employed. The basic rule of SCF is that the variational principle can be used to find the lowest possible energy (*i.e.*, the ground state energy) by testing a variety of wavefunctions (see Equation 25).

$$\mathrm{E}_{\mathrm{trial}} \geq \mathrm{E}_0 \quad \text{where } \mathrm{E}_0 \text{ is the lowest eigenvalue of } \hat{\mathrm{H}} \qquad \text{Equation 25}$$

In the SCF iteration method, the energy of a trial wave function Ψ, known as an initial guess, is evaluated:[15]

$$\mathrm{E}[\Psi] = \langle\Psi|\,\hat{\mathrm{H}}|\Psi\rangle \qquad \text{Equation 26}$$

Assuming that we vary Ψ by an small amount $\delta\Psi$, and then the resulting energy, $E[\Psi + \ \delta\Psi]$ becomes: [15]

$$\begin{aligned}\mathrm{E}[\Psi + \ \delta\Psi] &= \langle\Psi + \ \delta\Psi|\,\hat{\mathrm{H}}|\Psi + \ \delta\Psi\rangle \qquad \text{Equation 27}\\ &= \langle\Psi|\,\hat{H}|\Psi\rangle + \langle\delta\Psi|\,\hat{H}|\Psi\rangle + \langle\Psi|\,\hat{H}|\delta\Psi\rangle + \cdots\\ &= E[\Psi] + \delta E + \cdots\end{aligned}$$

The SCF iteration proceeds to find the Ψ so that first variation, δE, is within the specified convergence threshold. Once this criterion, the iteration process finishes.[22]

2.2.2.2 Density Functional Theory (DFT)

DFT describes the system with electron density (ρ), which calculates the probability of finding N electrons and integrating over the positions of all of the electrons as per:

$$\rho(\vec{\mathrm{r}}) = \mathrm{N}\int \mathrm{d}^3\mathbf{r_2}\int \mathrm{d}^3\mathbf{r_3}\ldots\int \mathrm{d}^3\mathbf{r_N}\,|\Psi(\mathrm{r}_1, \mathrm{r}_2, \ldots, \mathrm{r}_\mathrm{N})|^2 \qquad \text{Equation 28}$$

where ρ is the density of the electron cloud of N electrons, and Ψ is the wavefunction for the N-electron system. This description depends on 3N spatial coordinates and N spin coordinates.[23] According to the Hohenberg-Kohn theorem (Equation 29), which is an analog of the variational principle, the ground-state electronic density, $\rho_0(\vec{r})$, contains precisely the same information as ground-state wavefunction Ψ_0.[23]

$$\langle\Psi_0|\hat{\mathrm{H}}|\Psi_0\rangle = \mathrm{E}_0 = \mathrm{E}(\rho_0) \qquad \text{Equation 29}$$

Thus, the electronic energy E can be calculated from ρ:

$$\mathrm{E}[\rho] = \mathrm{T}[\rho] + \mathrm{E_{Ne}}[\rho] + \mathrm{E_{ee}}[\rho] \qquad \text{Equation 30}$$

where $\mathrm{T}[\rho]$ is the electronic kinetic energy, $\mathrm{E_{Ne}}[\rho]$ is the energy of nucleus-electron attraction, and $\mathrm{E_{ee}}[\rho]$ is the energy of electron-electron repulsion. In Equation 30, the $\mathrm{T}[\rho]$ can be approximated by expressing the density in terms of the non-interacting-electron orbitals ϕ (denoted $\mathrm{T}_S[\rho]$). Thus, the energy calculated from DFT follows:

$$\mathrm{E_{DFT}}[\rho] = \mathrm{T_s}[\rho] + \mathrm{E_{Ne}}[\rho] + \mathrm{J}[\rho] + \mathrm{E_{xc}}[\rho] \qquad \text{Equation 31}$$

where $\mathrm{J}[\rho]$ is the Coulomb term and $\mathrm{E}_{xc}[\rho]$ is the exchange-correlation energy. The most challenging aspect of the DFT treatment is determining the exchange-correlation energy. There are three different categories of density functional methods which approximate the E_{xc} term: (1) the local density approximation (LDA), (2) the generalized gradient approximation (GGA), and (3) hybrid methods. For LDA functionals, the exchange-correlation energy only relies on the electron density at given points while in the GGA method, it not only depends on the local electron density but also the gradient of the density. The hybrid methods involve incorporating some exact HF exchange into the density functional, shown in Equation 32:[24]

$$\mathrm{E_{XC}^{hybrid}} = \mathrm{E_{XC}^{GGA}} + \mathrm{c_x}(\mathrm{E_X^{HF}} - \mathrm{E_X^{GGA}}) \qquad \text{Equation 32}$$

Here, E_X^{HF} is the Hartree-Fock exchange energy, E_X^{GGA} and E_{XC}^{GGA} are the GGA exchange (x) and exchange-correlation (xc) energies, respectively, and c_X is a coefficient, which controls the amount of Hartree-Fock exchange that is incorporated into the hybrid functional. If the coefficient c_X is 0 %, then it yields a pure GGA functional.[24] The HF exchange coefficient of several popular DFT methods are given below in Table 5.[11]

Table 5: The HF exchange coefficient for several common functional.[11]

Methods	B3LYP	TPSSH	PBE	PBE0	TPSS
HF exchange coefficient	20%	10%	0%	25%	0%

2.2.2.3 Time-Dependent Density Functional Theory

To explore excited state electronic structure, PECs can be constructed using time-dependent density functional theory (TD-DFT). TD-DFT is an extension of DFT which is used to investigate the properties and dynamics of systems in the presence of time-dependent potentials. Since a photon can be interpreted as a electromagnetic wave, it can be treated as a time-dependent periodic perturbation to a molecular system:[25]

$$\hat{V}(x,t) = \hat{V}(x)e^{\pm i\omega\tau} = -\hat{\mu}\cdot\varepsilon e^{\pm i\omega\tau} \qquad \text{Equation 33}$$

where $\hat{V}(x,t)$ is the potential that depends on the time and position, $\hat{V}(x)$ is the potential that only depends on the position, $\hat{\mu}$ is the dipole moment, ε is the electric field intensity, and ω is the angular frequency of electron in the oscillating electronic field. This periodic perturbation leads to a tiny change of the electron density, thereby, changing the energy of the system. Suppose that we only have the state m initially; thus the coefficient of state m is c_m=1. Then, the state k appears and increases after "switching on" the perturbation (*i.e.,* the coefficient c_k increases from 0). This increasing rate of state k is proportional to the coupling coefficient V_{km}:[25]

$$V_{km} = i\hbar\frac{\partial c_k}{\partial\tau} \qquad \text{for } k = 1, 2, \ldots \text{N.} \qquad \text{Equation 34}$$

where V_{km} is the coupling coefficient between the stationary state $\Psi_m^{(0)}$ at $\tau = 0$ and the stationary state $\Psi_k^{(0)}$ at time τ:[25]

$$V_{km} \equiv \langle \Psi_k^{(0)} | \hat{V} \Psi_m^{(0)} \rangle = v_{km} e^{i(\omega_{km} \pm \omega)\tau} \qquad \text{Equation 35}$$

Combining Equations 34 and 35, we obtained:[25]

$$\frac{\partial c_k}{\partial \tau} = -\frac{i}{\hbar} v_{km} e^{i(\omega_{km} \pm \omega)\tau} \qquad \text{Equation 36}$$

Integrating Equation 36 with the boundary condition $c_k(\tau = 0)$=0, the coefficient of state *k* can be obtained:

$$c_k(\tau) = -\frac{i}{\hbar} \int_0^\tau d\tau \, v_{km}(\tau) e^{i(\omega_{km} \pm \omega)\tau} \qquad \text{Equation 37}$$

Thus, the probability ($|c_k(\tau)|^2$) per unit time of transition among states (*e.g.,* from the *mth* state to *kth)* state is:[25]

$$w_m^k = \frac{|c_k(\tau)|^2}{\tau} = |v_{km}|^2 \frac{2\pi}{\hbar} \delta(E_k - E_m \pm \hbar\omega) \qquad \text{Equation 38}$$

where v_{km} is the coupling between *kth* and *mth* states through perturbation $\hat{V}$, and δ is the Dirac delta function. Excited states are identified when $E_k - E_m = \hbar\omega$. This Equation is known as the Fermi Golden Rule,[18] which can be used to map the excited states with respect to the ground electronic state.[25]

2.2.3 Configuration Interaction

Configuration interaction (CI) methods improve on the Hartree-Fock solution (Ψ_0; described in section 2.2.2) by adding dynamic correlation. In this treatment, contributions from excited configurations are also included in the total wavefunction description. For example, contributions from single electron excitations (Ψ_a^r), wherein the electron in spin orbital χ_a is promoted to the spin orbital χ_r, and double excitations (Ψ_{ab}^{rs}), wherein two electrons in spin orbitals χ_a and χ_b are promoted to spin orbitals χ_r and $\chi_s$are routinely incorporated in the description of the ground state wavefunction.[15]

$$\Psi_0 = |\chi_1\chi_2 \cdots \chi_a\chi_b \cdots \chi_N\rangle \xrightarrow{\text{electron in } \chi_a \, promoted \ to \ \chi_r} \Psi_a^r = |\chi_1\chi_2 \cdots \chi_r\chi_b \cdots \chi_N\rangle$$

Equation 39

$$\Psi_0 = |\chi_1 \cdots \chi_a\chi_b \cdots \chi_N\rangle \xrightarrow{electrons \ in \ \chi_a\chi_b \ promotedd \ to \ \chi_r\chi_s} \Psi_{ab}^{rs} = |\chi_1 \cdots \chi_r\chi_s \cdots \chi_N\rangle$$

Equation 40

Thus, the CI wavefunction (Ψ_{CI}) is expressed as a linear combination of all Slater determinants:[26]

$$\Psi_{\mathrm{CI}} = \mathrm{C}_0|\Psi_0\rangle + \sum\nolimits_{\mathrm{a,r}} \mathrm{C}_{\mathrm{a}}^{\mathrm{r}}|\Psi_{\mathrm{a}}^{\mathrm{r}}\rangle + \sum\nolimits_{\mathrm{a,b,r,s}} \mathrm{C}_{\mathrm{a,b}}^{\mathrm{r,s}}|\Psi_{\mathrm{ab}}^{\mathrm{rs}}\rangle + \cdots$$ Equation 41

where $C_x$is the weighting coefficient of the wavefunction, *a* and *b* are inactive orbitals (*i.e.,* double-occupied), and *r* and *s* are active orbitals. $\sum_{a,r} C_a^r|\Psi_a^r\rangle$ represents one electron promotions from the inactive orbitals to the active orbitals (*i.e.,* single excitation), and $\sum_{a,b,r,s} C_{a,b}^{r,s}|\Psi_{ab}^{rs}\rangle$ represents two electron promotions from the inactive orbitals to the active orbitals (*i.e.,* double excitations).

In Full-CI calculations, the number of determinants for a N-electron system of 2K spin orbitals is $\binom{2K}{N} = \frac{(2K)!}{N!(2K-N)!}$. This large number of determinants leads to slow convergence of the CI calculation. Thus, the number of Ψ_i must be truncated to make calculations computationally feasible. Because the largest corrections to total energy comes from treatment of the single and double excitations, CIS (configuration interaction with single excitation), CID (configuration interaction with double excitations), and CISD (configuration interaction with single and double excitations) are used widely. However, the CI energies obtained with these methods are no longer size extensive or size consistent if the truncated CI is used.[27]

For a system containing a number of isolated particles, size-consistency (or size extensivity) refers to the equality of system's total energy to the sum of the energies of the individual particles. In other words, for a size-consistent treatment, $E_{tot} = E_0 + E_1 + \cdots + E_n\ (n = N)$. For example, if a two particle system (*AB*) is calculated by using the CID method, the total energy of the *AB* molecule should equal to the energy of *A* plus the energy of *B* ($E_{tot}= E_A+E_B$) when *A* and *B* are infinitely separated (*i.e.*, no shared electron density):[27] The wavefunctions of A and B separately are:

$$^{A}\Psi_{CID} = {}^{A}\Psi_{HF} + {}^{A}\Psi_{D} \qquad \text{Equation 42}$$

$$^{B}\Psi_{CID} = {}^{B}\Psi_{HF} + {}^{B}\Psi_{D}$$

However, when including both A and B in the same calculation, the wavefunction becomes

$$\begin{aligned} ^{\mathrm{A+B}}\Psi_{\mathrm{CID}} &= {}^{\mathrm{A}}\Psi_{\mathrm{CID}}\,{}^{\mathrm{B}}\Psi_{\mathrm{CID}} \qquad \text{Equation 43} \\ &= ({}^{A}\Psi_{HF} + {}^{A}\Psi_{D})({}^{B}\Psi_{HF} + {}^{B}\Psi_{D}) \\ &= {}^{A+B}\Psi_{HF} + {}^{A+B}\Psi_{D} + \boldsymbol{{}^{A}\Psi_{D}\,{}^{B}\Psi_{D}} \end{aligned}$$

In comparing Equations 42 and 43, $^{A}\Psi_{CID}\,{}^{B}\Psi_{CID} \neq {}^{A+B}\Psi_{CID}$. The missing energy associated with $\boldsymbol{{}^{A}\Psi_{D}\,{}^{B}\Psi_{D}}$ (quadruple excitation) gives rise to size inconsistency.

The Davidson correction (DC) can be used to estimate the energy terms to improve size-consistency. This correction (see Equation 44) approximates the effect of "quadrupole excitation" and allows one to estimate the value of the full configuration interaction energy from a limited configuration interaction expansion. [27] The CI calculation with Davidson correction is called the CI+Q method.

$$\Delta E_{DC} = (1 - C_0{}^2)E_{corr}(CID) \qquad \text{Equation 44}$$

where C_0 is the coefficient of the Hartree-Fock wavefunction in the normalized CID wavefunction.

2.2.4 Coupled Cluster (CC) Theory

Different from the CI approach, the CC theory, which uses the Hartree-Fock wavefunction, Ψ_0, as the zeroth order reference for correlation energy calculations, is size-consistent (see Equation 45).[28, 29]

$$\Psi_{CC} = e^{\hat{T}}\Psi_0 \qquad \text{Equation 45}$$

where Ψ_0 is the HF wavefunction and $\hat{T}$ is the cluster operator.

$$^{A+B}\Psi_{CCSD} = e^{\hat{T}}\Psi_0 = e^{\hat{T}_A+\hat{T}_B}\Psi_0 = e^{\hat{T}_A}e^{\hat{T}_B}\Psi_0 = {}^{A}\Psi_{CCSD} + {}^{B}\Psi_{CCSD} \qquad \text{Equation 46}$$

After application of a Taylor series expansion ($e^{\hat{T}} \cong 1 + \hat{T} + \frac{\hat{T}^2}{2} + \frac{\hat{T}^3}{3!} + \cdots$), the CC wavefunction becomes:[28]

$$\Psi_{CC} = (1 + \hat{T} + \frac{\hat{T}^2}{2} + \frac{\hat{T}^3}{3!} + \cdots)\Psi_0 \qquad \text{Equation 47}$$

where the cluster operator, $\hat{T}$, consists a series of operators, which can be expanded in terms of single excitation ($\hat{T}_1$), double excitation($\hat{T}_2$), triple excitations($\hat{T}_3$), *etc*.[28]

$$\hat{T} = \hat{T}_1 + \hat{T}_2 + \hat{T}_3 + \cdots + \hat{T}_n \qquad \text{Equation 48}$$

Where $\hat{T}_1\Psi_0 = \sum_{i,a} t_i^a |\Psi_i^a\rangle$,

$$\hat{T}_2\Psi_0 = \sum_{i,j,a,b} t_{i,j}^{a,b} |\Psi_{i,j}^{a,b}\rangle,$$

$$\hat{T}_3\Psi_0 = \sum_{i,j,k,a,b,c} t_{i,j,k}^{a,b,c} |\Psi_{i,j,k}^{a,b,c}\rangle$$

The CC wavefunction can then be employed in the Schrödinger equation to obtain the total energy as per:[28]

$$\hat{H}\Psi_{CC} = E\Psi_{CC} \qquad \text{Equation 49}$$

$$\hat{H}e^{\hat{T}}\Psi_0 = Ee^{\hat{T}}\Psi_0 \qquad \text{Equation 50}$$

$$e^{-\hat{T}}\hat{H}e^{\hat{T}}\Psi_0 = Ee^{-\hat{T}}e^{\hat{T}}\Psi_0 \qquad \text{Equation 51}$$

$$e^{-\hat{T}}\hat{H}e^{\hat{T}}\Psi_0 = E\Psi_0 \qquad \text{Equation 52}$$

$$E = \langle\Psi_0|e^{-\hat{T}}\hat{H}e^{\hat{T}}|\Psi_0\rangle = \langle\Psi_0|\bar{H}|\Psi_0\rangle \qquad \text{Equation 53}$$

where $\bar{H} = e^{-\hat{T}}\hat{H}e^{\hat{T}} = \hat{H} + [\hat{H},\hat{T}] + \frac{1}{2}\left[[\hat{H},\hat{T}]\hat{T}\right] + \frac{1}{3!}\left[\left[[\hat{H},\hat{T}]\hat{T}\right]\hat{T}\right] + \frac{1}{4!}\left[\left[\left[[\hat{H},\hat{T}]\hat{T}\right]\hat{T}\right]\hat{T}\right]$.

After calculating the electronic ground state, the equation of motion (EOM) method can be used to map the excited electronic structure.[30] However, the EOM-CC method is only a useful tool for excited states when CC theory is an effective model for the ground electronic state. The implementation of EOM-CC is as follows:[30]

$$\hat{H}\Psi_k = E_k\Psi_k \qquad \text{Equation 54}$$

$$\Psi_k = \hat{R}_k\Psi_{CC} = \hat{R}_k e^{\hat{T}}\Psi_0 \qquad \text{Equation 55}$$

$$\hat{H}\hat{R}_k e^{\hat{T}}\Psi_0 = E_k\hat{R}_k e^{\hat{T}}\Psi_0$$

where $\widehat{\mathrm{R}}_{\mathrm{k}} = \mathrm{r}_0(\mathrm{k}) + \sum_{\mathrm{i,a}} \mathrm{r}_{\mathrm{i}}^{\mathrm{a}} |\Psi_{\mathrm{i}}^{\mathrm{a}}\rangle + \frac{1}{4}\sum_{\mathrm{i,j,a,b}} \mathrm{r}_{\mathrm{i,j}}^{\mathrm{a,b}} |\Psi_{\mathrm{i,j}}^{\mathrm{a,b}}\rangle + \cdots$

Equation 56

$$e^{-\widehat{T}}\widehat{H}\widehat{R}_k e^{\widehat{T}}\Psi_0 = E_k e^{-\widehat{T}} e^{\widehat{T}} \widehat{R}_k \Psi_0 \quad \text{Equation 57}$$

$$e^{-\widehat{T}}\widehat{H}\widehat{R}_k e^{\widehat{T}}\Psi_0 = E_k \widehat{R}_k \Psi_0 \quad \text{Equation 58}$$

$$\widetilde{H}\widehat{R}_k\Psi_0 = (E_k - E_0)\widehat{R}_k\Psi_0 \qquad \text{where} \quad \widetilde{H} = e^{-\widehat{T}}(\widehat{H} - E_0)e^{\widehat{T}} \quad \text{Equation 59}$$

where Ψ_k is the wavefunction for the excited states, Ψ_{CC} is the coupled-cluster ground state energy, Ψ_0 is the HF wavefunction, E_k is the corresponding excitation energy, E_0 is the ground-state energy, $\hat{R}_k$ is the excitation operator, and $\hat{T}$ is the cluster operator. The $\hat{R}_k$ operator is described in terms of a series of *r* coefficients for the excited states (i.e., $r_0(k)$, r_{i}^{a}, and $r_{i,j}^{a,b}$,…) that describe the contributions of the ground state, single excitations, double excitations, *etc*.

As the formalization of the wavefunction in Equation 59 shows, the CC method is only applicable when a single determinant HF wavefunction is a good starting point. This is often the case for closed-shell systems at equilibrium. More than one Slater determinant is needed for a qualitative description of the wavefunction in bond breaking situations, or when treating low-lying excited states, or high-spin systems. Thus, for accurate calculation of transition metal-containing systems (*e.g.*, $Co^{+} \cdot RG$), multi-reference treatment is necessary.

2.3 Computational Details

In this section, the electronic states of the ${Co_2}^{+}$ dimer obtained from DFT and CCSD calculations are illustrated, respectively. All of these calculations were performed using the

Gaussian 09 software package. The electronic states of $Co_2{}^+$ were explored using the TD-DFT method. Prior to this exploration, the optimal functional and basis set combination was determined. Here, this was achieved by conducting a series of calculations to determine the ground state spin-multiplicities of Co, Co^+ and $Co_2{}^+$ species with the TPSSH, B3LYP, PBE, PBE1, and TPSS functionals. Each of these calculations was repeated using two popular basis sets: Lanl2dz and 6-311++G(3df). Further to this, the dissociation energy of $Co_2{}^+$ was calculated (as per Equation 60). Calculated molecular parameters were then compared with the literature values.[6] This comparison is discussed below in section 2.4.1.

$$Co_2{}^+ \overset{hv}{\rightarrow} Co^+ + Co$$

$$\mathrm{D_0} = \mathrm{E_{el}(Co^+)} + \mathrm{E_{el}(Co)} - \left\{\mathrm{E_{el}}\left(\mathrm{Co_2{}^+} + \mathrm{E_{ZPE}}\right)\right\} \qquad \text{Equation 60}$$

Following selection of a suitable functional and basis set, the PECs of $Co_2{}^+$ were scanned using the TD-DFT method. In this scan, 20 low-lying electronic states of $Co_2{}^+$ were examined in the range 1.7 - 2.2 Å at a 0.02 Å increments. To improve the accuracy of the calculations, counterpoise correction was introduced. In addition, two modifications were included to improve the convergence of the SCF: utilization a larger integration grid size consisting of 99 radial shells and 590 angular points for each atom so as to improve numerical integration, and the application of quadratic convergence. In parallel with DFT calculations, the PECs of $Co_2{}^+$ were also characterized using the EOM-CCSD/lanl2dz method. The scan procedure for the EOM-CCSD calculations was exactly the same as that used in the TD-DFT calculations.

2.4 Results and Discussion

This section discusses the low-lying electronic states of ${Co_2}^+$ as calculated by DFT/TD-DFT and CCSD/EOM-CCSD. TD-DFT and CCSD calculations are discussed in sections 2.4.1 and 2.4.2, respectively.

2.4.1 Investigation of ${Co_2}^+$ with Single Reference Methods

Table 6 shows a comparison between the theoretical and experimental relative energies of Co, Co^+ and ${Co_2}^+$ at the lowest state of a given multiplicity. Five functionals (TPSS, TPSSh, PBE, PBE0, and B3LYP) are employed in conjunction with the Lanl2dz basis set to determine the lowest-energy electronic state of a given multiplicity. The results of these calculations are then compared with literature values from the NIST database to assess functional performance.[9] For the Co atom, the $a^2F_{7/2}$, $a^4F_{9/2}$, and $z^6F_{11/2}$ states are the lowest-energy doublet, quartet, and sextet states, respectively. The a^1D_2, a^3F_4, and a^5F_5 states are the lowest-energy singlet, triplet, and quintet states of Co^+. By using these calculations to assess functional performance, we gain confidence in the results for DFT calculations of the ${Co_2}^+$ system, for which there is little experimental data available.[31] An electron spin resonance (ESR) study of Co_2^+ has reported a sextet multiplicity for the ground state .[6] This was correctly identified by all five of the functionals that were tested (see Table 6). All five functionals also correctly identify the quartet multiplicity as the ground state of the neutral Co atom, and the triplet ground state of Co^+ However, when comparing the calculated energy separation between different spin-multiplicities to that which was determined experimentally, we find that none of the functionals perform well. For example, the experimental energy level spacing between the quartet and doublet states of Co is 0.92 eV, whereas all five functionals predict the energy difference to be ~0.3 eV. The absolute error in the calculations of relative spin manifold energies of Co^+ are even larger than those of the *Co* calculations.

Table 6. The experimental relative energies of Co, Co^+ and ${Co_2}^+$ at the lowest state of a given multiplicity, and those energies that calculated using five DFT functionals under Lanl2dz basis set.

	Co			Co^+			${Co_2}^+$			
	Multiplicity (2S+1)			Multiplicity (2S+1)			Multiplicity (2S+1)			
	2	4	6	1	3	5	2	4	6	8
Theory										
TPSSH	0.38	0.00	3.72	2.95	0.00	1.62	0.78	0.37	0.00	2.51
B3LYP	0.26	0.00	3.98	2.67	0.00	1.63	2.78	2.68	0.00	3.32
PBE1	0.33	0.00	3.55	3.00	0.00	1.46	2.90	0.88	0.00	3.39
PBE	0.36	0.00	4.15	2.92	0.00	1.79	13.83	0.44	0.00	2.47
TPSS	0.37	0.00	3.91	3.08	0.00	1.74	0.74	1.84	0.00	2.51
Experiment[9]	0.92	0.00	2.93	1.44	0.00	0.42	-	-	-	-

Table 7. The calculated dissociation energy (in eV) of ${Co_2}^+$ both including and excluding the counterpoise correction obtained by using five functionals with the Lanl2dz and 6-311++G(3df) basis sets.

	TPSSH	B3LYP	PBE1	PBE	TPSS
Lanl2dz					
D_e (eV)	0.546	0.288	-0.158	2.508	1.955
BSSE (eV)	-2.076	-1.738	-2.603	-1.968	-2.197
D_e (eV), corrected	2.617	1.353	0.998	4.511	4.135
6-311++G(3df)					
D_e (eV)	1.263	0.652	0.194	2.952	2.352
BSSE (eV)	-2.043	-[b]	-1.618	-1.768	-2.128
D_e (eV), corrected	3.306	-	1.812	4.720	4.480
Experimental Dissociation Energy: 2.765 eV[a]					

a: The experimental dissociation energy obtained from the photodissociation spectrum of ${Co_2}^+$. [6]

b: The B3LYP/6-311++G(3df) calculation failed to converge.

Table 7 gives the dissociation energies of Co_2^+ as calculated with the five chosen functionals using the lanl2dz and 6-311++G(3df) basis sets. Two things stand out in these results: first, there is dramatic variation in the calculated D_e values between functionals and between basis sets for a given functional; second, the BSSE correction in all cases is very large. These results already suggest that DFT may not be a good choice of calculation method for cobalt-containing systems. Nevertheless, these calculations indicate that the PBE functional is the best choice (based on agreement with experimental results) when using either the lanl2dz or the 6-311++G(3df) basis set. This is not surprising since hybrid methods are known to underestimate bond strengths.[32] However, it should be noted that the TPSSh functional best reproduces the experimental dissociation energy when accounting for BSSE. This might indicate that the BSSE correction is absolutely necessary in calculations of cobalt-containing system, but the magnitude of the BSSE correction suggests that there is something wrong with the calculation. This is further supported by the fact that the theoretical dissociation energies become *larger* after the employment of the counterpoise corrections, contrary to expectation (the BSSE energy should be positive by definition).

In an attempt to construct the low-energy PECs of Co_2^+, the TPSSh (method of choice) and B3LYP (most commonly employed) functionals were used. For comparison purposes, both theLanl2dz and 6-311++G(3df) basis sets were applied. The PECs of Co_2^+ calculated by both functionals using the 6-311++G(3df) basis set are shown in Figure 7. Note that the calculations which employ the Lanl2dz basis set produces similar results.

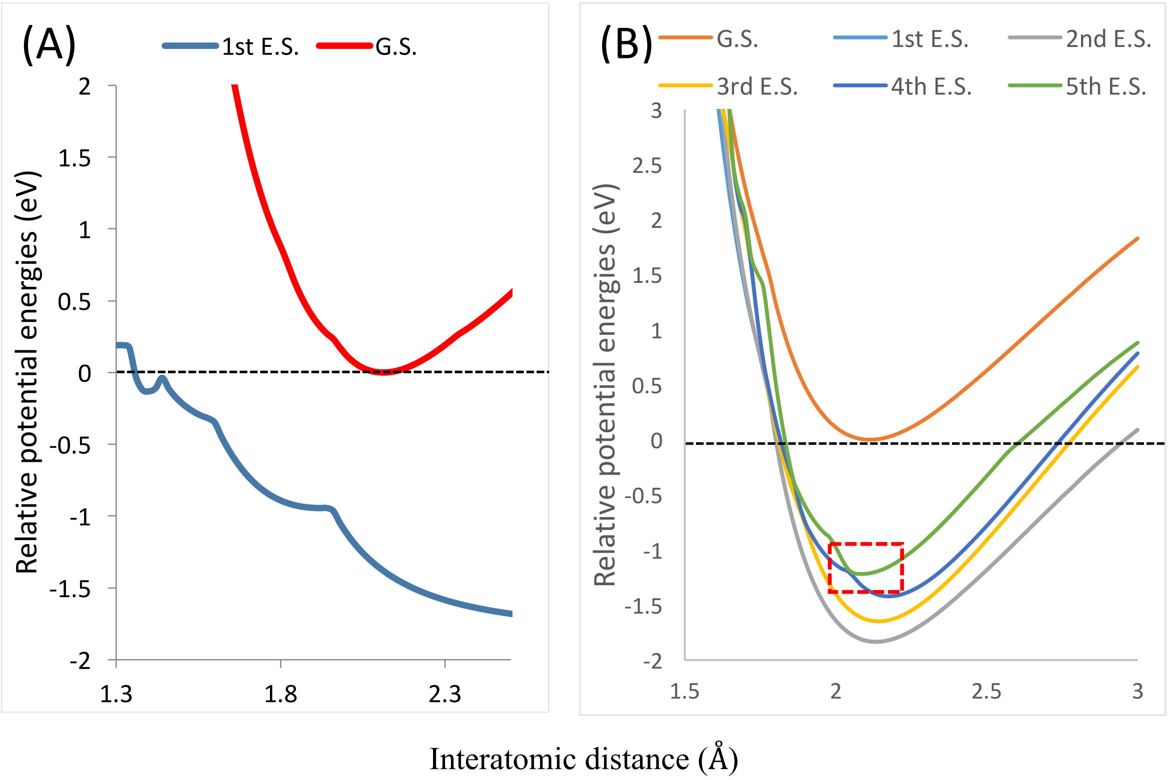

Figure 7. Low-energy PECs of $Co_2{}^+$ calculated with TD-DFT using (A) TPSSH/6-311++G(3df) and (B) B3LYP/6-311++G(3df).

As can be seen in Figure 7, both the TPSSh and B3LYP functionals generate believable ground states, but they fail in their treatment of the excited states. One failure, which is obvious in Figure 7A, is that the PECs of the calculated excited states were irregular and discontinuous. In the case of the B3LYP/6-311++G(3df) calculations, discontinuities may be a result of poor tracking of the electronic states at curve crossings (see highlight in Figure 7B). A second serious failure of the TD-DFT treatment is that the first excited state(s) are calculated to have negative potential energies with respect to the ground state. This, of course, is impossible in real physical systems. These unstable states arise due to broken symmetry in the TD-DFT treatment as described in the work of Cordova *et. al.*[24] In a nutshell, when a single-determinantal description of the ground state is incorrect, TD-DFT generates negative eigenvalues in its solution, which can be interpreted as arising from mixing with (or excitation to) other low-lying electronic states (usually of different multiplicities for molecules at equilibrium). As a result, the symmetry-broken solution yields a negative value of ω^2 (*i.e.*, an imaginary value of ω).[24] In other words, these negative excitation energies are certainly indicating that a single reference density functional description is not suitable for calculating the electronic structure and properties of ${Co_2}^+$.

To test whether the failings of the TD-DFT treatment were specific to the TD-DFT formalism, or were instead a more general failure of single reference treatment, the PECs of ${Co_2}^+$ were re-calculated at EOM-CCSD/Lanl2dz level of theory. The results of these calculations is shown in Figure 8. While the PECs are smooth and continuous, negative excited state potential energies relative to the ground electronic state again arise. Taken as a whole, it is clear that single reference methods fail in attempts to calculate the electronic structure of ${Co_2}^+$.

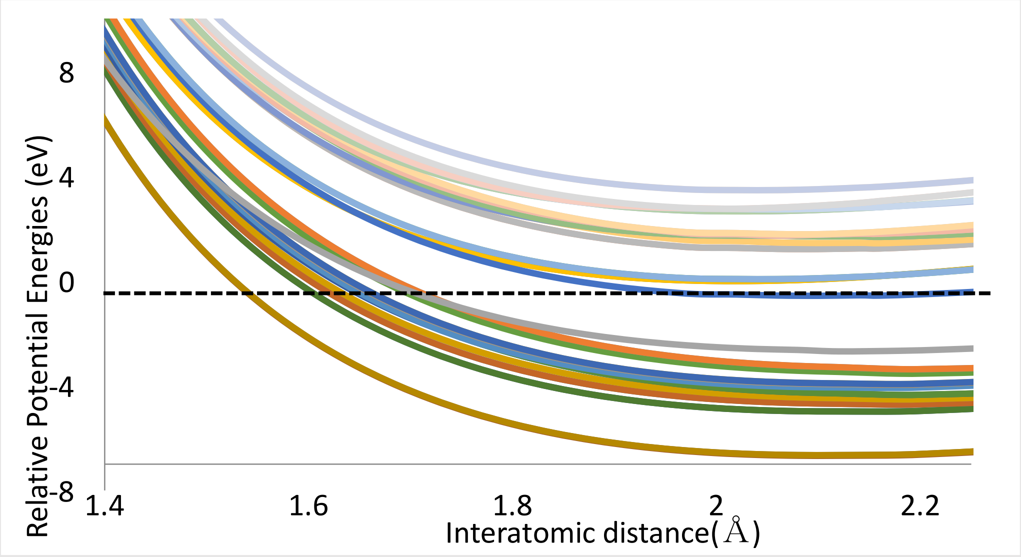

Figure 8. The PECs of ${Co_2}^+$ obtained using EOM-CCSD/Lanl2dz.

2.5 Conclusion

While DFT is able to correctly calculate the ground state spin multiplicity of Co, Co^+ and Co_2^+, relative energies between spin manifolds are poorly predicted. Moreover, the high degree in variability for dissociation energy as calculated with a variety of functionals, and the anomalous behavior of counterpoise correction calculations indicates that DFT fails to accurately treat cobalt-containing complexes. In expanding our study to include excited state calculations via the TD-DFT and EOM-CCSD methods, it became clear that the failings of our calculations stemmed from our choice of single reference calculation methods. The strongest indicator of the failure of single reference methods is the prediction of negative excitation energies relative to ground state in TD-DFT and EOM-CCSD calculations. To accurately describe the electronic structure of cobalt-containing molecules, the use of multi-reference methods is necessary.

Chapter 3: Multireference Calculations of Cobalt-Complexes

3.1 Introduction

As discussed in Chapter 2, single reference (SR) methods (*e.g.,* HF, DFT, CI, CCSD) are straightforward methods of solving many electron problems when molecular wavefunctions are well described by only one Slater determinant.[33] The HF method, whose results are widely used as starting points of single determinant calculations, can recover more than 99.9% of the total electronic energy. However, the remaining 0.1 % error, which is referred to as "electron correlation energy",[34] still leads to huge inaccuracy in the description of most chemical properties or phenomena.[35] Although accurate correlation energies and correlated wavefunctions can be estimated by SR calculations when incorporating specific corrections, a single slater determinant cannot properly describe the wavefunction of transition metal systems which contain a relatively large number of unpaired electrons and (oftentimes) a high-density of near-degenerate electronic states.[35] Thus multireference (MR) methods, which utilize multiple slater determinants to represent the system, should be introduced to recover the remaining dynamic correlation.[33]

Single reference and multi-reference wavefunction descriptions are shown in Equation 61 and Equation 62, respectively:

$$\text{Single Reference } |\Psi\rangle = |\Psi_0\rangle + \sum_\lambda C_\lambda |\Psi_\lambda\rangle \qquad \text{Equation 61}$$

$$\text{Multi-Reference } |\Psi\rangle = \sum_a C_a |\Psi_a\rangle + \sum_{\lambda \neq a} C_\lambda |\Psi_\lambda\rangle \qquad \text{Equation 62}$$

where Ψ_0, Ψ_a are the wavefunctions of the reference states, C_a are the mixing coefficients, and $\sum_{\lambda \neq a} C_\lambda |\Psi_\lambda\rangle$ is the dynamic correlation.

In the case of a single reference calculation, the ground state of the system is represented by only one slater determinant, $|\Psi_0\rangle$, while in the multireference scenario, the ground state wavefunction is represented by a mixture of low-lying electronic states denoted by the linear combination of slater determinants $\sum_a C_a\,|\Psi_a\rangle$. This replacement enables the multireference method to calculate a large number of excitation energies for systems that demand a multi-configurational approach.

Multireference configurational interaction (MRCI) and multireference equation-of-motion coupled cluster (MR-EOM-CC) are the two post Hartree-Fock multireference methods which have been used to explore the electronic states of interested transition metal with rare gas clusters: Co^+•He, Co^+•Ar, Co^+•Kr, Ag^+•Ar, and Au^+•Ar. Because the complexity of the Co_2^+, it is not calculated in this project. Below, the theory of the MRCI and MR-EOM-CC approaches are summarized and the results of the Co^+•RG (RG = He, Ar, Kr) and CM^+•Ar (CM = Ag, Au) are discussed. The MRCI and MR-EOM-CC computational details and results are discussed in sections 3.3 and 3.4, respectively. Conclusion follow in section 3.5.

3.2 Theory

3.2.1 Multireference Configuration Interaction

Consider the N_2 system during the dissociation process; there is one dominant electronic configuration at the equilibrium bond length of the ground state (see Figure 9). At internuclear distances other than at equilibrium, there is not one dominant electronic configuration to describe the system, but instead a combination of several electronic configurations is required.

Thus, the single slater determinant is not sufficient to describe the wavefunction of the N_2 system.

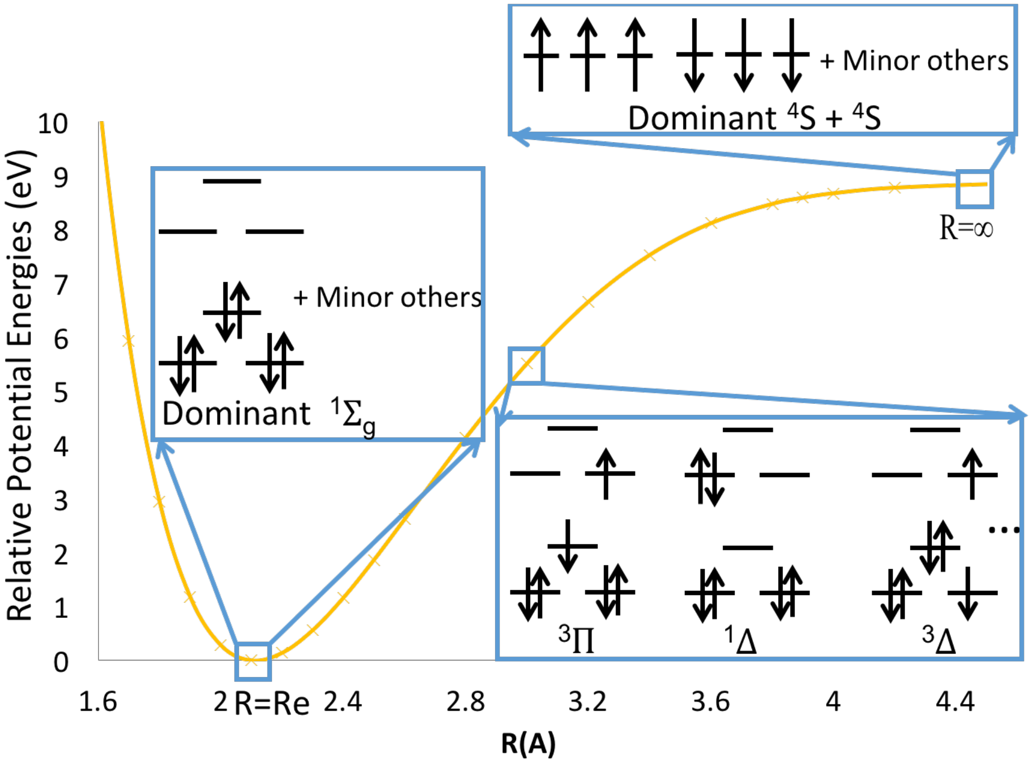

Figure 9: The electronic configurations of N_2 at different bond length.

The starting point of a MRCI calculation is a complete-active-space self-consistent-field (CASSCF) calculation, the first step of which is to construct the complete active space (CAS). The CAS is a collection of all the possible electronic configurations that contribute significantly to the current state of the system. The current state can then be expressed by a linear combination of the wavefunctions, $\sum_a C_a |\Psi_a\rangle$ which from the given electronic states:

$$|\Psi_{\mathrm{CAS}}\rangle = \sum_{\mathrm{a}} \mathrm{C_a} |\Psi_{\mathrm{a}}\rangle \qquad \text{Equation 63}$$

The CAS can be generated by choosing the number of active orbitals. These orbitals are then divided into three types: closed shell doubly *occupied*, variable occupation or *active* and empty *virtual* orbitals (see Figure 10).[36] By considering all of the electron-filling possibilities, a large number of electronic configurations can be formed. These configurations serve as the basis for the CASSCF calculation. The CASSCF calculation optimizes the orbitals to give the minimum energy of the molecule. One important assumption here is that the collection of electronic states generated from the electron-orbital filling process closely approximates the ground state of the system, such that dynamical correlation presents a minimal correlation. Thus, a careful choice of the CAS is required.

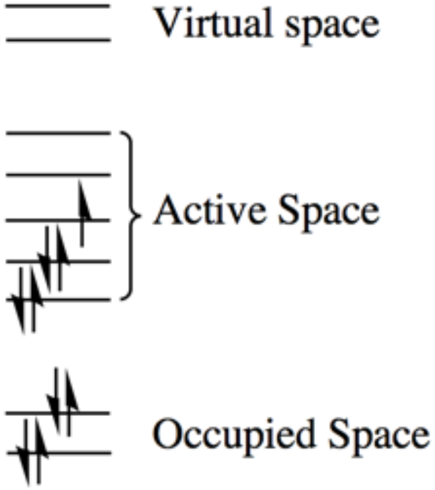

Figure 10: Schematic picture of complete active space (CAS) of a system

Different types of excitations (to generate different electronic configurations) can be classified according to the following notations: “p” stands for “particle”, which is the number of electrons entering the virtual space, and “h” indicates “hole”, which is the number of electrons leaving the doubly occupied space. Several examples are given below in Figure 11 to clarify these definitions.

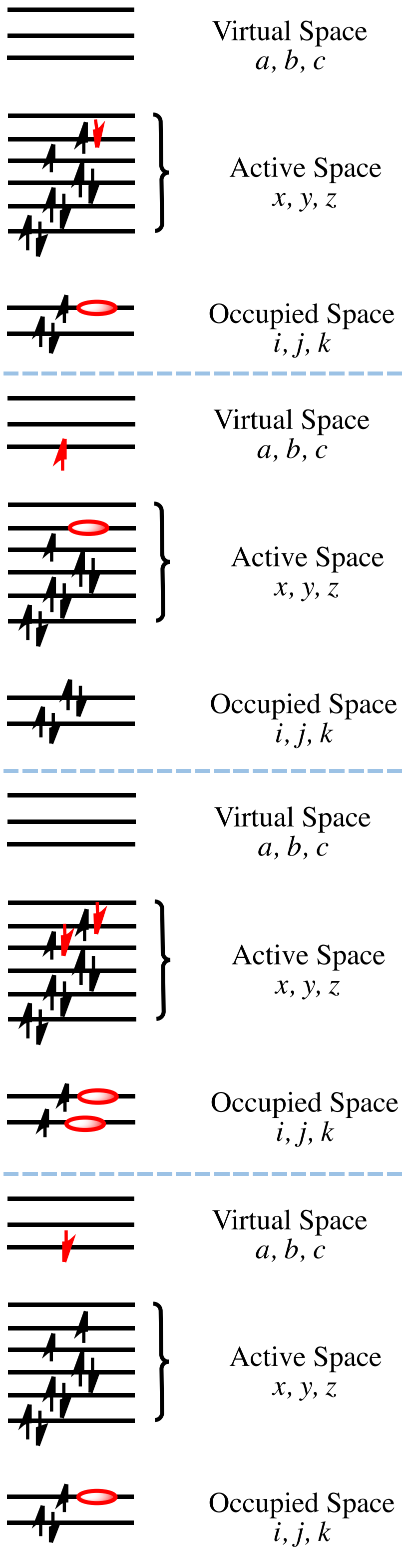

A 1-hole excitation (1h): an electron is removed from the occupied states and deposited in the active space; additional active-active excitations can occur.

A 1-particle excitation (1p): an electron is excited to the virtual space from the active space; additional active-active excitations can occur.

A 2-hole excitation (2h): Two holes are created in the occupied space and two electrons are deposited in the active space; additional active-active excitations can occur.

A 1-particle, 1-hole excitation (1p1h): There are two options; either (a) an inactive electron is promoted to the virtual space, additional active-active excitations can occur, or (b) an inactive electron is promoted to the active space, and an active electron is promoted to the virtual space.

Figure 11. A schematic picture of generating electronic configurations via electron excitations.

Figure 12 diagrammatically shows all possible single and double excitations out of the CAS. According to Equation 64, the resulting MRCI wavefunction becomes:

$$\Psi_{MRCI} = \sum_a C_a \, |\Phi_a\rangle + \sum_\lambda c_\lambda \, |\chi_\lambda\rangle = |\Phi_{CAS}\rangle + \sum_\lambda c_\lambda \, |\chi_\lambda\rangle \qquad \text{Equation 64}$$

Application of a Hamiltonian operator to the MRCI space used to minimize the expectation value of energy yields optimized coefficients. However, the MRCI calculation is very expensive due to the large number excitations (and, therefore, calculations) which must be considered.[37] In some situations, the number of active orbitals is too large to be addressed by a CAS, so it is necessary to use a restricted-active-space (RAS). There are three sub-spaces in a RAS: RAS1, RAS2, and RAS3 (see Figure 13).[38]

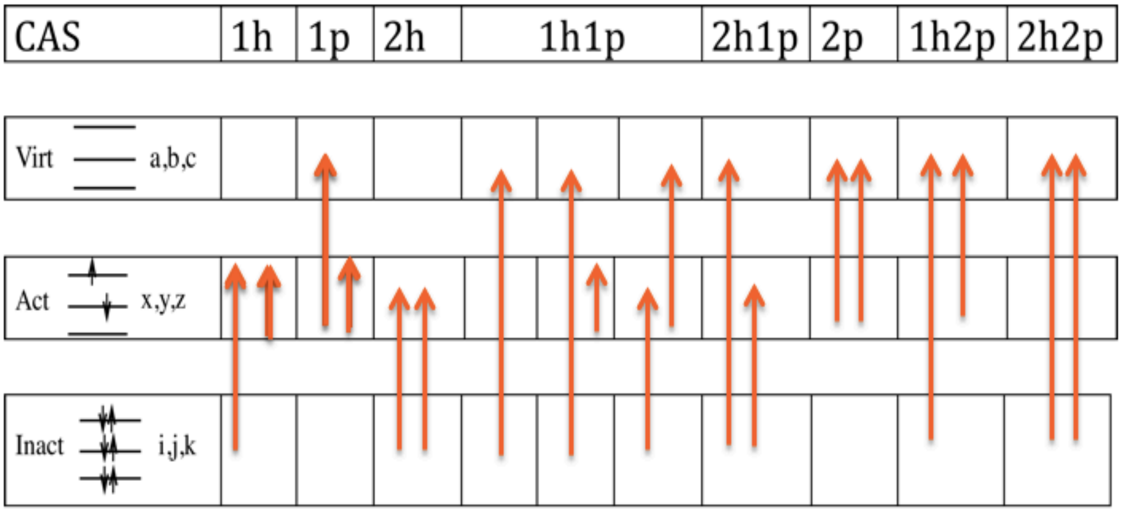

Figure 12: All single and double excitations out of the CAS.

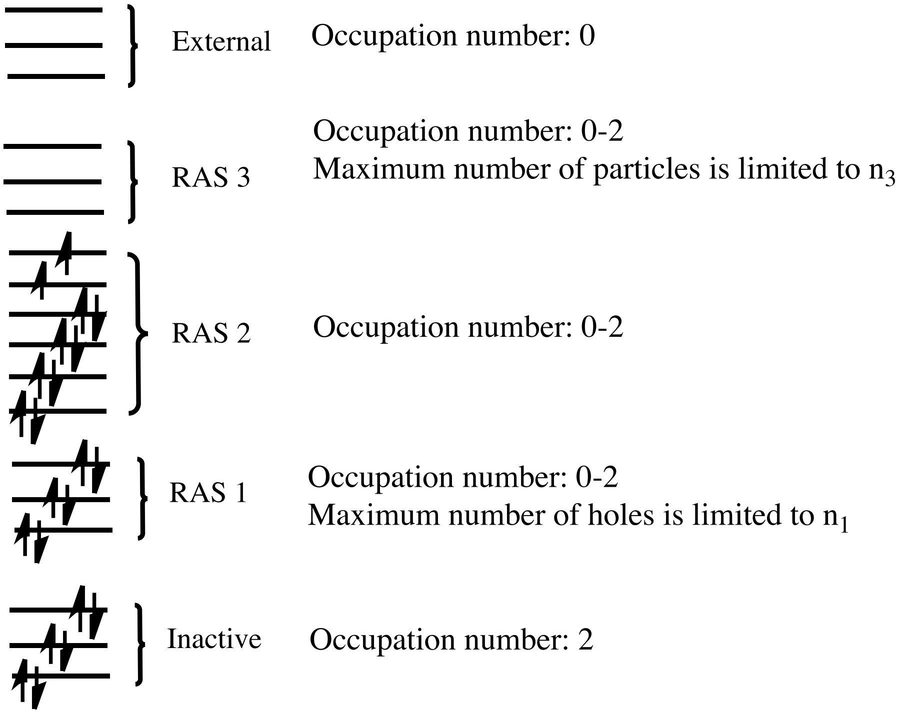

Figure 13: A schematic representation of the orbital classification in the RAS.

The key difference between the CAS and a RAS is that a RAS dictates the maximum number of particles in RAS3 and maximum number of holes in RAS1. This limitation greatly decreases the number of configuration state functions, which in turn decreases the computational cost.

3.2.2 MR-EOM-CC

The multireference formulation of coupled-cluster theory is an important extension of the standard single reference approach. The process to build the CAS wavefunction in MR-EOM-CC is the same as it is in MRCI. After the construction of the MR-EOM-CC wavefunction, two major strategies are used to calculate the energies of an electronic state: (1) transformations and (2) diagonalization.[37] By following the transformation- and diagonalization-strategy, the calculation becomes relatively compact, while in principle retaining the same eigenvalues.

3.2.2.1 Transformation Strategy

A set of similarity transformations of the second quantized Hamiltonian is performed using the following procedure:[37]

Schrodinger Equation: $\hat{H}|\Psi_\lambda\rangle = E_\lambda|\Psi_\lambda\rangle$

Hamiltonian $\bar{H}$ is transformed based on the operator $\hat{X}$: $\bar{H} = e^{-\hat{X}}\hat{H}e^{\hat{X}}$

$$\bar{H}|\Phi_\lambda\rangle = e^{-\hat{X}}\hat{H}e^{\hat{X}}|\Phi_\lambda\rangle = e^{-\hat{X}}\hat{H}e^{\hat{X}}e^{-\hat{X}}|\Psi_\lambda\rangle = e^{-\hat{X}}\hat{H}|\Psi_\lambda\rangle = e^{-\hat{X}}E_\lambda|\Psi_\lambda\rangle = E_\lambda|\Phi_\lambda\rangle$$

$$\text{where } |\Phi_\lambda\rangle = e^{-\hat{X}}|\Psi_\lambda\rangle$$

Thus, the transformed Hamiltonian ($\bar{H}$) has the same eigenvalues (E_λ) as the original Hamiltonian ($\hat{H}$), but it has different eigenstates ($|\Phi_\lambda\rangle = e^{-\hat{X}}|\Psi_\lambda\rangle$). Table 8 provides examples of different types of excitation operators which can be applied in MR-EOM-CC calculations.

Table 8: Operators included in various many body similarity transformations. Labels *i* and *j* indicate inactive orbitals or hole labels, *a* and *b* refer to virtual orbitals or particle labels, and *x, y,* and *z* are active labels referring to orbitals with variable occupation in reference configurations.

Acronym	Operator	Operator Components	Excitation Type
T	$\hat{T}_1$	$t_a^x E_x^a + t_a^i E_i^a$	1p, 1h1p
	$\hat{T}_2$	$t_{ab}^{xy} E_{xy}^{ab} + t_{ab}^{ix} E_{ix}^{ab} + t_{ab}^{ij} E_{ij}^{ab}$	2p, 2p1h, 2p2h
S	$\hat{S}_1$	$s_a^x E_x^a + s_a^i E_i^a$	1p,1h1p
	$\hat{S}_2$	$s_{ax}^{ij} E_{ij}^{ax}$	2h1p
X	$\hat{X}_2$	$x_{ay}^{xj} E_{xj}^{ay}$	1h1p
D	$\hat{D}_2$	$d_{ay}^{ix} E_{ix}^{ay}$	1h1p
U	$\hat{U}_2$	$u_{xy}^{ij} E_{ij}^{xy}$	2h
NI	…	$E_i^x, E_{iz}^{xy}, E_{xy}^{az}$	1h,1p

The $\hat{T}, \hat{S}, \hat{X}, and\ \hat{D}$ operators (see Table 8) describe the various excitations that are included in the MR-EOM calculations - these are referred to with the short hand notation for the MREOM-T|SXD method.[14] The "E" parameters are the excitation operators and the "t" coefficients are the coefficients that require calculation. The detailed transformation first requires transformation of the Hamiltonian on the operator as per: $\bar{H} = e^{-\hat{T}} \hat{H} e^{\hat{T}}$.[14] Then, the similarity transformed Hamiltonian is further modified by operation with $\hat{S}, \hat{X}, \hat{D}$, *i.e.*, $\hat{G} = \{e^{(\hat{S}+\hat{X}+\hat{D})}\}^{-1} \bar{H} \{e^{(\hat{S}+\hat{X}+\hat{D})}\}$. After acting upon the Hamiltonian with these four excitation operators, the only excitations out of the CAS that remain are 1p, 1h, and 2h.

$$\langle \Phi_{\mathrm{X}} | \hat{\mathrm{G}} | \Phi_{\lambda}{}^{\mathrm{CAS}} \rangle = 0 \qquad \text{where x} = \begin{cases} \text{1h1p} \\ \text{2h1p} \\ \text{1h2p} \\ \text{2h2p} \end{cases} \qquad \text{Equation 65}$$

where Φ_X is the wavefunction corresponding to different excitations, $\hat{G}$ is the transformed Hamiltonian for MREOM-T|SXD; and ${\Phi_\lambda}^{CAS}$ is the CAS wavefunction.

Besides the MREOM-T|SXD approach, we employed an another method of calculation: MREOM-T|T$^+$|SXD, which includes an additional transformation - T$^+$:

$$\hat{T}^+ = \sum_{i,a} t_a^i \hat{E}_a^i + \frac{1}{2}\sum_{i,j,a,b} t_{ab}^{ij} E_{ab}^{ij} \qquad \text{Equation 66}$$

This additional de-excitation operator T$^+$ is performed so that the resulting Hamiltonian $\hat{G}$ is approximately Hermitian. The remaining $\hat{S}, \hat{X}, and\ \hat{D}$ transformation steps are similar to that in MREOM-T|SXD approach.[39]

3.2.2.2 Diagonalization Strategy

Following transformation, a diagonalization of the transformed Hamiltonian is performed. As mentioned in the section on transformation strategy (3.2.2.1), the diagonalization space out of the CAS is greatly reduced to the 1p, 1h, and 2h configurations following application of the excitation operators $\hat{T},\ \hat{S},\ \hat{X}, and\ \hat{D}$ or $\hat{T},\ \hat{T}^+, \hat{S},\ \hat{X}, and\ \hat{D}$. Thus, the diagonalization space becomes a very compact subspace. Taking a Co$^+$ cation as an example, we can set the 8 electrons in 12 spin orbitals as the active space (ten 3d spin orbitals and two 4s spin orbitals), and employ 18 electrons in 18 occupied spin orbitals, and 0 electrons in 100 virtual spin orbitals (see Figure 14). There will be $\binom{12}{8} = 495$ combinations of CAS orbitals. For the CAS, there are a variety of excitations (see Table 9). Thus, the diagonalization space out of the CAS can be significantly compacted, such that multireference methods may be effectively applied.

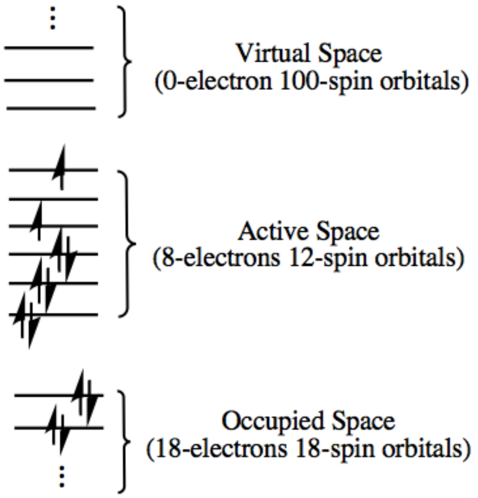

Figure 14. Schematic picture of the configuration of a cobalt cation, Co$^+$, system.

Table 9. The diagonalization space for different excitations out of the CAS of Co$^+$.

Excitations	1h	1p	1h1p	2h	2p	1h2p	1p2h	2h2p
Diagonalization Space	18	100	18×100	$\binom{18}{2}$	$\binom{100}{2}$	$18 \times \binom{100}{2}$	$100 \times \binom{18}{2}$	$\binom{100}{2} \times \binom{18}{2}$
D.S.×$\vert$CAS⟩	8910	5×10^4	9×10^5	8×10^4	2×10^6	4×10^7	8×10^6	4×10^8

3.2.3 Spin-orbit Coupling (SOC)

A charge moving along a circular path produces an orthogonal magnetic field, $\vec{\mu}$, (see Figure 15).[40] Consequently, there is a magnetic field associated with the orbital motion of electrons.

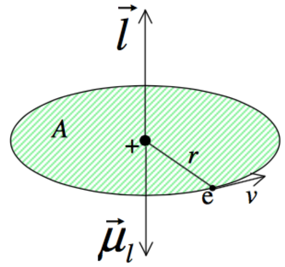

Figure 15: The generation of the magnetic dipole momentum

The magnitude of the magnetic dipole moment $\vec{\mu}$ is:

$$\vec{\mu} = \mathrm{IA} = \frac{(-e)}{T}\pi r^2 \frac{1}{c} = -\frac{er^2\omega}{2c} \quad \text{where } T = \frac{2\pi}{\omega} \qquad \text{Equation 67}$$

where I is the current generated due to the moving charge, A is the area of the loop, r is the radius of the loop, ω is the angular frequency; and T is the period. Because of the magnitude of the orbital angular momentum $|\vec{L}|$ is mvr (or $m\omega r^2$), the magnetic dipole momentum can be rewritten as:

$$\vec{\mu}_l = -\frac{er^2\omega}{2c} = -\frac{e\vec{L}}{2mc} = -\frac{e}{2mc}(\vec{L}_x + \vec{L}_y + \vec{L}_z) \qquad \text{Equation 68}$$

For the intrinsic spin of an electron, the formula is:[41]

$$\vec{\mu}_s = g_e \frac{e}{2m_e c}\vec{S} \qquad \text{Equation 69}$$

The magnetic dipole induced by the orbital motion (μ_l) of the electron can interact with the momentum generated by the electron intrinsic spin (μ_s). This interaction called spin-orbit coupling (SOC).

For diatomic molecules (see Figure 16), the interactions between the orbital and spin angular momenta can be classified as homo-interactions or hetero-interactions (see Table 10). Homo-interactions are defined as interactions between an electron spin and its own orbital angular momentum about the nuclei within the molecule with which they are most closely associated. For example the interaction $\mu_{l,iA}\mu_{s,i}$ is the interaction between the orbital angular momentum that are induced by the electron *i* as it moves around *A* ($i.e., \mu_{l,iA}$) and the spin angular momentum induced by electron *i* ($i.e., \mu_{s,i}$). [42] Hetero-interactions, on the other hand, are defined as the coupling between electron spin and their orbital angular momenta about the remaining nuclei in the molecule, such as the interaction $\mu_{l,iB}\mu_{s,i}$. This is the interaction between the orbital angular momenta that are induced by electron *i* as it moves around B (*i.e.,* $\mu_{l,iB}$), and the spin angular momentum of the electron *i* ($i.e., \mu_{s,i}$). [42]

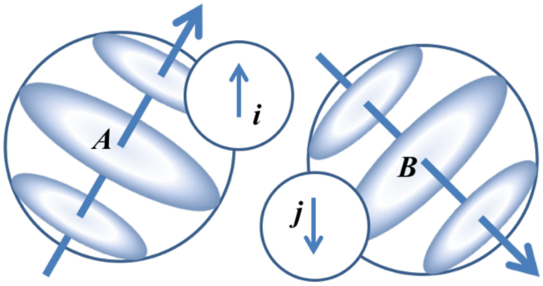

Figure 16. The intra- and inter-atomic spin orbit coupling of electron *i* and *j*.

Table 10. The orbital and spin angular momentum induced in the diatomic molecule system.

Type I	Homo-interaction	$\mu_{l,iA}\mu_{s,i}$ and $\mu_{l,jB}\mu_{s,j}$
Type II	Hetero-interaction	$\mu_{l,iB}\mu_{s,i}$ and $\mu_{l,jA}\mu_{s,j}$

Because the interatomic distance is (usually) larger than the distance between the nuclei and the electrons of the atoms [i.e., $(r_{AB}, r_{Aj}, r_{Bi}) > (r_{Ai}, r_{Bj}, r_{ij})$], SOC depends predominantly on the contributions from the individual atoms, and hetero-interactions can be neglected.[42]

The SOC energies for the individual atoms can be obtained by solving the Schrödinger equation:

$$\widehat{\mathrm{H}}^{\mathrm{spin-orbit}}\,\Psi = \mathrm{E}_{\mathrm{lsj}}\,\Psi \qquad \text{Equation 70}$$

where Ψ is the wavefunction and $\widehat{H}^{spin-orbit}$ is the spin-orbit interaction Hamiltonian.[43]

$$\widehat{H}^{spin-orbit} = \alpha\hat{l}\cdot\hat{s} = \frac{\alpha}{2}\left(\hat{j}^2 - \hat{l}^2 - \hat{s}^2\right) = \frac{\alpha}{2}[j(j+1) - l(l+1) - s(s+1)] \qquad \text{Equation 71}$$

where $\hat{l}$ is the orbital angular momentum, $\hat{s}$ is the spin angular momentum, $\vec{j}$ is the total angular momentum $(\vec{j} = \vec{l} + \vec{s})$, and α is the spin-orbit coupling constant. Thus, the eigenvalue for the spin-orbit energy of a given $|l, s, j\rangle$ level is:[43]

$$\mathrm{E}_{\mathrm{nlsj}} = \frac{\alpha\hbar}{2}[\mathrm{j}(\mathrm{j}+1) - \mathrm{l}(\mathrm{l}+1) - \mathrm{s}(\mathrm{s}+1)] \qquad \text{Equation 72}$$

Energy differences between spin-orbit states arise from the relative alignment of the spin and orbital angular momenta. This phenomenon is known as spin-orbit splitting. Possible J values obey a Clebsch-Gordon series and range from |*l*-*s*| to |*l*+*s*| (see Figure 17). Taking cobalt as an example, the splitting pattern and energies obtained due to the SOC interactions are shown in Figure 18.

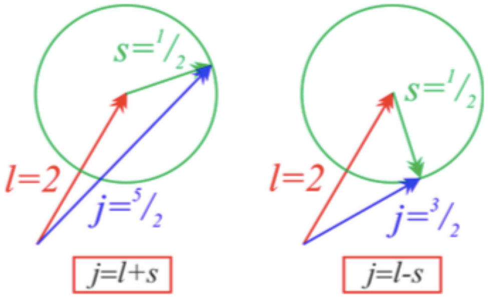

Figure 17: The energy of SOC depends on the relative coupling of the angular and hence on the relative orientation of the angular momenta.[43]

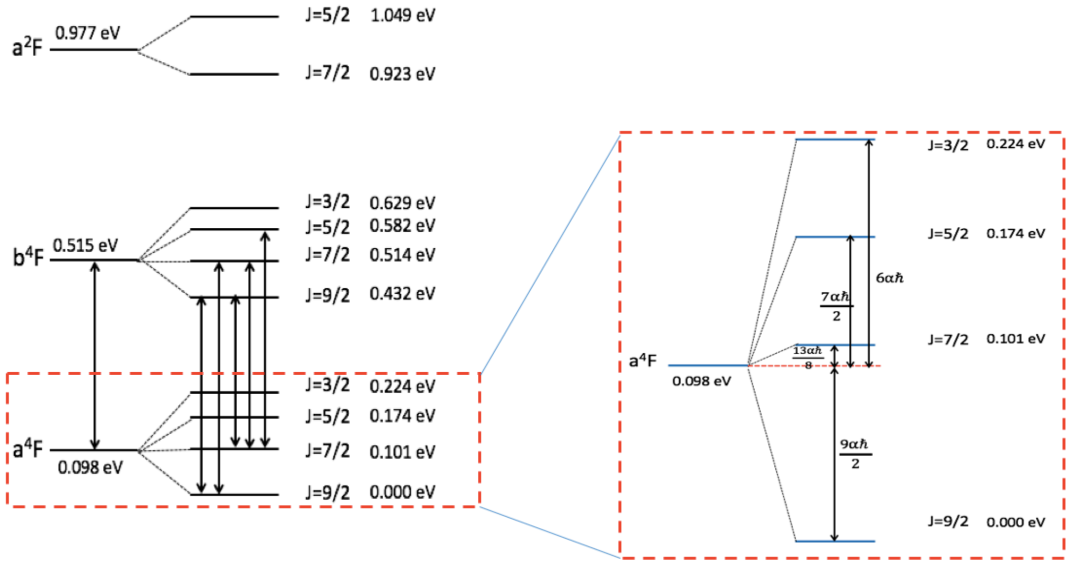

Figure 18: The spin-orbit splitting for three low-energy states of atomic Cobalt.

As can be seen in Figure 18, this spin-orbit interaction causes around 0.1 eV energy splitting among different J values in this cobalt system, which is significant in atomic cobalt system, and it expected to be similarly important in Co-containing systems. Thus, the SOC should implement in the further calculations.

3.2.4 Scalar Relativistic Effects

Accounting for relativistic effects is necessary for accurate theoretical treatment of heavy elements (like cobalt in this project). Owing to the high effective nuclear charge that is experienced by electrons that penetrate to the nucleus, the inner core electrons are traveling at a significant fraction of the speed of light, which leads to a relativistic increase in the electron mass:[44]

$$m = \frac{m_0}{\sqrt{1-(v^2/c^2)}} \qquad \text{Equation 73}$$

In equation 73, *m* is the relativistic mass of electron, m_0 is the mass of electron at zero velocity, *v* is the velocity of the electron, and *c* is the speed of light. To account for this scalar relativistic effect, the Douglas-Kroll-Hess (DKH) correction is employed in calculations of the cobalt-containing systems that are studied in this thesis.[44]

3.2.5 Ro-vibrational Structure

In a one-dimensional or effective radial potential, the number, energies and properties of vibration-rotational levels can be determined by solving the one-dimensional Schrödinger equation:[45]

$$-\frac{\hbar^2}{2\mu}\frac{d^2\Psi_{v,J}(r)}{dr^2} + V_J(r)\Psi_{v,J}(r) = E_{v,J}\Psi_{v,J}(r) \qquad \text{Equation 74}$$

where μ is the reduced mass of the system, r is the internuclear distance, and *v* and *J* are the vibrational and rotational quantum numbers, respectively. The $-\frac{\hbar^2}{2\mu}\frac{d^2\Psi_{v,J}(r)}{dr^2}$ term is the kinetic energy while the $V_J(r)$ term describes the effective one-dimensional potential. The $V_J(r)$ consists of two parts; the electronic potential ($V_{e,J}$) and the centrifugal potential, $V_{c,J}$:

$$V_{c,J}(r) = [J(J+1) - \Omega^2]\hbar^2/2\mu r^2 \qquad \text{Equation 75}$$

where Ω is the projection of the electronic angular momentum onto the internuclear axis. To solve Equation 75, the Cooley eigenvalue convergence method is used.[45] In this method, the numerical integration at a given trial energy proceeds outward from the (user defined) minimum interatomic distance while at the same time, this numerical integration process moves inward from the maximum distance until they meet at one point (see Figure 19). If the difference in the slopes of these inward and outward functions slopes is zero (actually, less than the chosen convergence criterion), the calculation is finished and the eigenvalues, $E_{v,J}$, and eigenfunctions, $\Psi_{v,J}(r)$, of the potential $V_J(r)$ are determined.

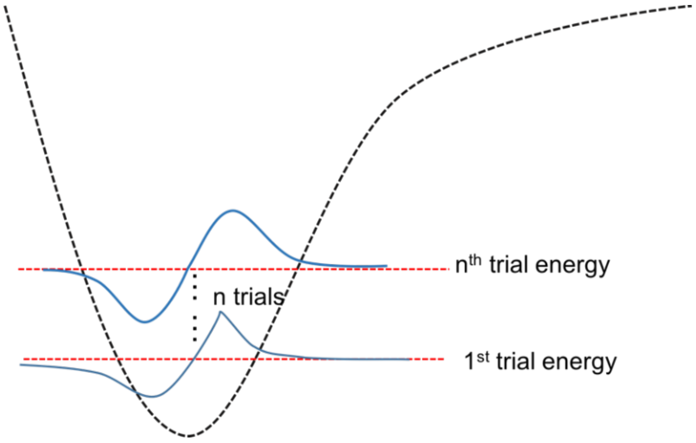

Figure 19. The convergence procedure to find the eigenvalues of a given potential.

Upon determining the energies of the corresponding vibrational levels, a plot of these energies (G_v) versus the corresponding vibrational level quantum number ($v + {}^1\!/_2$) is constructed and fit with a polynomial trend line. The higher the order of the polynomial function, the higher the accuracy of the simulation; however, computational cost also increases. Thus, a six-order polynomial function is typically selected based on the balance of accuracy and computational cost. The coefficients of these polynomial functions are the vibrational constants for the given electronic state:[43]

$$G_v = \omega_e\left(v + {}^1\!/_2\right) - \omega_e x_e\left(v + {}^1\!/_2\right)^2 + \omega_e y_e\left(v + {}^1\!/_2\right)^3 + \cdots \qquad \text{Equation 76}$$

Similarly, one can extract the rotational constants by fitting rotational energies, F(J), as a function of [J(J+1)] with a six-order polynomial fit:.[43]

$$F_J = B_J[J(J+1)] + D_J[J(J+1)]^2 + H_J[J(J+1)]^3 + \cdots \qquad \text{Equation 77}$$

Thus, the calculated vibrational constants and the rotational constants can be used to compare with the experimental measurements.

3.3 MRCI calculation of Co^+•Ar

In this section, the MRCI calculations of the electronic states of Co^+•Ar are discussed. Since the heavier RG (Ar-Xe) species may exhibit charge transfer and incipient chemical bonding, we start the investigation from Co^+•Ar. Section 3.3.1 describes the computational details of the calculation. In section 3.3.2 shows the calculation results and discussions.

3.3.1 Computational details

MRCI/Def2-TZVPPD calculations of Co^+•Ar were carried out with the Molpro 2010.1 program.[46] The basis set chosen for our study was Def2-TZVPPD (described in section 2.2.1.2) based on the study of Hellweg *et. al*.[47] Since the Def2-TZVPPD basis set is not implemented internally in Molpro, it is constructed from user input based on the parameters from the EMSL basis set exchange.[48] To begin, the unrestricted Hartree-Fock (UHF) method was chosen to determine the single configuration wavefunction of the ground state. After the UHF calculation, the multi-configurational wavefunction was generated using the CASSCF method. Finally, the MRCI calculations, which includes the correlation energy calculation, were performed based on the reference wavefunction from the CASSCF calculation.[49] In order to improve the accuracy of the MRCI calculation, the Davidson correction (see section 2.2.3), corrections for scalar relativistic effects corrections (described in section 3.2.4), and corrections for SOC interactions (see section 3.2.3) were included in the computational treatment.[49]

The PECs of Co^+•Ar were obtained from single-point energy calculations over a bond length range of 2 Å to 10 Å. Before scanning from 2 Å to 10 Å, a single-point electronic state calculation of $Co^+ \bullet Ar$ ($d_{Co^+-Ar} = 10$ Å) was conducted to ensure the validity of the PECs scan by comparing the resulting relative energies of the individual electronic states of the dimer at long range to the experimental electronic energies of Co^+. The underlying assumption here is that the interaction between the Ar atom and the Co^+ can be neglected at a distance of 10 Å and that the "molecular" electronic energies at this internuclear distance are representative of the internal energy level structure of the atomic Co^+ cation. The experimental data for the internal energies of Co^+(see Table 11) were taken from the atomic tables of the National Institute of Standards and Technology (NIST) website.[9]

Two electronic configurations for the Co^+ cation were considered: $3d^8$ and $3d^7 4s$. Due to limitations of the Molpro program, these two electronic configurations were treated independently. For the $3d^8$ configuration, the a^3F state was selected in the CASSCF calculation to generate the multi-configuration wavefunction. Then, the a^3F, a^1D, and a^3P states were included in the MRCI calculation. For the $3d^7 4s^1$ configuration, a state-average CASSCF was performed for the a^5F and b^3F states to build the multi-configurational wavefunction. Then, the a^5F, b^3F, and a^5P states were considered in the MRCI calculation. A sample input file for this calculations is shown in Appendix 1. To plot the PECs of these two configurations simultaneously, the PECs of $3d^7 4s$ configuration were positioned such that the dissociation threshold matched the corresponding experimental electronic energy levels of Co^+.

Table 11: The relative energy levels of Co^+ as tabulated by NIST.[9]

Configurations	Term	J	Level (eV)
$3d^8$	a^3F	4	0.000
		3	0.118
		2	0.198
$3d^74s$	a^5F	5	0.415
		4	0.499
		3	0.566
		2	0.614
		1	0.645
$3d^74s$	b^3F	4	1.217
		3	1.328
		2	1.404
$3d^8$	a^1D	2	1.445
$3d^8$	a^3P	2	1.644
		1	1.662
		0	1.685
$3d^74s$	a^5P	3	2.203
		2	2.236
		1	2.274

3.3.2 Results and Discussion

Assuming that the interaction between the Ar atom and the Co^+ cation can be neglected at a distance of 10 Å, the energies of the various electronic states of $Co^+ \bullet Ar$ ($\mathrm{d}_{Co^+-Ar} = 10$ Å) from MRCI+Q/Def2-TZVPPD calculations should be comparable with the experimentally determined internal energies of Co$^+$ (given in Table 12). While the relative energies within a given configuration (*i.e.* $E_{a^5F(10Å)} - E_{a^3F(10Å)}$) are calculated fairly accurately,[9] the absolute energy difference between the two configurations is calculated to be 0.6218 eV, which is inconsistent with the experimental value of 0.5150 eV. This error might be corrected by accounting for the SOC effect, or it might arise due the difficulty of treating the a^{3}F and a^{5}F electronic states simultaneously.

Table 12: The comparison between experimental Co$^+$ energies (eV) and calculated $Co^+ \bullet Ar$ ($d_{Co^+\cdot Ar} = 10$ Å) internal energies in MRCI+Q/Def2-TZVPPD level of theory using the Molpro program.

$Co^+(d^8)\cdot Ar$					$Co^+(3d^7 4s)\cdot Ar$				
Term	J	E_{Calc}	E_{NIST}	%Diff	Term	J	E_{Calc}	E_{NIST}	%Diff
a^{3}F	4	0	0	0	a^{5}F	5	0	0	0
	3	0.1202	0.1178	2.04		4	0.0838	0.0841	0.36
	2	0.2051	0.1980	3.59		3	0.1525	0.1501	1.60
a^{1}D	2	1.4900	1.4446	3.14		2	0.2046	0.1983	3.18
a^{3}P	2	1.7533	1.6441	6.64		1	0.2397	0.2299	4.26
	1	1.7878	1.6619	7.58	b^{3}F	4	0.8709	0.8012	8.70
	0	1.8199	1.6854	7.98		3	0.9834	0.9123	7.79
						2	1.0671	0.9883	7.97
					a^{5}P	3	1.8883	1.7880	5.61
						2	1.9356	1.8202	6.34
						1	1.9672	1.8583	5.86

The fact that the calculated relative electronic energies for the separate atom limits of $Co^{+} \bullet Ar$ are in good agreement with the experimental values indicates that the MRCI+Q/Def2-TZVPPD method is a reasonable choice for the construction of the PECs of the $Co^{+} \bullet Ar$ system.[9] However, the calculated low-energy PECs for $Co^{+} \bullet Ar$ exhibited a great deal of unexpected structure (see Figure 20).

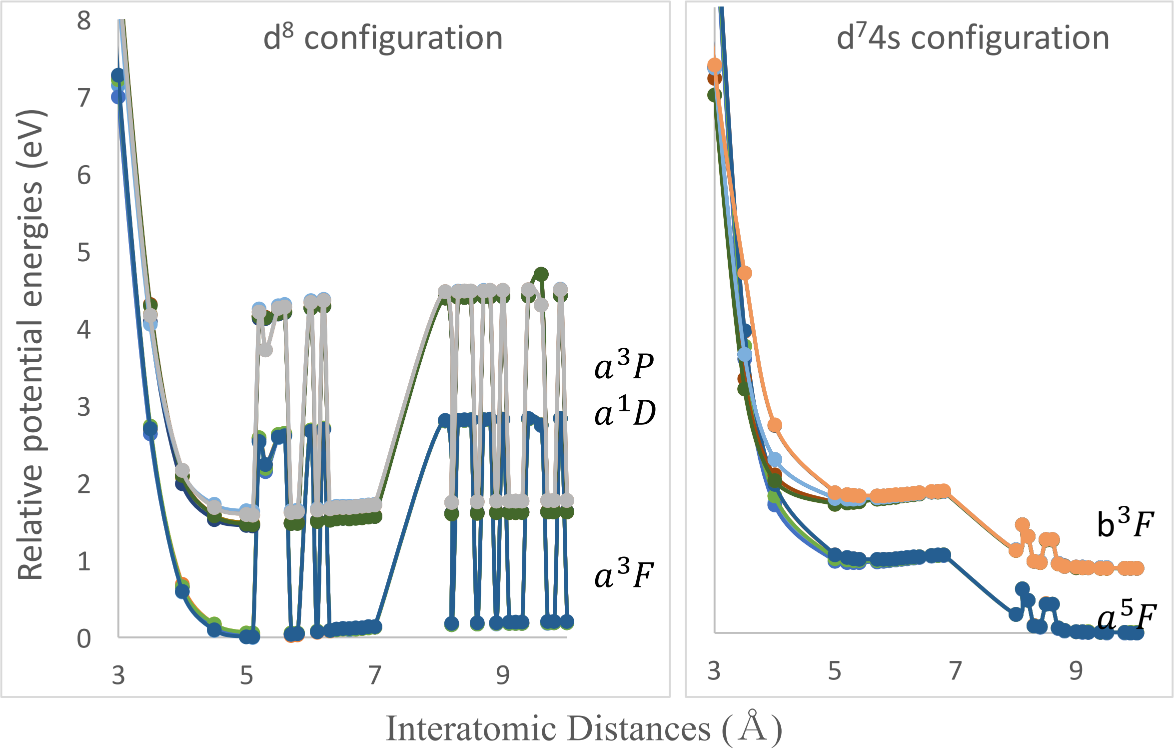

Figure 20: The PECs of Co^{+}•Ar as calculated by MRCI+Q/Def2-TZVPPD using the Molpro program.

To explore the reason for the unexpected behavior of the PECs, the CASSCF calculation results were plotted, which is shown in Figure 21. These discontinuous PECs from CASSCF calculation indicates that the failure of MRCI+Q calculation is due to the selection of CAS for the Co^{+}•Ar system. This unsuccessful selection of CAS causes the calculations to converge to the wrong states. To date, we have not found the solution to this problem.

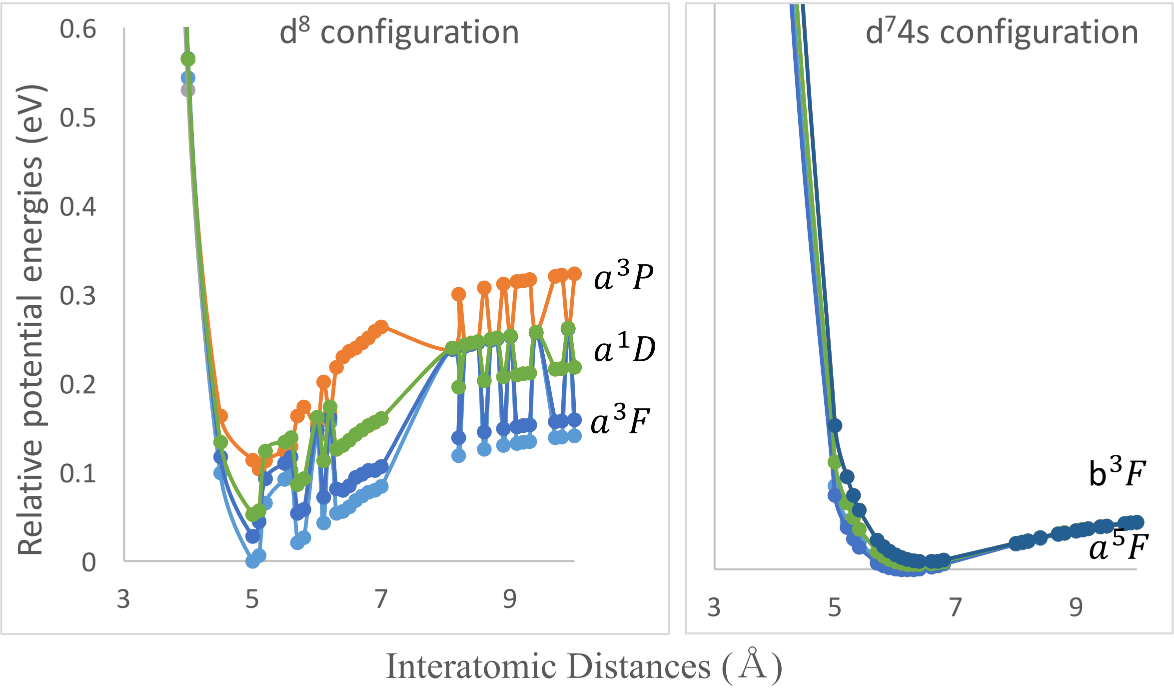

Figure 21: The PECs of Co$^+$•Ar as calculated by CASSCF/Def2-TZVPPD using the Molpro program.

3.4 MR-EOM-CCSD calculation of $Co^+ \cdot Ar$

There are three steps necessary to conduct MREOM-CCSD calculations in the ACESII and ORCA programs. One must first determine the active space, then perform the state-average CASSCF calculation, and, finally, carry out the final MREOM-CCSD calculation. The Davidson correction is no longer needed in these calculations due to the nature of coupled cluster theory (described in *section 2.2.4*).[50] Although MREOM-CCSD calculations can be conducted in either the ACESII or ORCA programs, the ORCA program has two technical advantages over the ACESII program: the inclusion of the SOC calculation and the ability to simultaneously treat electronic states from different electronic configurations. In principle, ACESII can deal with both 3d^8 and 3d^{7}4s configurations simultaneously as well; however, we have not found a way to implement this to date. One important thing to be noted is that the MREOM-T|SXD (see *section 3.2.2.1*) calculation is carried out in ACESII program while the MREOM-T|T^+|SXD calculation (described in *section 3.2.2.1*) is performed in the ORCA program because ORCA can only deal with a Hermitian matrices whereas ACESII can solve the non-Hermitian matrix.

In section 3.4.1, the MREOM-T|SXD calculations of $Co^+ \bullet RG$ $(RG = He, Ar, Kr)$ via ACESII program are illustrated. Section 3.4.2 discussed the MREOM-T|T^+|SXD calculations of Co^+•RG (RG=Ar, Kr, Xe), CM^+•Ar (CM= Ag, Au) in ORCA program.

3.4.1 Preparation for the Calculation

Before probing the PECs of the selected metal-rare gas cationic clusters, four trial calculations were performed on $Na^+ \bullet Ar$ (a system suitable for single reference description) to ensure the validity of our MREOM-CCSD calculations. First, two trial calculations, one at the CCSD level of theory and one at the CCSD(T) level of theory, were conducted to determine if triple excitations should be included in the MREOM-T|T^+|SXD calculation. Then, calculations with and without the counterpoise correction were conducted to assess the importance of BSSE (defined in *section 2.2.1.3*, see Figure 22). In comparing the $Na^+ \bullet Ar$ PECs as calculated at the CCSD and CCSD(T) levels of theory, we find that there is very little difference. This indicates the easier CCSD calculation can be used to decrease the computational cost. Interestingly, the counterpoise correction that is calculated for $Na^+ \bullet Ar$ is 0.0424 eV, which is a substantial 28.4 % correction to the dissociation energy. Moreover, since the BSSE correction increases significantly with decreasing internuclear separation (as expected; see Figure 23), including counterpoise correction should significantly decrease the theoretical dissociation energy. Owing to the fact that BSSE is expected to have such a major impact on the calculation results, counterpoise corrections were applied in all subsequent calculations.

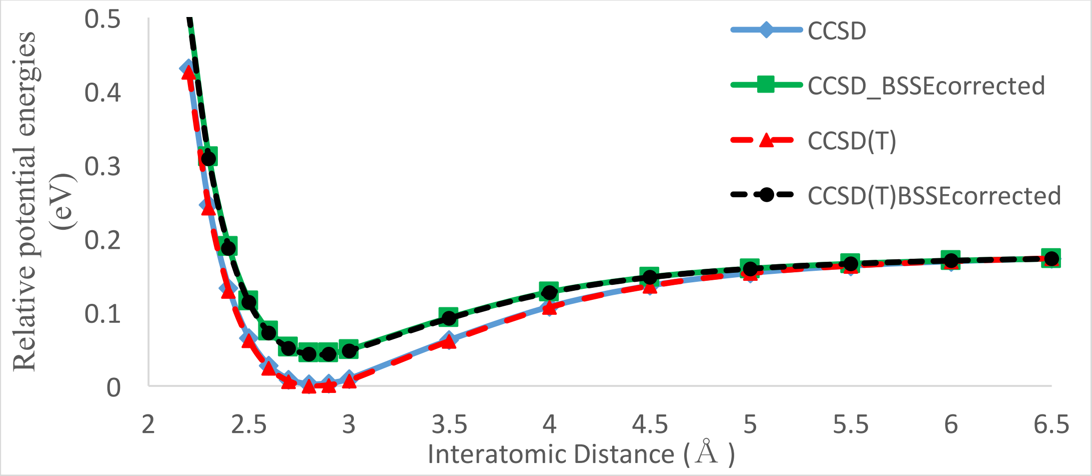

Figure 22: The CCSD/Def2-TZVPPD and CCSD(T)/Def2-TZVPPD calculation of $Na^{+} \bullet Ar$ system with/without the counterpoise correction using the ACESII program. Blue curve corresponds to the CCSD/Def2-TZVPPD calculation without the counterpoise correction while the Green curve corresponds to the CCSD/Def2-TZVPPD calculation after the counterpoise correction. Red dashed curve stands for the CCSD(T)/Def2-TZVPPD calculation without the counterpoise correction while the Black dashed curves represents for the CCSD(T)/Def2-TZVPPD calculation after the counterpoise correction.

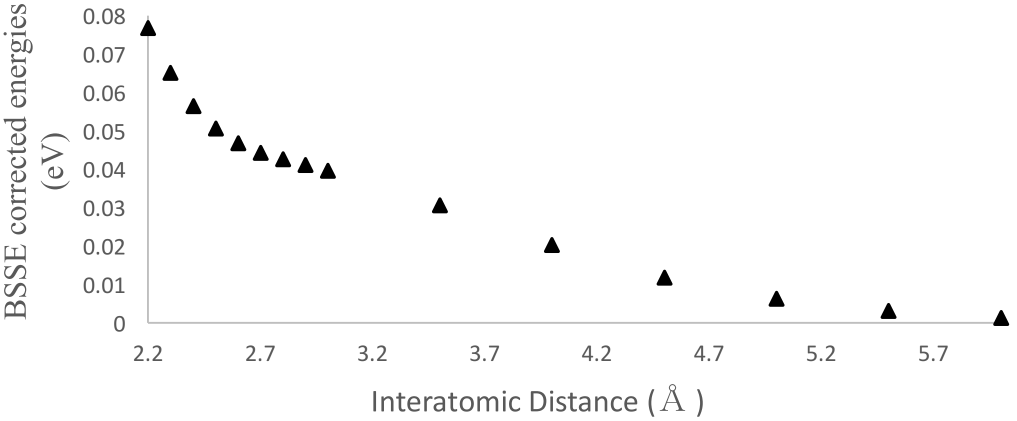

Figure 23: The BBSE correction energies for $Na^{+} \bullet Ar$ system in CCSD/Def2-TZVPPD calculation using the ACESII program.

3.4.2 Investigation of cobalt clusters with ACESII

3.4.2.1 Computational Details

MREOM-T|SXD/Def2-TZVPPD calculations of the electronic states of Co^+•RG (RG= He, Ar, Kr) were performed using the ACESII program. A sample calculation input file of Co^+•Ar is provided in Appendix 2. It is the heavier RG species (Ar-Xe) that are of particular interest, since these may exhibit charge transfer and incipient chemical bonding. However, Co^+•He is the easiest calculation that we can do, so this is where we began our investigation. The calculated electronic energies of various electronic states at 10 Å were then compared with the experimental electronic energies of Co^+. Owing to the fact that the SOC calculation has not been implemented in the ACESII program, the experimental electronic energies of a particular L-S multiplet were instead averaged over the corresponding J values for comparison with computed results (see Equation 78).

$$\mathrm{E_{LS}} = \frac{\sum_{\mathrm{J \in LS}} \mathrm{E_J} \cdot (2\mathrm{J}+1)}{\sum_{\mathrm{J \in LS}} (2\mathrm{J}+1)} \qquad \text{Equation 78}$$

where L, S, and J are the orbital angular momentum quantum number, the spin angular momentum quantum number, and the total angular momentum quantum number, respectively. For example, the energy of a^3F state of cobalt is calculated as:

$$E_{L=3,S=1} = \frac{E_4 \cdot (2\times4+1) + E_3 \cdot (2\times3+1) + E_2 \cdot (2\times2+1)}{(2\times4+1)+(2\times3+1)+(2\times2+1)} = \frac{0.0\times9+0.118\times7+0.198\times5}{9+7+5} = 0.086 \text{ eV}$$

Therefore, these averaged electronic energies of Co^+ are compared with our calculated energies and the comparison results are provided in the following section.

3.4.2.2 Results and Discussion

Assuming that the interactions between the RG atom and Co^+ are negligible at a distance of 10 Å, the relative energies of the various electronic states of Co^+•RG (RG = He, Ar, Kr) at 10 Å should be comparable to the internal energies of the Co^+ atomic cation. The results of the MREOM-T|SXD/Def2-TZVPPD calculations for these species, as well as the experimentally measured electronic energies of Co^+, are provided in Table 13. The calculated absolute energy differences between the $3d^74s$- and $3d^8$-configurations (*i.e.,* $E_{a^5F(10Å)} - E_{a^3F(10Å)}$) of Co^+•Ar (RG=He, Ar, Kr) were 0.1920 eV, 0.1949 eV, and 0.2054 eV, respectively. These are markedly different from the experimental value of 0.5150 eV. In the MRCI calculation of Co^+•Ar ($\Delta E = 0.6218$ eV; described above) the energy difference was *ca.* +0.2 eV. By comparing these energies with experimental values, we find that the both MRCI and MREOM-T|SXD approaches exhibit a large deviation. To further investigate the source of errors, the integration of the a^3F and a^5F electronic states and the inclusion of the SOC correction were explored.

Table 13: Comparison between the experimental Co^+ energies and calculated $Co^+ \cdot RG$ ($d_{Co^+-RG} = 10$ Å) energies of various states (eV) at the MREOM-T|SXD/Def2-TZVPPD level of theory using the ACESII program.

Configurations	Term	$E_{Co^+(NIST)}$	$E_{Rela\_Co^+}$	$E_{Rela\_Co^+\cdot He}$	$E_{Rela\_Co^+\cdot Ar}$	$E_{Rela\_Co^+\cdot Kr}$
$3d^8$	a^3F	0.000	0.000	0.000	0.000	0.000
	a^1D	1.359	1.358	1.389	1.392	1.392
	a^3P	1.569	1.568	1.540	1.544	1.544
	a^1G	2.266	2.266	2.303	2.305	2.305
$3d^74s^1$	a^5F	0.515	0.515	0.515	0.515	0.515
	b^3F	1.298	1.298	1.280	1.280	1.280
	a^5P	2.228	2.228	2.231	2.236	2.236

As can be seen in Table 13, the calculated relative potential energies of the $3d^8$ and $3d^74s$ separated atom limits matches well with the corresponding J-averaged NIST values for Co^+ internal energies. This indicates that the MREOM-T|SXD method is a good selection for the construction of the PECs of the Co^+•RG (RG= He, Ar, Kr) systems. Figure 24 shows the PECs that are associated with the $3d^8$ and $3d^74s$ configurations of Co^+•RG (RG= He, Ar, Kr). The PECs for the $3d^8$ and $3d^74s$ configurations were merged by setting the relative position of the $3d^74s$ configuration a^5F dissociation threshold to the relative energy of the a^5F state in Co^+ ($3d^74s$) (i.e., 0.429eV above the a^3F state in Co^+ ($3d^8$)). The merged PECs are shown in Figure 25.

A. $Co^+ \cdot He$

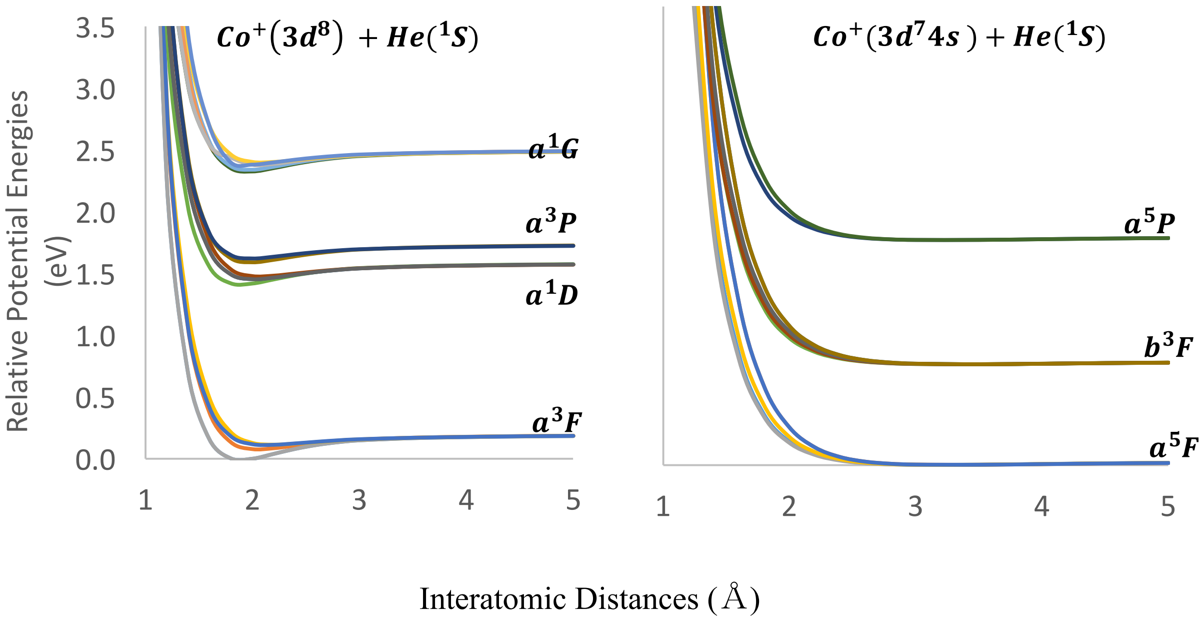

B. $Co^{+} \cdot Ar$

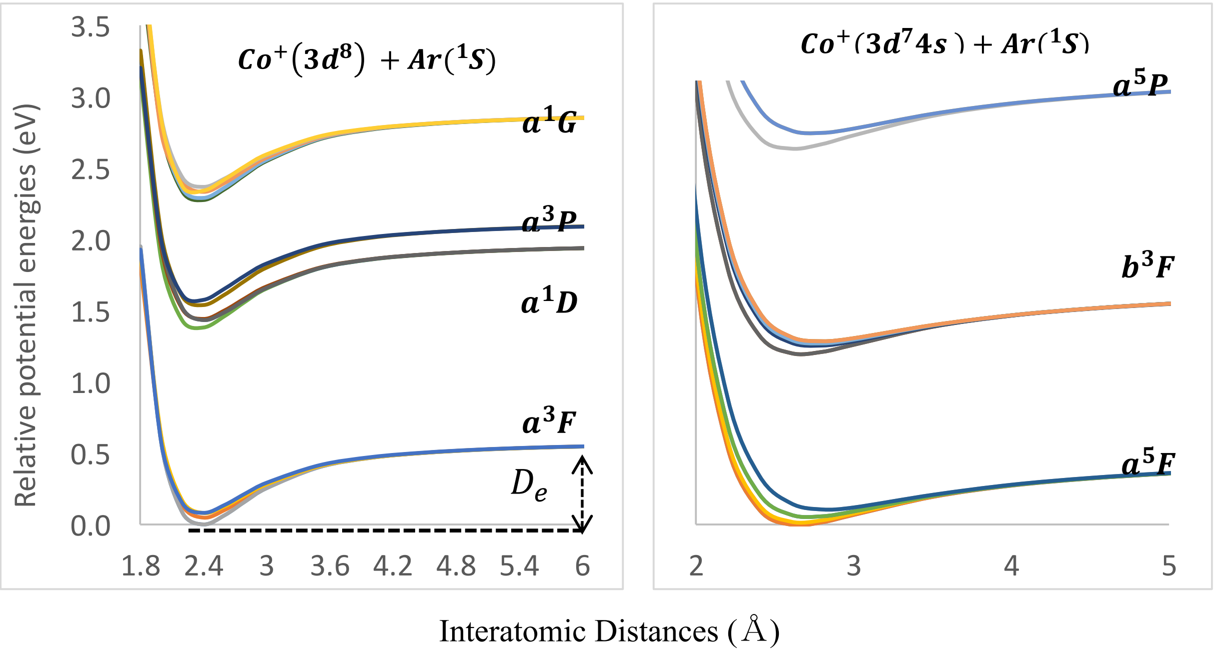

C. $Co^{+} \cdot Kr$

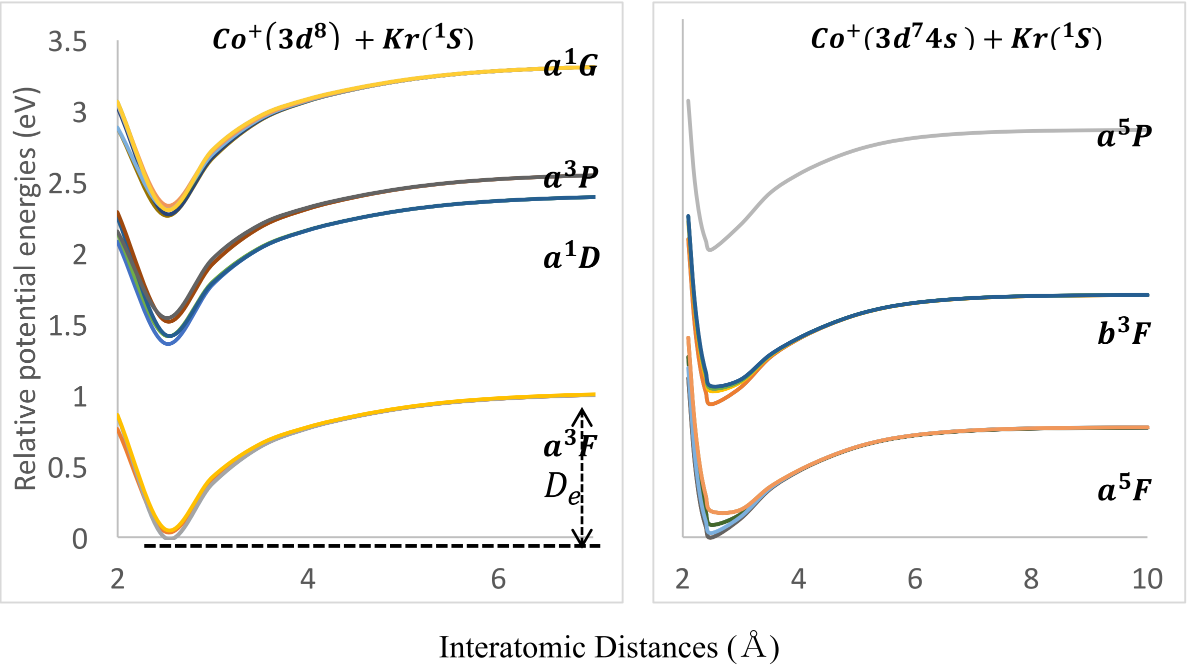

Figure 24. The potential energy curves of $Co^{+}(3d^{8}) \bullet RG$ (left) and $Co^{+}(3d^{7}4s) \bullet RG$ (right) as calculated by MREOM-T|SXD/Def2-TZVPPD using the ACESII program.

A: $Co^{+} \cdot He(^{1}\boldsymbol{S})$

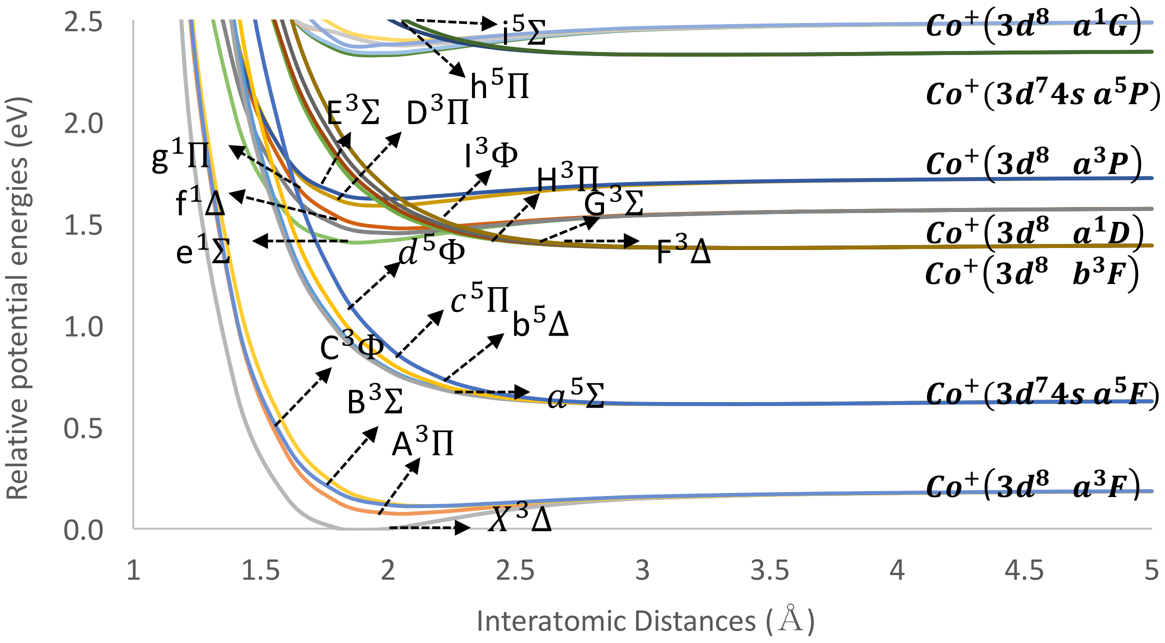

B: $Co^+ \cdot Ar(^1\boldsymbol{S})$

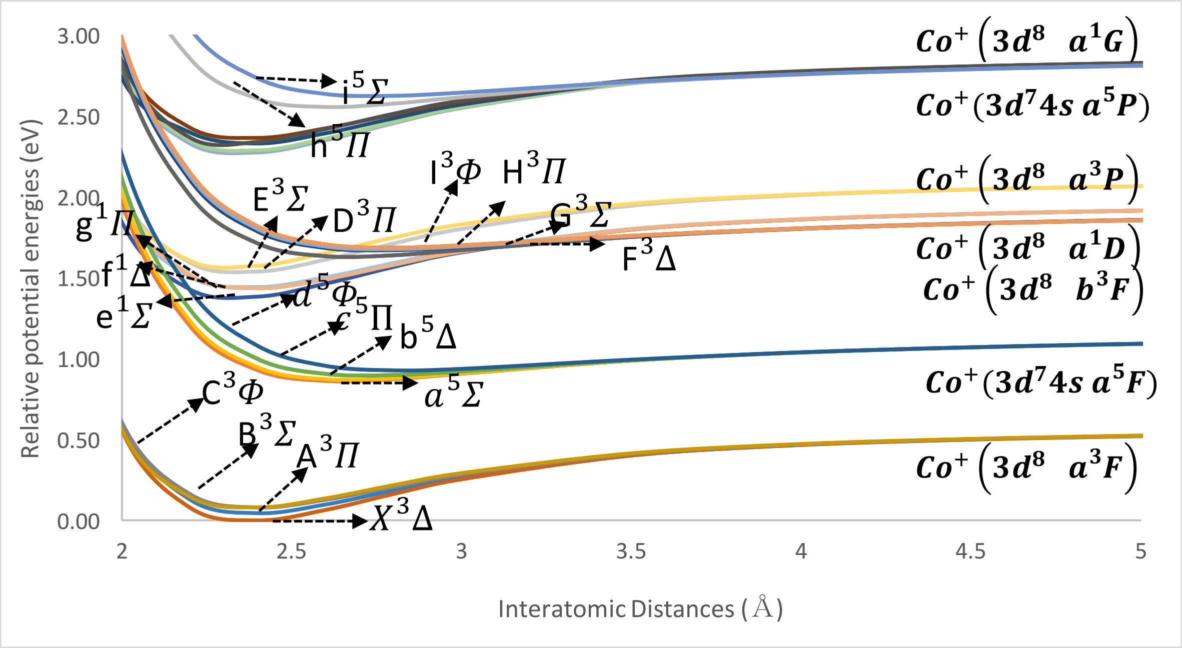

C: $Co^+ \cdot Kr(^1\boldsymbol{S})$

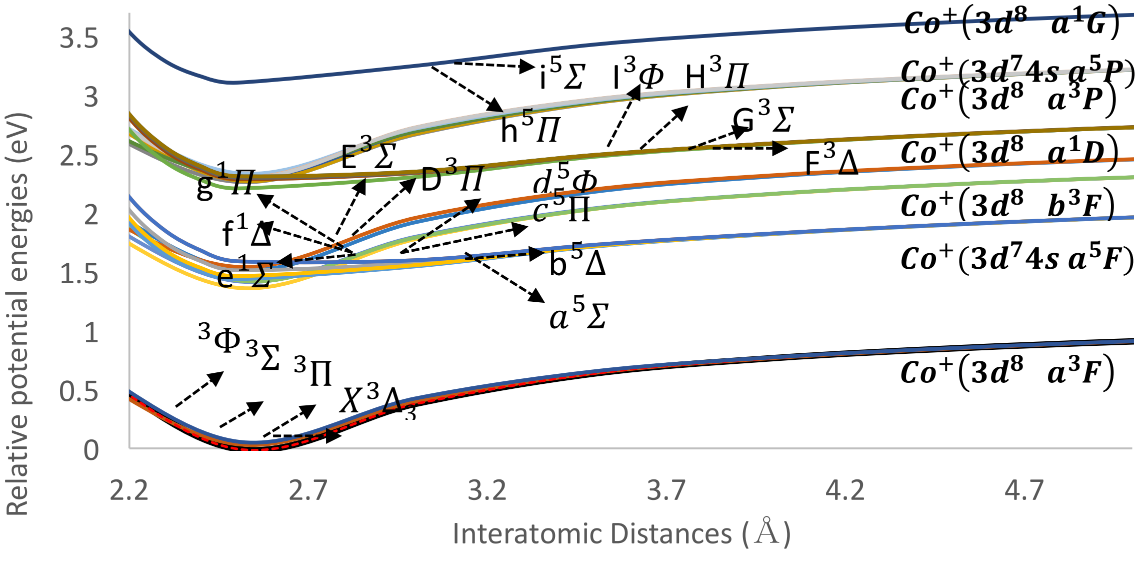

Figure 25: The potential energy curves of $Co^+ \bullet RG$ $(RG = He, Ar, Kr)$ as calculated by MREOM-T|SXD/Def2-TZVPPD using the ACESII program; these electronic states are represented by molecular term symbol $(^{2S+1}\Lambda_\Omega)$. The ground state $^3\Delta_3$ is correlated with the $Co^+(3d^8\ a^3F) + RG(^1S)$ separated atom limit.

The dissociation energies, D_e, of Co^+•RG (RG= He, Ar, Kr) are obtained by subtracting the molecular energy at R_e from the energy at a large internuclear separation (10 Å).[49] These values are provided in Table 14. The experimentally determined dissociation energies (as described in Chapter 1) are also given in Table 14 for comparison purposes.[49] Two conclusions can be drawn from the data in Table 14. Firstly, the equilibrium bond length of Co^+•RG (RG= He, Ar, Kr) increases from He to Kr, which is consistent with experimental measurements and expectations. Secondly, the increasing interatomic distance of the Co^+•RG (RG= He, Ar, Kr) series is slightly less than the increase in the van der Waals radii of the RG (RG= He, Ar, Kr) series. This suggests that there may be an increasing chemical (*i.e.*, charge transfer) component to Co^+•RG (RG= He, Ar, Kr) binding with increasing RG mass/size. To further explore this possibility, one can estimate the physical interactions between Co^+ and the RG atoms that arise due to the polarizability (α) of the rare gases. The increasing polarizability of the RG atoms from He to Kr leads to stronger ion-induced dipole interactions in Co^+•RG down the RG group. The ion-induced dipole interaction potential ($V_{ion-induced\ dipole}$) is:[51]

$$V_{\mathrm{ion-induced\ dipole}}(\mathrm{r}) = -\frac{\mathrm{e}^2\alpha}{2(4\pi\varepsilon_0)^2\mathrm{r}^4} \qquad \text{Equation 79}$$

where e is the fundamental charge, α is the atomic polarizability, and r is the interatomic distance. For completeness, the classical dispersion energy, V_{disp}, which is the interaction between the induced-dipole of the rare gas and the induced-dipole of the cobalt cation, can be calculated as per the formula:

$$V_{\mathrm{disp}}(\mathrm{r}) = -\frac{C_6}{\mathrm{r}^6} \qquad \text{Equation 80}$$

where

$$C_6 = \frac{3\alpha_{RG}\alpha_{Co^+}}{2(4\pi\varepsilon_0)^2} \cdot \frac{I_{Co^+} \cdot I_{RG}}{I_{Co^+} + I_{RG}}$$

where, I is the ionization energy for the atom. Thus, the total classical (*i.e.*, electrostatic) binding energy of Co^+•RG (RG= He, Ar, Kr) is calculated as the sum of the dispersion energies and the inductive energies. is the results of these calculations are given in Table 15.

Table 14: The equilibrium bond length and dissociation energies of $Co^+ \bullet$ RG comparison.

Co^+•RG	R (Å)					$D\,(eV)$			
	VdW	Calc.	Exp.[52, 6]	Diff	%Diff	Calc.	Exp.[52, 6]	Diff	%Diff
Co^+•He	1.40	1.899	1.87±0.3	0.03	1.55	0.1837	0.131 ±0.002	0.0527	40.22
Co^+•Ar	1.88	2.366	2.385	0.02	0.79	0.5621	0.5097	0.0524	10.29
Co^+•Kr	2.02	2.488	2.447	0.04	1.67	1.0109	0.6701	0.3408	50.85

Note: The experimental measurements are R_0 and D_0 while those calculated are R_e and D_e

Table 15. The polarizability and the binding energies (in eV) of the $Co^+ \bullet$ RG $(RG = He, Ar, Kr)$. The experimental interatomic distances of $Co^+ \bullet$ RG are applied in the calculation.

$Co^+ \cdot$ RG species	$\alpha_{Co^+} + \alpha_{\mathrm{RG}}$(au)[53,54]	$E_{\text{Dispersion Energies}}$	$E_{\text{Inductive}}$	$E_{\text{Total Binding}}$
$Co^+ \cdot He$	8.25+1.3838	0.1537	0.1173	0.2710
$Co^+ \cdot Ar$	8.25+11.091	0.2315	0.3902	0.6217
$Co^+ \cdot Kr$	8.25+16.740	0.2341	0.4816	0.7157

Comparing the experimentally determined binding energies with those from classical electrostatic calculations for Co^+•He, Co^+•Ar, and Co^+•Kr, it can be concluded that the quantum mechanics model is more suitable for this cobalt-helium/argon system since the deviation for classical model is approximately 0.13 eV while that for quantum model is generally less than 0.1eV. For the krypton complex, however, classical result seems better, which may due to complexity of krypton's electronic structure.

A final thing to note here is the absolute and relative errors between the calculated and experimentally determined values of equilibrium interatomic distance and dissociation energy. The calculated interatomic distances of $Co^+ \bullet RG(RG = He, Ar, Kr)$ are in good agreement with the experimental measurement. However, the discrepancy in the dissociation energies of the $Co^+ \bullet RG(RG = He, Ar, Kr)$ series is relatively large. The possible explanations that could account for these differences is that the SOC is ignored by calculations in the ACESII program. Including SOC would generate a high density of electronic states for $Co^+ \cdot RG$, which could mix and therefore affect the accuracy of the calculations.

3.4.3 Investigation of selected metal-rare gas clusters with ORCA

3.4.3.1 Computational Details

MREOM-T|T^+|SXD/Def2-TZVPPD calculations of the electronic states of $Co^+ \cdot Ar$ were also performed using the ORCA program to compare with the results obtained using the ACESII program. A sample calculation input file is provided in Appendix 3. Importantly, the SOC interaction is treated in the ORCA code, and ORCA can treat both the ^{3}F state in the $3d^8$ configuration and the ^{5}F state in the $3d^7 4s^1$ configuration of $Co^+ \bullet RG$ simultaneously.

Consequently, two types of reference states can be generated: the lowest energy level in each of the $3d^8$ and $3d^7 4s^1$ configurations (*i.e.*, ^3F in $3d^8$ and ^5F in $3d^7 4s$), or the combined result of separate $3d^8$ and $3d^7 4s^1$ calculations. Two types of MREOM-T|T$^+$|SXD approaches can also be compared to pursue higher accuracy, *mreom*, which involves 1p, 1h, and 2h excitations and the *mreom_ph*, which includes an extra 1p1h excitation.

In addition to the Co^+•Ar system, the Co^+•Kr, Co^+•Xe, Ag^+•Ar, and Au^+•Ar systems were also explored since these species have previous single reference calculation results, which can be used to assess the validity of the multireference methods. Whereas the state-average CASSCF calculation was conducted for $Co^+ \bullet Ar$, $Co^+ \bullet Kr$, Co^+•Xe and $Ag^+ \bullet Ar$, the state-average RASSCF calculation (*defined in section 3.2.1*) was conducted for Au^+•Ar due to the complexity introduced by the extra orbitals of Au^+(*i.e.*, 6p orbital) that must be included in the active space. In the $Au^+ \cdot Ar$ calculation the number of holes in RAS1 was set to zero, so that no electron can be active from the RAS1 orbitals; furthermore, the number of particles in RAS3 was set to three so that no more than three electrons can be promoted to the RAS3 orbitals because these are the dominant excitations (see Figure 26). It should also be noted that counterpoise correction was introduced (see section 2.2.1.3) for all species to account for BSSE.

Table 16: The internal energies of Ag^{+}as tabulated by NIST[9]

Configuration	Term	J	Level (eV)
$4d^{10}$	^{1}S	0	0.0000
$4d^{9}5s$	$^{2}[5/2]$	3	0.4154
		2	0.4995
$4d^{9}5s$	$^{2}[3/2]$	1	1.2166
		2	1.3277

Table 17: The internal energies of Au^{+}as tabulated by NIST[9]

Configuration	Term	J	Level (eV)
$5d^{10}$	^{1}S	0	0.0000
$5d^{9}6s$	^{3}D	3	1.8647
		2	2.1872
		1	3.4425
$5d^{9}6s$	^{1}D	2	3.6726

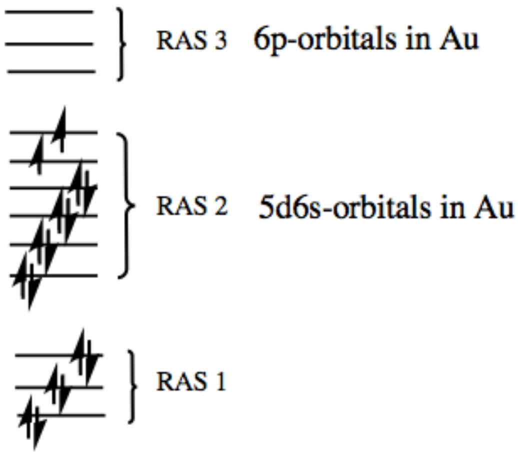

Figure 26: A schematic representation of the orbital classification of Au^{+} in the RAS.

3.4.3.2 Results and Discussion

3.4.2.2.1 Co^{+}•Ar, Co^{+}•Kr, and Co^{+}•Xe

Before proceeding with MREOM-T|T^{+}|SXD calculations, it is necessary to compare the two types of reference states that could be chosen (described in section 3.4.3.1). The results of this comparison for Co^+ are shown in Table 18. Owing to the fact that the SOC calculation was implemented in the ORCA program, the resulting electronic energies can be compared directly with the experimentally determined spin-orbit state energies.

Table 18: The comparison of Co^+•Ar (10 Å) energy levels (eV) for different reference states as calculated by MREOM_T|T^+|SXD in ORCA program.

Configuration	Term	J	NIST	Reference States		
				$3d^74s^1$&$3d^8$	$3d^8$	$3d^74s^1$
$3d^8$	a^3F	4	0.000	0.000	0.292	
		3	0.118	0.113	0.408	
		2	0.198	0.198	0.487	
$3d^74s$	a^5F	5	0.415	0.421		0.388
		4	0.499	0.499		0.466
		3	0.566	0.563		0.530
		2	0.614	0.612		0.578
		1	0.645	0.645		0.611
$3d^74s$	b^3F	4	1.217	1.172		1.146
		3	1.328	1.281		1.250
		2	1.404	1.359		1.328
$3d^8$	a^1D	2	1.445	1.390	1.689	
$3d^8$	a^3P	2	1.644	1.575	1.863	
		1	1.662	1.580	1.869	
		0	1.685	1.610	1.894	
$3d^74s$	a^5P	3	2.203	2.111		2.077
		2	2.236	2.156		2.122
		1	2.274	2.186		2.152
$3d^8$	a^1G	2	2.352	2.463	2.738	

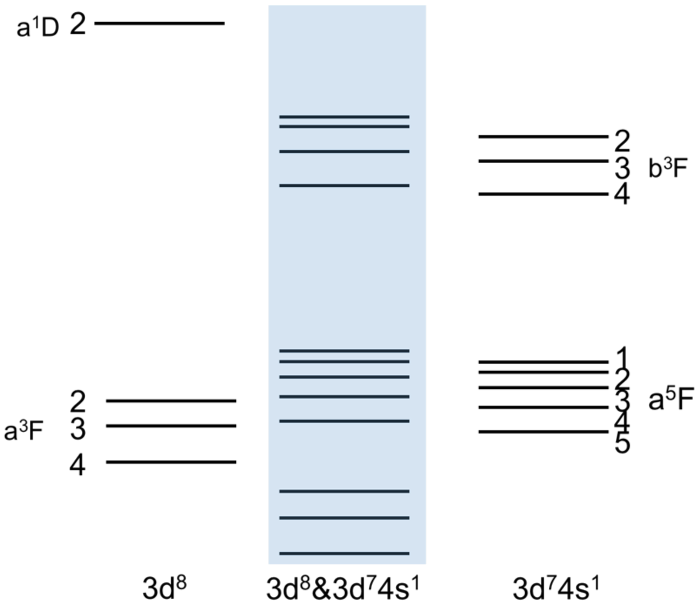

Figure 27: The energy level plot to show the mixing among electronic states from different electronic configurations.

The calculated energies of the electronic states for the separated atom limit of $Co^{+} \cdot Ar$ are quite satisfactory when both the 3d^{7}4s^1 and 3d^8 configurations are included as reference states (see Table 18). Calculations which employ only a single configuration for determining the reference state exhibit energy level spacings that are consistent with the corresponding experimental values, however, the absolute energies between the states are shifted (see Table 18 and Figure 27). This suggests that there are significant interactions between the electronic states arising from the different electronic configurations. In other words, the 3d^{7}4s^1 and 3d^8 electronic configurations should be treated simultaneously when determining reference states. Inclusion of additional electronic configurations is probably not necessary because the first high-lying electronic configuration above the 3d^{7}4s^1, the 3d^{7}4p^1 configuration, is approximately 6 eV above the ground state and is unlikely to mix significantly with the low-energy states.[9]. It should also be noted that the strength of this inter-configurational interaction may vary with the interatomic distance, which means that the shape of the PECs obtained in the previous section may not be accurate. Despite the discrepancy in the inter-configurational electronic energy, the energy differences between spin-orbit states arising from the same electronic configuration compare very well with those determined experimentally. This indicates that the SOC calculation is independent of the choice of reference state.

Besides the choice of reference states for this cobalt system, the choice of the calculation method (*mreom* versus *mreom_ph*) was also explored. The resulting electronic energies of Co^+ are given in Table 19 along with the experimentally determined values.[49] In comparing the results from the *mreom* and *mreom_ph* calculations of Co^+, it is obvious that the *mreom* results agree better with the experimental values. Given this result, and considering the fact that the *mreom_ph* calculation took much longer to converge than did the *mreom* calculation, the *mreom* method was selected for further studies. It is also interesting to note that both the *mreom* and *mreom_ph* calculations are more accurate for the states of the $3d^8$ configurations than those of the $3d^7 4s$ configurations, which might be due to the higher active space percentage (%Active), which is the ratio of CAS wavefunction in the final wavefunction, for the $3d^7 4s$ configurations than the $3d^8$ configurations.

Table 19: Co$^+$ energy-level comparison for *mreom* and *mreom_ph* calculations using Def2-TZVPPD basis set in the ORCA program.

Config.	Term	J	E_{NIST}(eV)	mreom		mreom_ph		Diff[a]	%Diff[a]
				$E_{relative}$	%Active	$E_{relative}$	%Active		
3d^8	a^{3}F	4	0.000	-0.006	0.927	0.069	0.925	-0.075	N/A
		3	0.118	0.107		0.182		-0.075	9.32
		2	0.198	0.191		0.260		-0.069	3.54
3d^{7}4s	a^{5}F[*b*]	5	0.415	0.415	0.995	0.415	0.992	0.000	0.00
		4	0.499	0.493		0.497		-0.004	1.20
		3	0.566	0.556		0.561		-0.005	1.77
		2	0.614	0.605		0.609		-0.004	1.47
		1	0.645	0.639		0.640		-0.001	0.93
3d^{7}4s	b^{3}F	4	1.217	1.166	0.993	1.167	0.990	-0.001	4.19
		3	1.328	1.275		1.276		-0.001	3.99
		2	1.404	1.353		1.351		0.002	3.63
3d^8	a^{1}D	2	1.445	1.384	0.926	1.449	0.922	-0.065	4.22
3d^8	a^{3}P	2	1.644	1.569	0.912	1.626	0.909	-0.057	4.56
		1	1.662	1.574		1.629		-0.055	5.29
		0	1.685	1.602		1.657		-0.055	4.93
3d^{7}4s	a^{5}P	3	2.203	2.104	0.986	2.159	0.983	-0.055	4.49
		2	2.236	2.150		2.190		-0.04	3.85
		1	2.274	2.179		2.228		-0.049	4.18
3d^8	a^{1}G	4	2.352	2.459	0.920	2.470	0.917	-0.011	4.55

a: Diff stands for the energy difference between the *mreom* and *mreom_ph* calculations, and the %Diff is the percentage difference for the different energy of the *mreom* calculations compared with the experimental value.

b: Because of the high active space percentage (0.995), the energy of this state is set the same as experimental energies.

Having selected the *mreom* method and the combined 3d^8 and 3d^{7}4s^1 reference states, the electronic structure of $Co^+ \bullet RG(Ar, Kr, Xe)$ was studied with the MREOM-T|SXD/Def2-

TZVPPD approach. The resulting PECs for Co$^+$•Ar, Co$^+$•Kr and Co$^+$•Xe are plotted in Figures 28, 29 and 30, respectively.

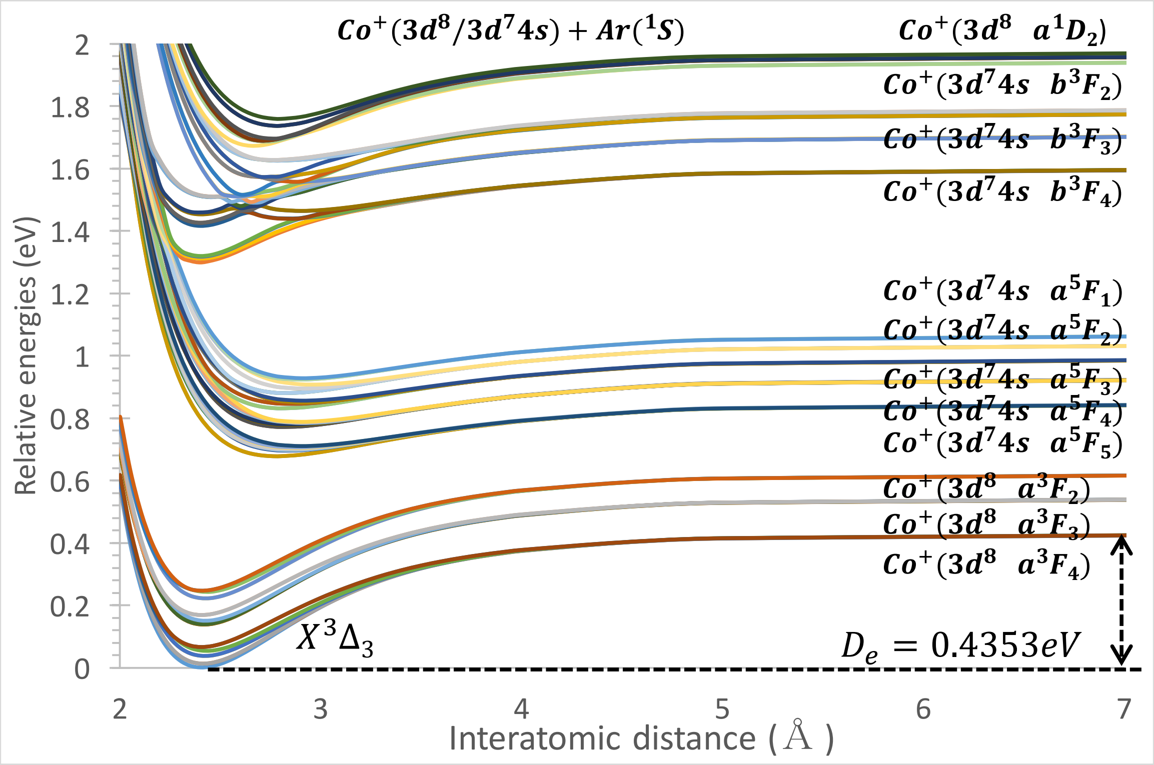

Figure 28: The potential energy curves of $Co^+ \bullet Ar$ as calculated by MREOM-T|T$^+$|SXD/Def2-TZVPPD using the ORCA program.

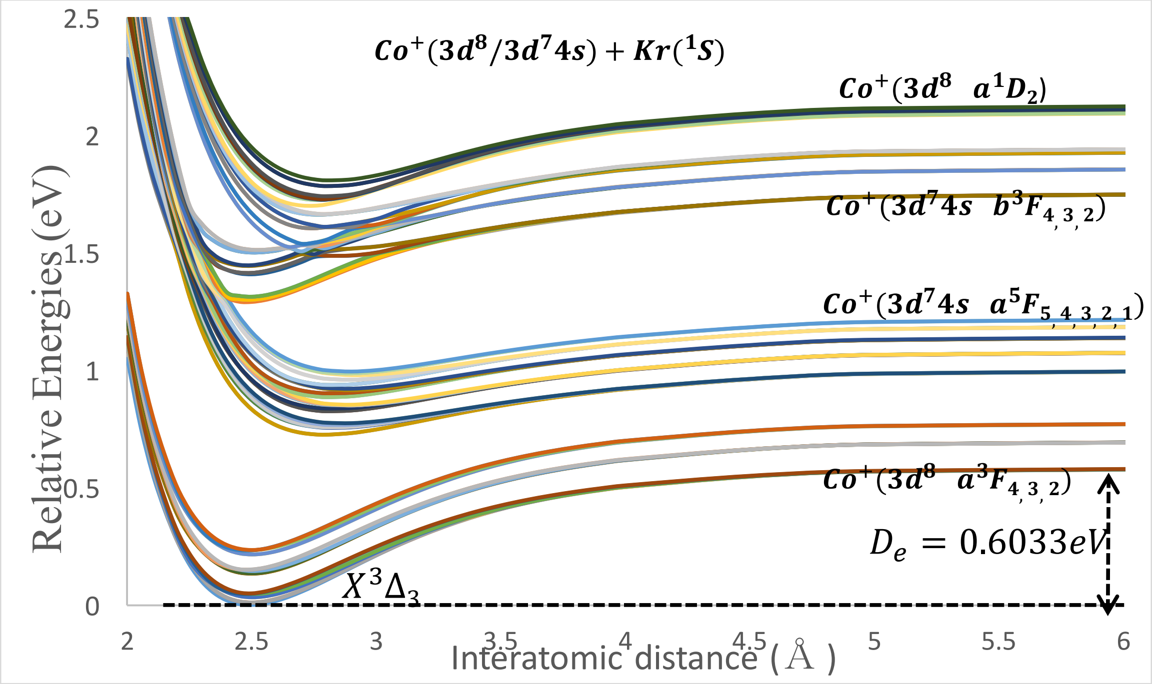

Figure 29: The potential energy curves of $Co^+ \bullet Kr$ as calculated by MREOM-T|T$^+$|SXD/Def2-TZVPPD using the ORCA program.

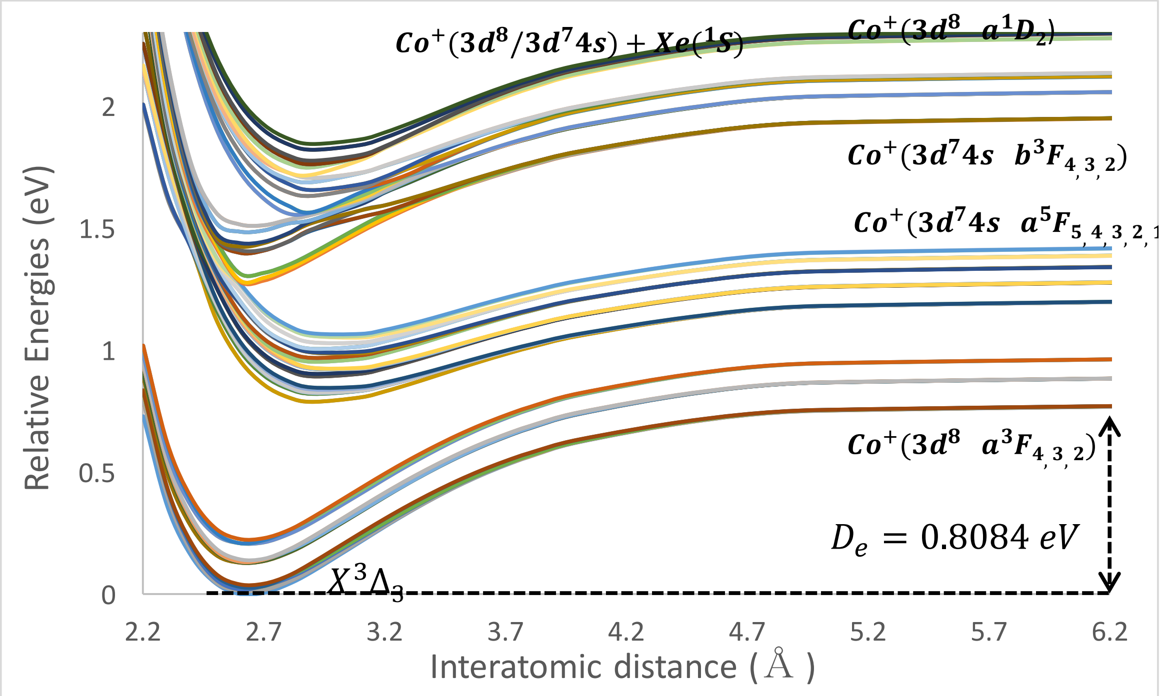

Figure 30: The potential energy curves of $Co^+ \bullet Xe$ as calculated by MREOM-T|T$^+$|SXD/Def2-TZVPPD using the ORCA program.

In Figures 28, 29 and 30, the minima of the ground state potential energy curves have been set zero. Because of the complexity brought by the SOC, it is difficult to assign term symbols to the individual PECs at this point. The dissociation energies, D_e, of $Co^+ \bullet RG(RG = Ar, Kr, Xe)$, which were calculated by subtracting the molecular energy at R_e from the energy at a large separation (10 Å), are given in Table 20. These same PECs, following correction for BSSE, are plotted in Figures 31 and 32 for Co^+•Ar and Co^+•Kr, respectively. One thing to note here is that the counterpoise correction for the Co^+•Xe has error termination and, as yet, we have not solved this problem. The zoom-in PECs of Co^+•Ar can be found in Appendix 5.

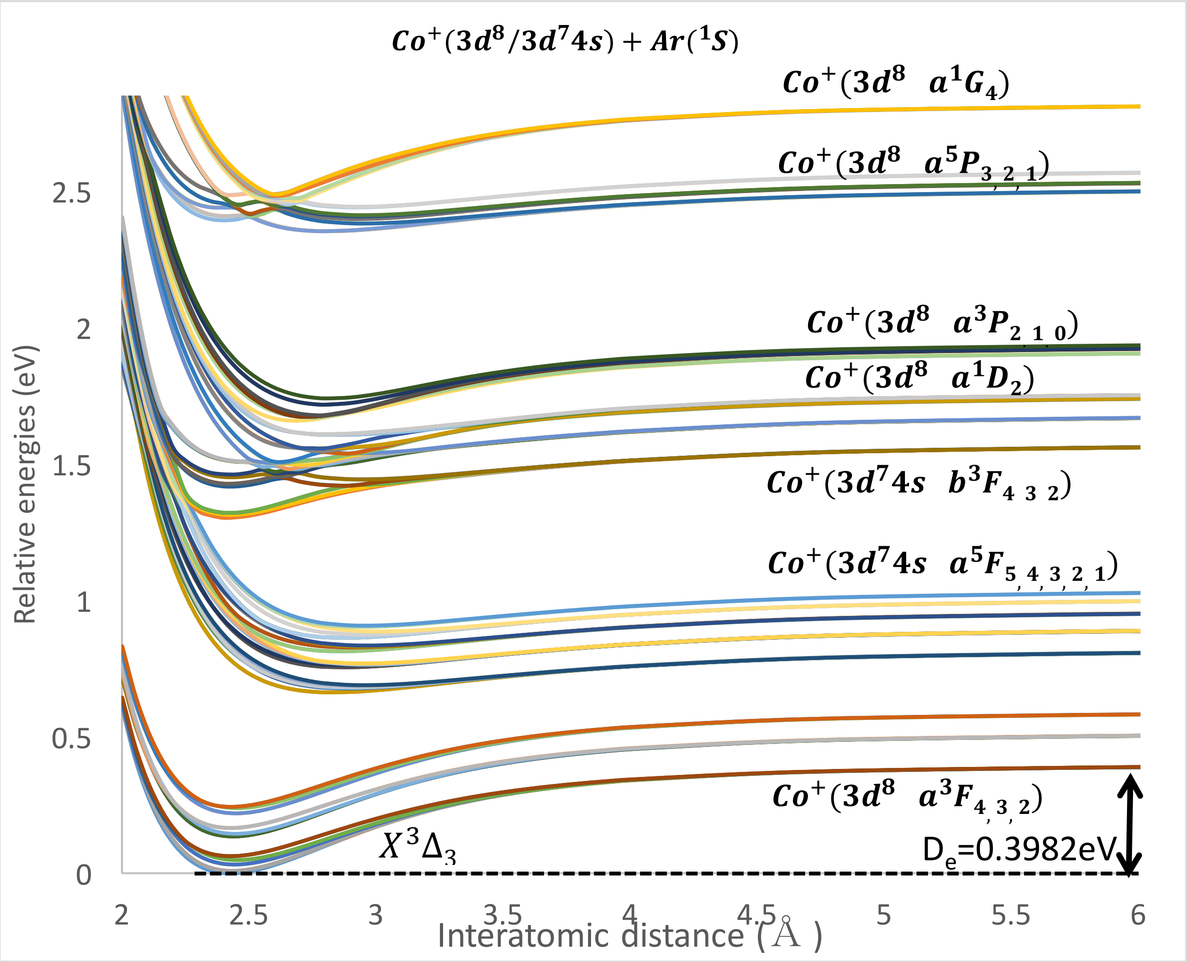

Figure 31: The potential energy curves of $Co^+ \bullet Ar$ as calculated by MREOM-T|T$^+$|SXD/Def2-TZVPPD (including counterpoise correction) using the ORCA program.

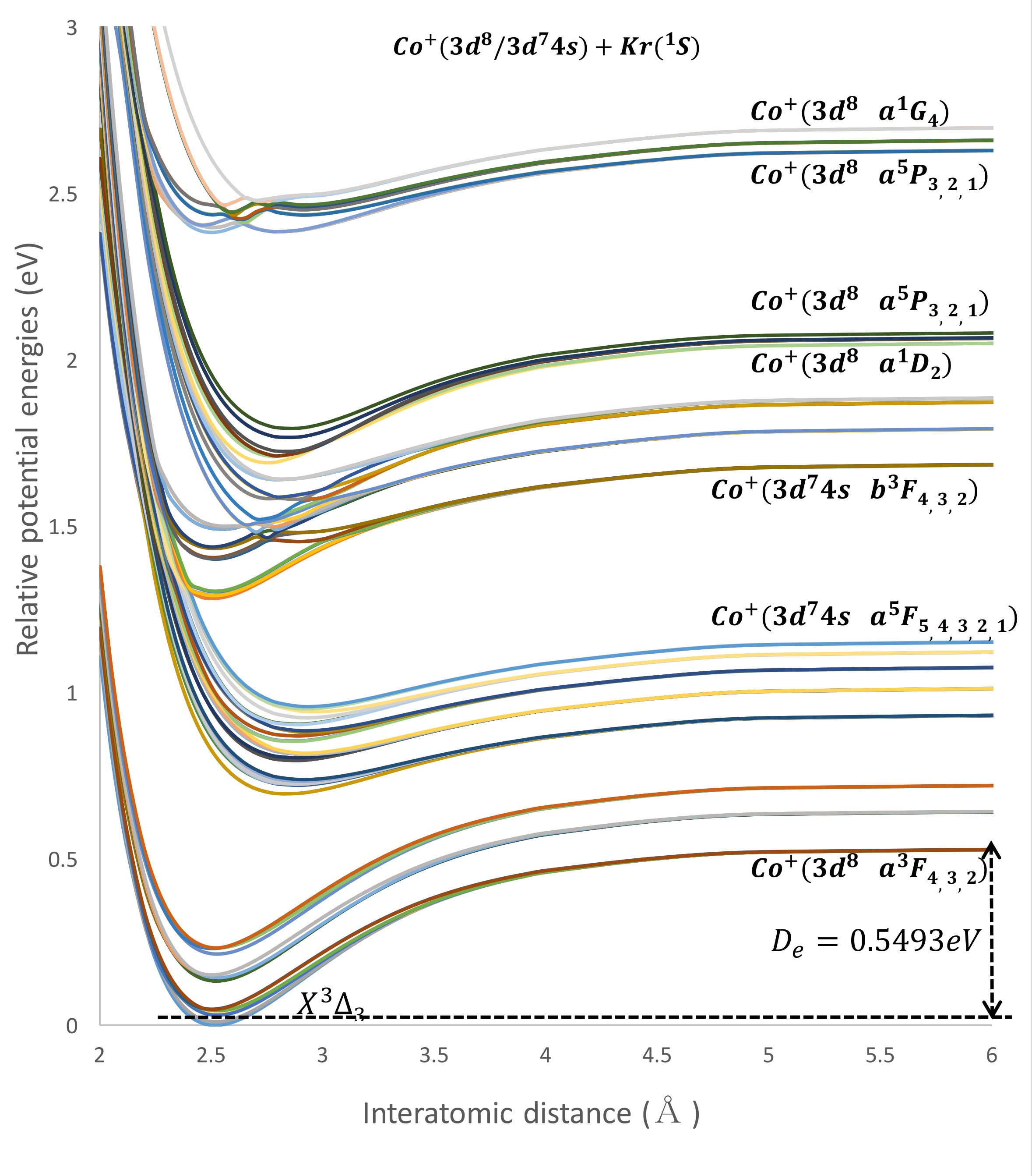

Figure 32: The potential energy curves of $Co^+ \bullet Kr$ as calculated by MREOM-T|T$^+$|SXD/Def2-TZVPPD (including counterpoise correction) using the ORCA program.

Table 20: The equilibrium bond lengths and dissociation energies of $Co^{+} \bullet RG$ $(RG = Ar, Kr, Xe)$ as calculated by MREOM-T|T^{+}|SXD/Def2-TZVPPD using the ORCA program.[7]

Cobalt-complexes	$\boldsymbol{R_{e,calc}}$(Å)	$\boldsymbol{R_{e,exp}}$(Å)[8]	**%diff**	$\boldsymbol{D_{e,calc}(eV)}$	$\boldsymbol{D_{e,exp}(eV)}$	**Diff**	**%diff**
$\boldsymbol{Co^{+} \cdot Ar}$	2.402	2.385	0.71	a^3F_4: 0.4353	0.5097	0.0744	14.59
				a^3F_3: 0.5381		0.0284	5.57
$\boldsymbol{Co^{+} \cdot Kr}$	2.473	2.447	1.06	a^3F_4: 0.6033	0.6701	0.0668	9.97
				a^3F_3: 0.7177		0.0476	7.10
$\boldsymbol{Co^{+} \cdot Xe}$	2.612	-		a^3F_4: 0.8084	0.9547 ± 0.0186	0.1463	15.32
				a^3F_3: 0.9225		0.0322	3.37
$\boldsymbol{Co^{+} \cdot Ar - BSSE}$	2.434	2.385	2.05	a^3F_4: 0.3975	0.5097	0.1122	22.01
				a^3F_3: 0.5118		0.0021	0.41
$\boldsymbol{Co^{+} \cdot Kr - BSSE}$	2.521	2.447	3.02	a^3F_4: 0.5541	0.6701	0.1160	17.31
				a^3F_3: 0.6685		0.0016	0.24

As can be seen in Table 20, the percentage difference in the $Co^{+} \bullet RG$ $(RG = Ar, Kr)$ equilibrium bond length between the calculation and experiment are 0.63% and 2.16%, respectively. This is a remarkably good agreement. For the comparison of the dissociation energies, there are two possible situations. In their paper, Brucat *et al.* concluded that $Co^{+}(3d^8\ \ a^3F_3) + RG(^1S)$ are the ground state products which are formed.[55] If this is the case, our calculation results agree exceptionally well with experimental measurements (*i.e.*, 0.41 % and 0.24 % difference for Co^{+}•Ar and Co^{+}•Kr, respectively). However, the ground electronic state of Co^+ is a^3F_4. If Brucat's article has a typographical error (*i.e.*, the wrong state label), then a relatively large difference exists between our calculations and Brucat's measurements (*i.e.*, 22.01 % and 17.31 % difference for Co^+•Ar and Co^+•Kr, respectively).

3.4.3.2.2 Ag^+•Ar

To assess the performance of the MREOM-T|T^+|SXD/Def2-TZVPPD approach in calculations of $Ag^+ \bullet Ar$, an essentially closed-shell species (the first open-shell configuration is ca. 4.9 eV above the ground state configuration), the electronic energies at an interatomic distance of 10 Å were compared with the experimentally measured internal energies of Ag^+.[9] The results of these calculations are given in Table 21. As can be seen, the calculated relative potential energies of the dissociation thresholds of $Ag^+ \bullet Ar$ (at r = 10 Å) are in good agreement with the literature values of Ag^+ given in the NIST database. This indicates that the selected CAS (described in section 3.3.3) works well in this system. Having identified a suitable CAS, MREOM-T|T^+|SXD/Def2-TZVPPD calculations were carried out for a range of interatomic distances to construct the low-energy PECs of $Ag^+ \bullet Ar$. The low-lying PECs of $Ag^+ \bullet Ar$ are plotted in Figure 33. It is important to note that BSSE is, again, expected to be significant for the $Ag^+ \bullet Ar$ system. It was therefore included in the calculations of the PECs for $Ag^+ \bullet Ar$.

Table 21: The comparison of Ag^{+}•Ar (10 Å) energy levels(eV) between experimental values with the MREOM-T|T^{+}|SXD calculation in ORCA program. The %Diff represents the percent differences between calculation results and experimental energies.

Configuration	Term	J	E_{NIST}	$E_{calc}(Ag^{+} \cdot Ar)$	%Diff
$4d^{10}$	^{1}S	0	0	0	0
$4d^{9}(^{2}D_{5/2})5s$	$^{2}[^{5}/_{2}]$	3	4.856	4.806	1.04
		2	5.052	4.995	1.11
$4d^{9}(^{2}D_{3/2})5s$	$^{2}[^{3}/_{2}]$	1	5.423	5.358	1.20
		2	5.709	5.640	1.22

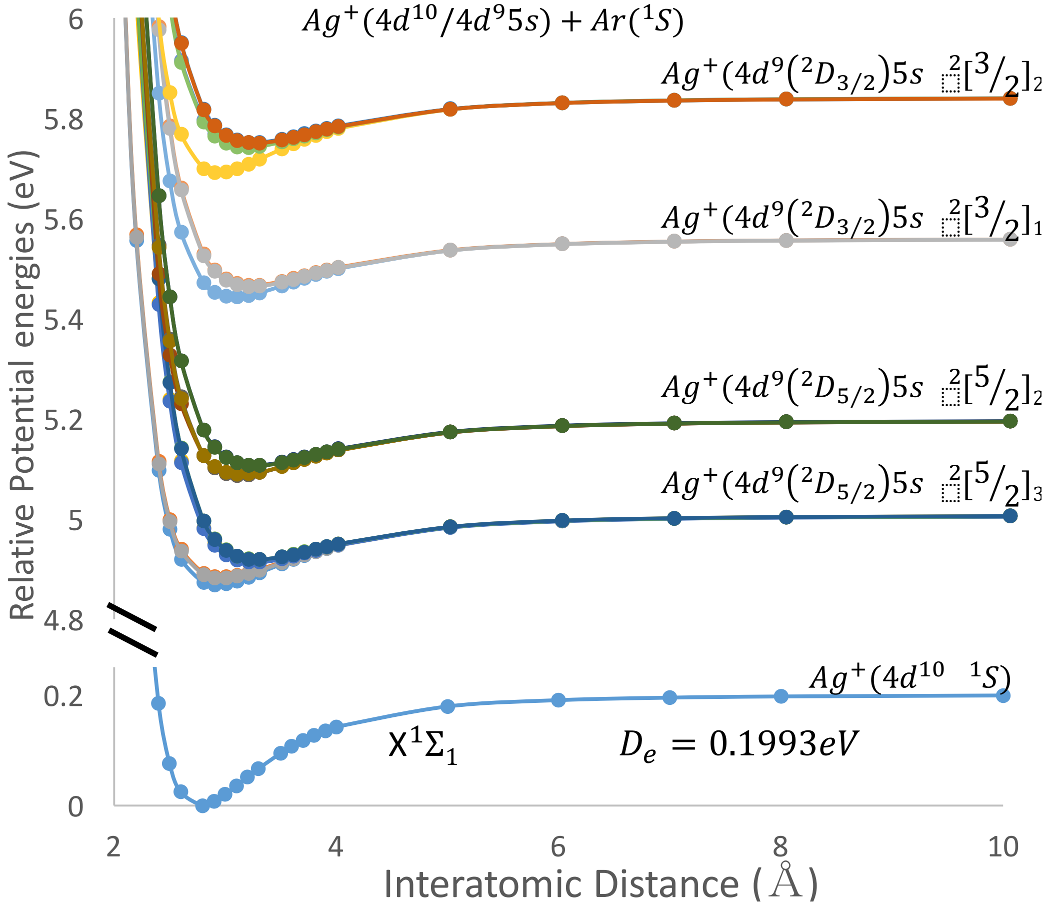

Figure 33: The low-energy potential energy curves of $Ag^{+} \bullet Ar$ as calculated by MREOM-T|T^{+}|SXD/Def2-TZVPPD with counterpoise correction using the ORCA program.

The dissociation energies, D_e, of $Ag^+ \bullet Ar$ were calculated by subtracting the molecular energy at equilibrium bond length, R_e, from the energy at an internuclear separation of 10 Å.[49] The result of this calculation is compared with the results of two single reference CCSD(T) studies in Table 22. Currently, there is no experimental dissociation energy available for $Ag^+ \bullet Ar$. Instead, Gardner *et. al.*[56] investigated neutral $Ag \bullet Ar$ cluster with the RCCSD(T)/d-awCV∝Z calculation and determined an equilibrium bond length of 4.039 Å and a dissociation energy of 0.0133 eV. He also concluded that the HOMO of the $Ag \bullet Ar$ molecule is a sigma antibonding orbital. Thus by removing an electron from this neutral system to form a cation, one would expect stronger binding energy and shorter equilibrium bond length in the cationic system, which agrees with the findings of this work.

Table 22: The equilibrium bond length and the dissociation energy of $Ag^+ \cdot Ar$ comparison among different theoretical calculations. Reference 57 stands for the CCSD(T)/aug-cc-pV5Z calculation with counterpoise correction via Molpro program, Reference 58 corresponds the CCSD(T)/aug-cc-pVQZ-pp calculation in Molpro program.

	R*e* (Å)	D*e* (eV)
This Study	2.70	0.2522
This Study-BSSE correction	2.76	0.1993
Reference 57[57]	2.63	0.3334
Reference 58[58]	2.64	0.3232
Classic Electrostatic	2.76	0.3089

As can be seen in Table 22, the dissociation threshold of $Ag^+ \cdot Ar$ calculated from multireference method is lower than that from the single reference approaches. This lower dissociation energy indicates that the contribution from the excited states to the ground state of the $Ag^{+} \cdot Ar$ system should not be neglected.

3.4.3.2.3 Au^{+}•Ar

The calculations of Au^{+}•Ar introduced two additional complexities compared to those of Ag^{+}•Ar. Firstly, as mentioned in section 3.3.3, RASSCF calculations were required for $Au^{+} \bullet Ar$ to save computational cost. Secondly, the first excited electronic configuration of Au^{+} is only ~1.9 eV above the ground state (in comparison to ~4.9 eV for Ag^{+}). Consequently, the likelihood of interactions between the ground and first excited electronic configurations is much greater in Au^{+}•Ar. It is therefore of interest to study Au^{+}•Ar with MREOM-T|SXD/ Def2-TZVPPD to see if this method would perform as well here as it did with Ag^{+}•Ar. Table 23 provides a comparison between the electronic states of $Au^{+} \bullet Ar$ at r = 10 Å to the experimentally measured internal energies of Au^{+}.[9] The low-energy PECs of Au^{+}•Ar are plotted in Figure 34. The calculated ground state equilibrium bond length and dissociation energy are compared with literature values in Table 24.

Table 23. The comparison of Ag^{+}•Ar (10 Å) energy levels(eV) between experimental values with the MREOM-T|T^{+}|SXD calculation in ORCA program. E$_{\text{NIST}}$ gives the experimentally measured internal energies of Au^{+} as tabulated by the NIST database.[9] The %Diff gives the percent differences between calculation results and experimental energies.

Configuration	Term	J	E$_{\text{NIST}}$	E$_{\text{calc}}$(Au^{+} · Ar)	%diff
$5d^{10}$	^{1}S	0	0	0	0
$5d^{9}6s$	^{3}D	3	1.865	1.828	1.99
		2	2.187	2.147	1.85

		1	3.443	3.502	1.72
$5d^9 6s$	^1D	2	3.673	3.710	1.03
$5d^8 6s^2$	^3F	4	5.019	4.846	3.44
		3	6.469	6.405	0.99
		2	6.014	5.858	2.60

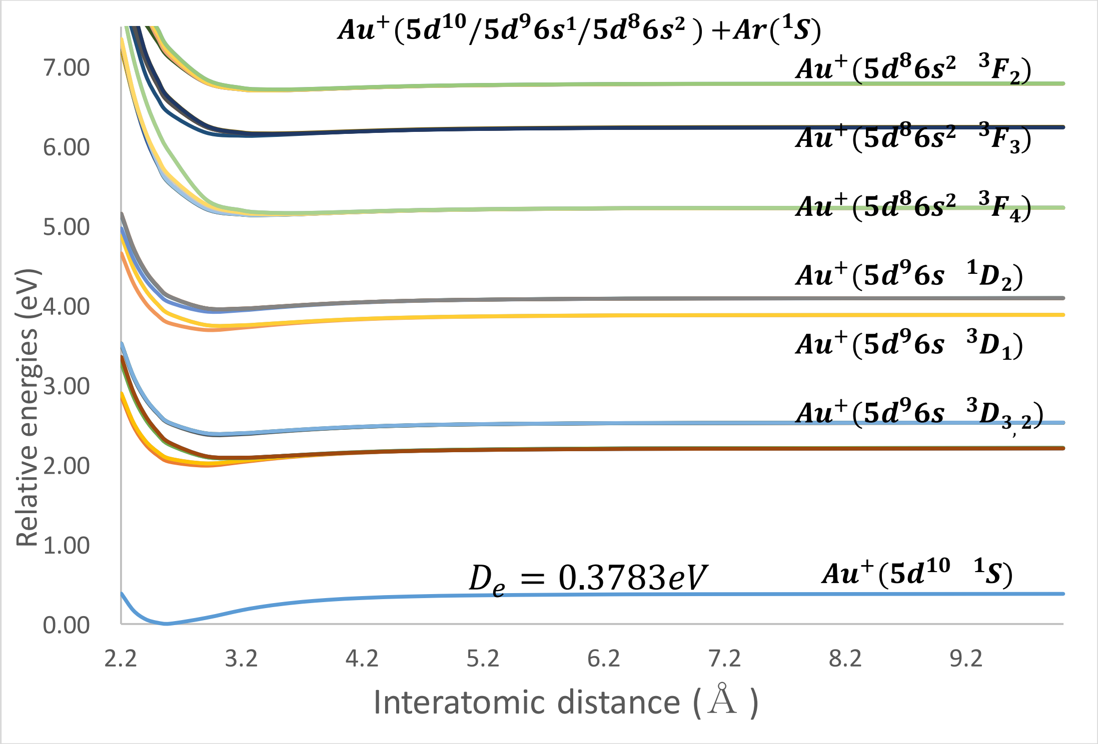

Figure 34: The potential energy curves of $Au^+ \bullet Ar$ as calculated by MREOM-T|SXD/Def2-TZVPPD with counterpoise correction using the ORCA program.

Table 24. The equilibrium bond length and the dissociation energy of $Au^{+} \cdot Ar$ comparison among different theoretical calculations. Reference 57 stands for the CCSD(T)/aug-cc-pV5Z calculation with counterpoise correction via Molpro program, and Reference 58 corresponds to the CCSD(T)/aug-cc-pVQZ-pp calculation in Molpro program.

	Re(Å)	De(eV)
This Study	2.53	0.4192
This Study-BSSE correction	2.56	0.3783
Reference 53[57]	2.52	0.4886
Reference 54[58]	2.53	0.4643

Similar to the $Ag^{+} \cdot Ar$ system, the dissociation threshold of $Au^{+} \cdot Ar$ calculated by multireference method is lower that from the single reference approach. From both the $Ag^{+} \cdot Ar$ and the $Au^{+} \cdot Ar$ cases, we can conclude that the employment of multireference approach is necessary even for close-shell transition metal-containing systems.

3.4.4 Ro-vibrational Fits

3.4.4.1 Computational Details

The ro-vibrational energy levels of the ground electronic state and the first 19 excited electronic states of $Co^{+} \bullet Ar$ were investigated with the LEVEL 8.2 program.[59] The selection of these excited states is based on the spectral range that has been studied experimentally.[8] Depending on the depth of the potential well, up to 50 vibrational levels are considered for each selected electronic state. Further to this, we have calculated for, each vibrational level 100 associated rotational levels (Figure 35). Based on these ro-vibronic energy levels, the rotational and vibrational constants for each electronic state are calculated with a six-order polynomial fit based on Equations 76 and 77.

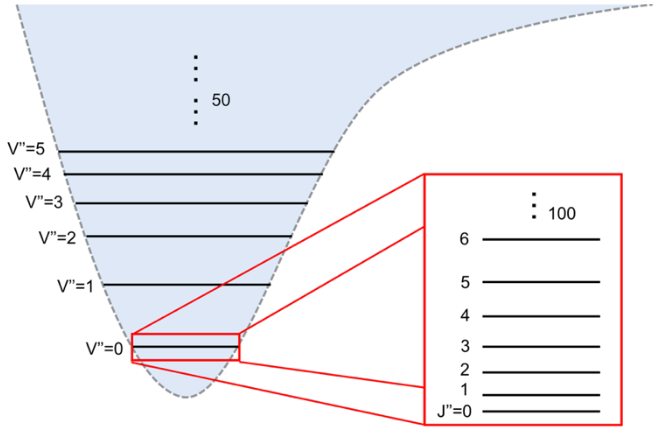

Figure 35. The ro-vibronic energy levels built on the ground state PEC

Upon calculating the ro-vibrational levels of a single PEC, the ro-vibronic transitions between the nineteen excited PECs and the ground vibronic state can be calculated using the LEVEL program (*i.e.*, see Figure 36). The intensity of the transition is estimated with the Franck-Condon factor associated with the individual transitions, and the relative Boltzmann population of the lowest 10 rotational levels of the ground state at 298.15 K.

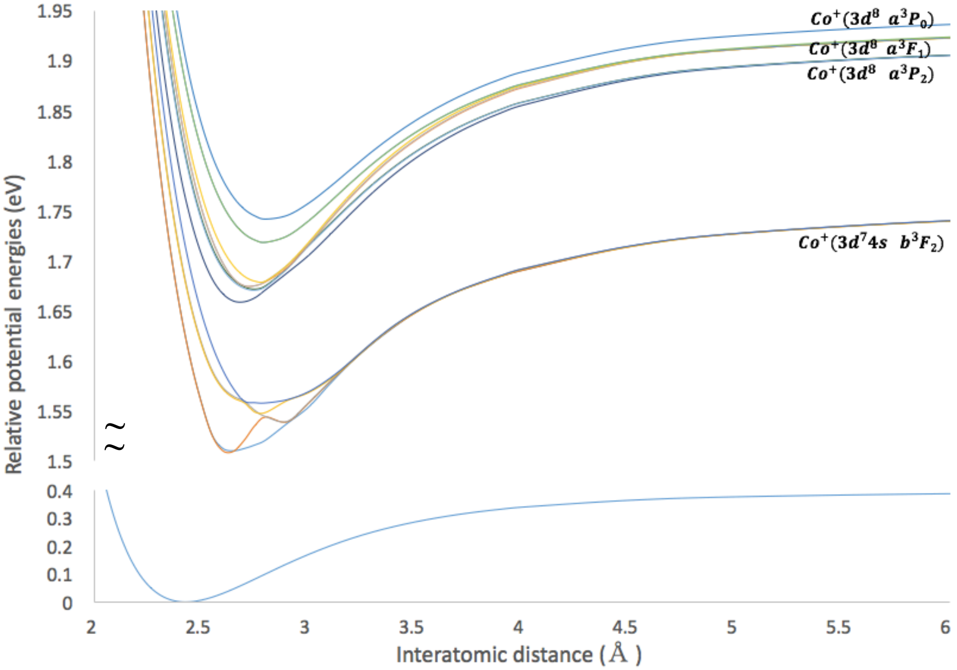

Figure 36. The PECs of $Co^{+\bullet}Ar$ ground state and the first nineteen excited states as calculated by MREOM-T|SXD/Def2-TZVPPD using the ORCA program.

3.4.4.2 Results and Discussions

To extract molecular parameters and spectra for Co$^+$•Ar, the ro-vibrational energy level structure of $Co^+ \cdot Ar$ was mapped using the LEVEL program.[45] The results of this analysis were then compared with the vibrational constants and dissociation energy reported in the experimental study by Brucat *et al*. such that we could assess the accuracy of the calculated PECs.[55] The calculated zero-point-energy (ZPE) of Co$^+$•Ar is 0.01029 eV, which, when combined with the calculated value of D_e = 0.3975 eV, yields D_0 = 0.3872 eV. Thus, the calculated value of D_0 is 0.1225 eV less than the experimentally determined value of 0.5097 eV, which is a difference of ~24 %. Of course, there is some ambiguity as to the experimentally determined value of D_0 (*vide supra*). A further comparison between calculated and measured molecular parameters for Co$^+$•Ar is provided in Table 25, which gives the vibrational parameters that were extracted for the three excited states analyzed in Brucat's experimental study. These were determined via analysis of the $X^3\Delta_3(v = 0)$ →A, $X^3\Delta_3(v = 0)$ →B, and $X^3\Delta_3(v = 0)$ →C vibronic band systems. [8]

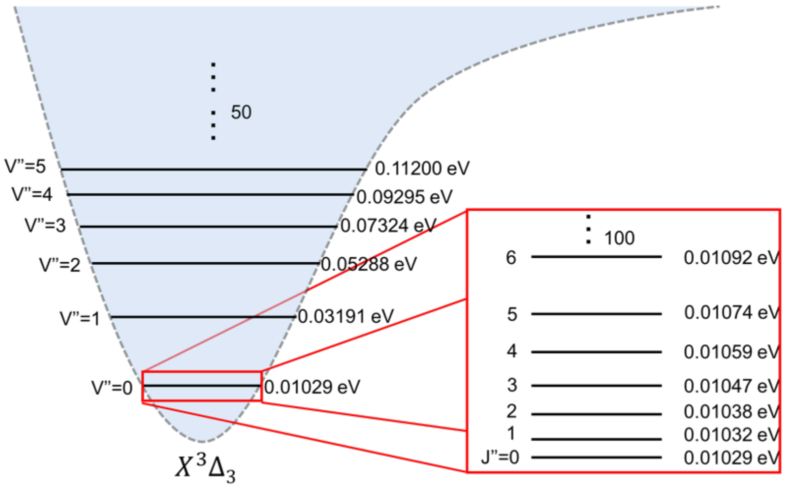

Figure 37. Low-lying ro-vibrational levels of the Co$^{+\bullet}$Ar ground state as calculated using the LEVEL program.[45]

Table 25. The calculated ro-vibrational constants and the relative energies for 20 electronic spin states of Co^+•Ar as determined by a LEVEL program fit of the MREOM-T|T^+|SXD/Def2-TZVPPD PECs. Experimentally determined parameters are those reported in reference 8. The Relative Energy stands for the threshold energy relative to the minimum energy of ground state.

	Vibrational Constant (cm^{-1})		Rotational Constant (cm^{-1})		Relative Energy (eV)
	ω_e	$\omega_e x_e$	B_J	D_J	
Experimental[55]					
A (a^1D_2)	164	3.13	0.1172	N/A	1.954
B (b^3F_2)	120	2.18	0.0625	N/A	1.913
C (a^3P_2)	175	3.29	0.0939	N/A	2.153
Theoretical					
G.S.	179.93	2.688	0.1194	2E-7	0.397
b^3F_2	130.58	0.513	0.0986	2E-7	1.7478
	133.73	1.461	0.1018	1E-7	1.7481
	122.32	1.556	0.0867	1E-7	1.7481
	97.423	1.8524	0.0911	2E-7	1.7482
	101.26	1.461	0.0895	3E-7	1.7482
a^1D_2	164.07	5.2322	0.0924	1E-7	1.7605
	71.257	0.3994	0.0863	5E-7	1.7606
	72.266	1.178	0.0863	5E-7	1.7606
	85.712	1.725	0.0885	4E-7	1.7609
	84.073	1.3628	0.0884	4E-7	1.7609
a^3P_2	151.66	7.2055	0.0977	2E-7	1.930
	153.5	5.0167	0.0939	2E-7	1.930
	153.04	4.9579	0.0941	2E-7	1.931
	150.23	3.184	0.0940	2E-7	1.931
	151.53	3.5256	0.0943	2E-7	1.932
a^3P_1	154.03	3.873	0.0922	1E-7	1.9130
	130.14	2.9269	0.0897	2E-7	1.9130

	128.65	2.4564	0.0897	2E-7	1.9131
a^3P_0	123.97	2.880	0.0886	2E-7	1.944

However, the relative peak intensities of theoretical spectrum still deviate significantly from Brucat's work.[8] Further efforts are required to resolve this issue.

3.5 Conclusion

The PECs of Co$^{+\bullet}$Ar that were calculated at the MRCI+Q/Def2-TZVPPD level of theory exhibited unexpected discontinuities, which may be partially due to an discontinuous PECs from CASSCF calculation. It is clear that the Davidson correction cannot completely account for the size-inconsistency error across the range of interatomic distances that were studied. To remedy this size-consistency issue, the PECs of Co^{+}•Ar, Co^{+}•Kr, Ag^{+}•Ar, and Au^{+}•Ar were constructed from MREOM-T|T^{+}|SXD/Def2-TZVPPD calculations, which included corrections for the SOC effect and BSSE. The dissociation energies (D_e) of Co^{+}•Ar, Co^{+}•Kr, Ag^{+}•Ar, and Au^{+}•Ar obtained from these calculations are 0.3975 eV, 0.5541 eV, 0.1993 eV, and 0.3783 eV, respectively. After the ZPE correction, the dissociation energies (D_0) of Co^{+}•Ar, Co^{+}•Kr, Ag^{+}•Ar, and Au^{+}•Ar obtained from these calculations are 0.3872 eV, 0.5443 eV, 0.1931 eV, and 0.3696 eV, respectively. The calculated D_0 values of Co^{+}•Ar and Co^{+}•Kr were somewhat smaller than the experimentally determined D_0 values of 0.5097 eV and 0.6701 eV, respectively. Whether this error is caused by selection of too small a basis set for calculations, or a poor assignment of the experimental data is not clear. We are currently working towards adding more orbitals (i.e., 3p or more orbitals in Co^{+}•Ar system) to the CAS and using the larger basis sets (*i.e.*, Def2-QZVPPD) to explore whether the error is computational in nature. Other members of the Hopkins group are also working towards carrying out velocity-map image experiment to confirm the experimentally determined dissociation energies.

From the ro-vibrational calculations, the ZPEs of Co^+•Ar, Co^+•Kr, Ag^+•Ar, and Au^+•Ar are: 0.0103 eV, 0.0098 eV, 0.0062 eV, and 0.0087 eV, respectively. Furthermore, transitions between the nineteen excited PECs and the ground vibronic state are calculated and the vibration-rotation line spectrum is plotted. However, only the Franck-Condon factor is considered for the intensity of our ro-vibronic spectrum. Thus, the factor that may affect the intensity of the spectrum, such as the Hönl-London factor and Boltzmann distribution, should be considered and explored in the future.

Chapter 4: Conclusions and Closing Remarks

The electronic structures of the Na^+•Ar, Ag^+•Ar, Au^+•Ar, Co^+•RG (RG = Ar, Kr, Xe), and Co_2^+ systems have been explored computationally in an effort to identify the calculation method that best reproduces experimental data. Preliminary DFT and CCSD calculations for Co_2^+ yield discontinuous PECs as well as negative excitation energies, which reveals that single reference methods are inadequate to describe the electronic structure of the Co_2^+ system. Indeed, this is expected to be the case for any transition-metal-containing open-shell species, and all molecules with high densities of states. Consequently, it is clear from the studies outlined herein that the incorporation of multi-reference methods is absolutely necessary to accurately model the electronic structures of molecules.

Two multireference approaches, MRCI and MREOM-CCSD, have been applied to several cobalt-containing systems. For the MRCI/Def2-TZVPPD treatment of the Co^+•Ar, all of the calculated excitation energies are positive, but discontinuous PECs are still predicted. This unexpected and unphysical behavior may be due to the unsuitable selection of the CAS orbitals. The MREOM-CCSD approach, on the other hand, yields promising results for the Co^+•RG (RG= Ar, Kr), Ag^+•Ar, and Au^+•Ar systems - all calculated excitation energies are positive and the PECs are continuous. The dissociation energies (D_0) of Co^+•Ar, Co^+•Kr, Ag^+•Ar, and Au^+•Ar are 0.3872 eV, 0.5443 eV, 0.1931 eV, and 0.3696 eV, respectively. It was clear that corrections to account for the SOC effect and BSSE were necessary to improve calculation accuracy. Nevertheless, in comparing the results of our calculations with the experimentally determined values of 0.5097 eV and 0.6701 eV for Co^+•Ar and Co^+•Kr respectively, we find a ~0.11 eV underestimation for D_0 for both systems. Whether this is a result of computational accuracy, or a poor assignment of experimental data is currently not clear. An alternative method of assessing calculation accuracy by comparison of predicted excited state parameters with those determined experimentally has also been unfruitful thus far owing to ambiguities introduced by the very high density of excited electronic states in the Co-containing molecules.

In the future, efforts can be made to improve both theoretical calculation and experimental measurement. The accuracy of the MREOM calculation is dependent on the choice of the CAS, the basis set used and the modification of the excitation operators. Thus, adding more orbitals (*i.e.*, 3p or more orbitals in Co^+Ar system) to the CAS, using larger basis sets (*i.e.*, Def2-QZVPPD), or adding the U excitation operator (*i.e.*, MREOM-T|T^+|SXD|U) might improve calculation accuracy. The use of additional excitation operators in multireference calculations is especially attractive since this should also speed up the calculations. On the experimental side, velocity-map imaging experiments could be conducted to verify molecular dissociation energies, and rotationally-resolved spectra could be acquired to provide a more detailed view of the excited electronic states.[60] While, ultimately, this work did not provide the "skeleton key" necessary to unlock the low-energy electronic structure of the high-spin cobalt-containing molecules chosen for study, it has provided an invaluable road map to help guide future studies of multi-reference systems.

Reference

1. Mintz, B., Williams, T. G., Howard, L. & Wilson, A. K. Computation of potential energy surfaces with the multireference correlation consistent composite approach. *J. Chem. Phys.* **130, 23410,** (2009).

2. Wang, T. *et al.* Synchrotron radiation-based multi-analytical approach for studying underglaze color: The microstructure of Chinese Qinghua blue decors (Ming dynasty). *Anal. Chim. Acta* **928,** 20–31 (2016).

3. Julien, C. M., Mauger, A., Zaghib, K. & Groult, H. Comparative Issues of Cathode Materials for Li-Ion Batteries. *Inorganics* **2,** 132–154 (2014).

4. Riedel, T., Walter, S., Claeys, M., Schulz, H. & Schaub, G. Fuels and petrochemicals from CO2 via Fischer-Tropsch synthesis — steady state catalyst activity and selectivity. *Stud. Surf. Sci. Catal.* **114,** 443–446 (1998).

5. Sharma, R. *et al.* Improvement in magnetic behaviour of cobalt doped magnesium zinc nano-ferrites via co-precipitation route. *J. Alloys Compd.* **684,** 569–581 (2016).

6. Russon, L. M. *et al.* The bond energy of Co2+. *Chem. Phys. Lett.* **204,** 235–240 (1993).

7. Hayes, T., Bellert, D., Buthelezi, T. & Brucat, P. . The bond length of CoKr+. *Chem. Phys. Lett.* **242,** 627–631 (1995).

8. Lessen, D. & Brucat, P. J. Resonant photodissociation of CoAr+ and CoKr+: Analysis of vibrational structure. *J. Chem. Phys.* **90,** 6296–6305 (1989).

9. Kramida, A., Ralchenko, Yu., Reader, J. and N. A. T. (2015). NIST Atomic Spectra Database (ver. 5.3), Retrieved from http://physics.nist.gov/asd [2016, June 26]. National Institute of Standards and Technology, Gaithersburg, MD.

10. Jiang, W., Deyonker, N. J. & Wilson, A. K. Multireference Character for 3d Transition-Metal-Containing Molecules. *J. Chem. Theory Comput* **8,** 460–468 (2012).

11. Weymuth, T., Couzijn, E. P. A., Chen, P. & Reiher, M. New benchmark set of transition-metal coordination reactions for the assessment of density functionals. *J. Chem. Theory Comput.* **10,** 3092–3103 (2014).

12. Nakao, Y., Hirao, K. & Taketsugu, T. Theoretical study of the water activation by a cobalt cation: Ab initio multireference theory versus density functional theory. *J. Chem. Phys.* **1141,** (2001).

13. Titov, A. V., Mosyagin, N. S., Alekseyev, A. B. & Buenker, R. J. GRECP/MRD-CI

calculations of spin-orbit splitting in ground state of Tl and of spectroscopic properties of TlH. *Int. J. Quantum Chem.* **81,** 409–421 (2001).

14. Huntington, L. M. J., Demel, O. E. & Nooijen, M. Benchmark Applications of Variations of Multireference Equation of Motion Coupled-Cluster Theory. *J. Chem. Theory Comput.* **12,** 114–132 (2016).

15. Szabo, A. & Ostlund, N. S. *Modern Quantum Chemistry: Introduction to Advanced Electronic Structure Theory, 75*. (McGraw-Hill, 1989).

16. Lowe, J. P. & Peterson, K. A. *Quantum Chemistry, p359*. (Elsevier AP, 2006).

17. Standard, J. M. Chemistry 460: Basis Set Notation. (Illinois State University, 2015).

18. Atkins, P. & Friedman, R. *Molecular Quantum Mechanics, p302*. (Oxford University Press, 2005).

19. Atkins, P. & Friedman, R. *Molecular Quantum Mechanics*. (Oxford, 2011).

20. Helgaker, T. Basis functions and basis sets. (Department of Chemistry, University of Oslo, Norway, 2010).

21. Sherrill, C. D. Counterpoise Correction and Basis Set Superposition Error, 2-4. (School of Chemistry and Biochemistry Georgia Institute of Technology, 2010).

22. Deshmukh, P. C., Banik, A. & Angom, D. Hartee-Fock Self-Consistent Field Method for Many-Electron Systems, 8. (Indian Institute of Technology Madras, Chennai; Space Applications Centre, Ahmadabad; Physical Research Laboratory, Ahamadabad., 2011).

23. Lowe, J. P. & Peterson, K. A. *Quantum Chemistry, p359*. (Elsevier Academic Press, 2006).

24. Cordova, F. *et al.* Troubleshooting time-dependent density-functional theory for photochemical applications: Oxirane. *J. Chem. Phys.* **127,** 164111–134305 (2007).

25. Piela, L. *Ideas of Quantum Chemistry, 218*. (2014). doi:10.1016/B978-0-444-59436-5.00016-7

26. Sherrill, C. D. An Introduction to Configuration Interaction Theory, 31. (Georgia Institute of Technology, 1995).

27. Malmqvist, P.-H. & Roos, B. 0. THE CASSCF STATE INTERACTION METHOD. *Chem. Phys. Lett.* **155,** (1989).

28. Bartlett, R. J. & Musiał, M. Coupled-cluster theory in quantum chemistry. *Rev. Mod.*

Phys. **79,** 291 (2007).

29. Crawford, T. D. & Schaefer, H. F. An Introduction to Coupled Cluster Theory for Computational Chemists, 16. (The University of Georgia, Athens, Georgia 30602-2525).

30. Zhao, Y., Pu, J., Lynch, B. J. & Truhlar, D. G. Tests of second-generation and third-generation density functionals for thermochemical kinetics. *Phys. Chem. Chem. Phys.* **6,** 673–676 (2004).

31. Dahlbeck, R. & Yuan, Y. ESR of Co, Rh, Ir trimers and diatomic ions. **107,** 305–306 (1992).

32. Schultz, N. E., Zhao, Y. & Truhlar, D. G. Databases for Transition Element Bonding: Metal–Metal Bond Energies and Bond Lengths and Their Use to Test Hybrid, Hybrid Meta, and Meta Density Functionals and Generalized Gradient Approximations. *J. Phys. Chem. A* 1–66 (2005).

33. Knowles, P. *et al.* Ab Initio Methods for Electron Correlation in Molecules. *Mod. Methods Algorithms Quantum Chem.* **1,** 69–151 (2000).

34. Raghavachari, K. & Anderson, J. B. Electron Correlation Effects in Molecules. *J. Phys. Chem.* **100,** 12960–12973 (1996).

35. Clifford, D. S., Gernot, F. & Kwang, K. *Theory and Applications of Computational Chemistry: The first Forty Years, 669*. (2005).

36. Aquilante, F. *et al.* MOLCAS 8: New Capabilities for Multiconfigurational Quantum Chemical Calculations across the Periodic Table. *J. Comput. Chem.* **37,** 506–541 (2016).

37. Liu, Z. multireference equation of motion coupled cluster study of atomic excitation sepctra, 22. (Department of Chemistry, University of Waterloo, 2015).

38. Malmqvist, Å. *et al.* The restricted active space followed by second-order perturbation theory method: Theory and application to the study of CuO2 and Cu2O2 systems. *J. Chem. Phys.* **128,** 204109 (2008).

39. Huntington, L. Development of an Automatic Code Generator and Implementation of Multireference Equation of Motion Coupled-Cluster Theory in the ORCA Program Package, 58. (Department of Chemistry, University of Waterloo, 2015).

40. Mueller, M. *Fundamentals of Quantum Chemistry, Molecular Spectroscopy and Modern Electronic Structure Computations, 207*. (Kluwer Academic/Plenum Publishers, 2001).

41. Mueller, M. Fundamentals of Quantum Chemistry. *J. Chem. Inf. Model.* **53,** 208 (1989).

42. Schröder, M. Theoretical Investigation of the Ultrafast Photodissociation Dynamics of Diatomic Molecules in a Rare Gas Environment, Chapter 4 Diatomics in Molecules - DIM, 50. (Whitman College, 1953).

43. Hopkins, W. S. Unit 1 – Spectroscopic Theory Fall 2012. 1–58 (2012).

44. Schwarz, W. H. E. & Schwarz, W. H. E. *Relativistic Methods for Chemists*. *English* **0172, 63,** (2010).

45. Le Roy, R. J. LEVEL: A computer program for solving the radial Schrödinger equation for bound and quasibound levels. *J. Quant. Spectrosc. Radiat. Transf.* 1–12 (2016). doi:10.1016/j.jqsrt.2016.05.028

46. Werner, H.-J. & Knowles, P. J. MOLPRO Users Manual Version 2010.1(University College Cardiff Consultants Limited). (2010).

47. Hellweg, A. & Rappoport, D. Development of new auxiliary basis functions of the Karlsruhe segmented contracted basis sets including diffuse basis functions (def2-SVPD, def2-TZVPPD, and def2-QVPPD) for RI-MP2 and RI-CC calculations. *Phys. Chem.* **17,** 1010–1017 (2015).

48. Schuchardt, K.L., Didier, B.T., Elsethagen, T., Sun, L., Gurumoorthi, V., Chase, J., Li, J., and Windus, T. L. & J. Chem. Inf. Model., 47(3), 1045-1052, 2007, doi:10. 1021/ci600510j. Basis Set Exchange: A Community Database for Computational Sciences.

49. Liang, G., Liu, X., Zhang, X., Xu, H. & Yan, B. Accurate potential energy functions, non-adiabatic and spin–orbit couplings in the ZnH+ system. *Spectrochim. Acta Part A Mol. Biomol. Spectrosc.* **156,** 9–14 (2016).

50. Szczesniak, M. M., Scheiner, S., Szcz~ Niak, M. M. & Scheinerb, S. Møller-Plesset Treatment of Electron Correlation in (HOHOH)- Meller -Plesset treatment of electron correlation effects in (HOHOHt. *Chem. Phys* **77,** (1982).

51. Kumar, D. & Parshad, D. Study of Intermolecular Forces and Interactions in Binary Liquid Mixture Chloroform , Acetone , M-xylene, and Cyclohexane in DMSO. *Indian Streams Res. J.* **4,** 1–8 (2014).

52. Partridge, H., Baugleicher, C. W., Jr. & Langhoff Stephen R. Theoretical Study of MetalIons Bound to He, Ne, and Ar. *J. Phys. Chem.* **96,** 5350 (1992).

53. Burns, K. ~L., Bellert, D., Leung, A. ~W.-K. & Breckenridge, W. ~H. The effects of

dispersive Cn/Rn-attraction on M+/Rg bonding (M+=atomic metal ion, Rg=rare gas atom). *J.Chem.Phys.* **114,** 2996–3002 (2001).

54. Miller, T. M. in *CRC Handbook of Chemistry and Physics* 10–188 (2016).
55. Asher, R. L., Bellert, D., Buthelezi, T. & P.J.Brucat. The ground state of CoAr+. *Chem. Phys. Lett.* **227,** 277–282 (1994).
56. Gardner, A. M., Plowright, R. J., Watkins, M. J., Wright, T. G. & Breckenridge, W. H. Theoretical study of the X Σ 2 + states of the neutral CM–RG complexes (CM = coinage metal, Cu, Ag, and Au and RG = rare gas, He–Rn). *J. Chem. Phys.* **132,** 184301–5562 (2010).
57. Tong, X.-F., Yang, C.-L., Wang, M.-S., Ma, X.-G. & Wang, D.-H. Interactions of Mz–X complexes (M = Cu, Ag, and Au; X = He, Ne, and Ar; and z = ±1). *J. Chem. Phys.* **134,** 024306 (2011).
58. Yousef, A. *et al.* Interaction potentials and transport properties of coinage metal cations in rare gases. *J. Chem. Phys.* **127,** 154309 (2007).
59. Roy, R. J. Le. *LEVEL 8.2 A Computer Program for Solving the Radial Schrodinger Equation for Bound and Quasibound Levels, 2*. (Guelph-Waterloo Centre for Graduate Work in Chemistry, 2014).
60. Dick, B. Inverting ion images without Abel inversion: maximum entropy reconstruction of velocity maps. *Phys. Chem. Chem. Phys.* **16,** 570–580 (2014).

Appendixes

Appendix 1: The sample input file of MRCI/Def2-TZVPPD calculation on electronic states of $Co^{+}(d^{8})\cdot Ar$ at a 10Å interatomic distance via Molpro program

***,Co cation with Ar: d8 Configuration	Title
geometry={Co; Ar, Co, r(i)}	Z-Matrices of $Co^{+}Ar$
sym=[1,2,3,4,5,6,7,8,9,10,11,12,13,14,15]	15 states (a^{3}F, a^{1}D, a^{3}P)
SET,DKROLL=1 SET,DKHO=5	DKH relativistic effect
basis={copied from EMSL}	Basis set
distance=[10.0]	Interatomic distance
do i=1,#distance r(i)=distance(i)	Allow various distance
{rhf; WF,44,1,2;}	RHF calculation
{casscf; OCC,13,5,5,1;	CASSCF calculation-a^{3}F
WF,44,4,2; state,2 WF,44,3,2; state,2 WF,44,2,2; state,2 WF,44,1,2; state,1}	wavefunction of a^{3}F number of electrons, symmetry, and spin
{mrci;OCC,13,5,5,1;WF,44,4,2;save,3042.1;state,2;noexc} {mrci;OCC,13,5,5,1;WF,44,3,2;save,3032.1;state,2;noexc} {mrci;OCC,13,5,5,1;WF,44,2,2;save,3022.1;state,2;noexc} {mrci;OCC,13,5,5,1;WF,44,1,2;save,3012.1;state,1;noexc}	save CASSCF (a^{3}F) wavefunctions by MRCI noexc: No excitation
{mrci;OCC,13,5,5,1;WF,44,4,2;save,4042.1;state,3} E(1)=energy(1) E_Q(1)=energd0(1) E(2)=energy(2) E_Q(2)=energd0(2) E(13)=energy(3) E_Q(13)=energd0(3) {mrci;OCC,13,5,5,1;WF,44,3,2;save,4032.1;state,3} E(3)=energy(1) E_Q(3)=energd0(1) E(4)=energy(2)	MRCI calculations for same spin multiplicity states: a^{3}F (7 states) a^{3}P (7 states)

```
E_Q(4)=energd0(2)
E(14)=energy(3)
E_Q(14)=energd0(3)
{mrci;OCC,13,5,5,1;WF,44,2,2;save,4022.1;state,3}
E(5)=energy(1)
E_Q(5)=energd0(1)
E(6)=energy(2)
E_Q(6)=energd0(2)
E(15)=energy(3)
E_Q(15)=energd0(3)
{mrci;OCC,13,5,5,1;WF,44,1,2;save,4012.1;state,1}
E(7)=energy(1)
E_Q(7)=energd0(1)
```

MRCI calculations for same spin multiplicity states: a^1D (5 states)

```
{mrci;OCC,13,5,5,1;WF,44,4,0;save,4040.1;state,1}
E(8)=energy(1)
E_Q(8)=energd0(1)
{mrci;OCC,13,5,5,1;WF,44,3,0;save,4030.1;state,1}
E(9)=energy(1)
E_Q(9)=energd0(1)
{mrci;OCC,13,5,5,1;WF,44,2,0;save,4020.1;state,1}
E(10)=energy(1)
E_Q(10)=energd0(1)
{mrci;OCC,13,5,5,1;WF,44,1,0;save,4010.1;state,2}
E(11)=energy(1)
E_Q(11)=energd0(1)
E(12)=energy(2)
E_Q(12)=energd0(2)
```

SOC calculation

```
lsint
text,a3F,a1D,a3P states, mrci
{mrci;hlsmat,ls,4042.1,4032.1,4022.1,4012.1,4040.1,4030.1,
4020.1,4010.1}
enddo
```

Make a Table for the final results

```
{table,sym,E,E_Q,
head, Symmetry,MRCI,MRCI+Q,
save, CoAr_d8_DKH_soc.tab,
title, MRCI calc of CoAr cation for d8 configuration
sort,1,2,3}
---
```

Appendix 2

The sample input file of MREOM-T|SXD/Def2-TZVPPD calculation on electronic states of $Co^{+}(d^{8})\cdot He$ at a 10Å interatomic distance via ACESII program

Co cation with He	Title
Co He 1 R R=10	Z-matrices
*ACES2(CALC=CCSD, REF=UHF, BASIS=Def2-TZVPPD, DKH_ORDER=-1, DAMP_TYPE=DAVIDSON OCCUPATION=8-3-3-1/6-3-3-1	Method: CCSD Reference: UHF Basis set DKH relative effect Davidson correction Orbital occupation
UNO_REF=ON,UNO_MULT=1, UNO_CHARGE=0	use UHF orbitals but to create equal α, β orbitals
QRHF_G=-2/-3/-4 MAKERHF=ON, BRUECKNER=ON IP_CALC=IP_EOMCC,IP_SYM=2-1-1-1 DIP_CALC=EOMCC,DIP_SYM=1-0-0-0)	Change the active space

*mrcc_gen closed_shell_calc=cas_ic_mrcc mcscf_calc=none aaii_shift=0.2 ai_shift=0.2 amii_shift=0.2 *true_mrcc read_mos=on *datta_mrcc datta_project=off precontract_Taa=off mreom_degen=on project_amii_d=off project_amii_x=off project_amii_a=off datta_include_U=off datta_separate_TS=on datta_T_only=off demel_ic_MRCC=on full_ic_MRCC=on datta_exclude_S_one_active=off datta_exclude_S_all_active=on datta_exclude_S_d_active=off final_ic_mrcis=on	
*gtci_final include_hh=on include_1h=on include_1p=on include_ph=on include_phh=off	Define the diagonalization space: 2h, 1h, 1p, 1p1h excitations
nele=8 nsymtype=8 multiplicity=8 3 3 3 3 1 1 1 1 state_irrep=8 1 2 3 4 1 2 3 4 states_per_symtype=8 1 3 3 3 5 3 3 3	Number of electrons (8) in active space (3d^{8}) MREOM-T|SXD approach on the ^{3}F and ^{1}D states of $Co^{+}(d^{8})\cdot He$

CASSCF reference: ^{3}F

1+2+2+2=7 states

```
*gtci
nele=8
nsymtype=4
multiplicity=4
3 3 3 3
state_irrep=4
1 2 3 4
states_per_symtype=4
1 2 2 2
*end
```

Appendix 3

The sample input file of MREOM-T|T$^+$|SXD/Def2-TZVPPD calculation on electronic states of $Co^+(d^8) \cdot Ar$ at a 10Å interatomic distance via ORCA program

Basis set: def2-TZVPP
DKH relative effect

```
!MREOM def2-TZVPP DKH
```

Z-matrices

```
* xyz 1 5
 Co      0.000000      0.000000      0.000000
 Ar      0.000000      0.000000      1.000000
end
```

Add diffusion function

```
%basis
 AddGTO 27
  P 1
   1 0.03481105658700         1.00000000000000
 end
 AddGTO 18
  S 1
   1 0.073732186754 1.0000000
  P 1
   1 0.041779128551 1.0000000
  D 1
   1 0.12039311859 1.0000000
 end
```

```
!MOREAD
%moinp "orca.gbw"
%method frozencore fc_ewin end
%casscf
 nel 8
 norb 6
 mult 5, 3
 nroots 7, 7
 gtol 1e-9
 etol 1e-10
 shiftup 2
 shiftdn 2
 switchstep nr
end
```

State-average CASSCF:
$3d^8$: a3F
$3d^7 4s^1$: b3F

```
 %mdci
MaxCoreWork 50000
MaxCoreIntAmp 55000
ewin -6, 4000
MaxIter 300
STol 1e-9
TCutInt 1e-14
Hbar_Symmetry = Vertex
LevelShift 0
End
%mrci
  maxmemint 55000
  maxmemvec 55000
  ewin -6, 4000
  MaxIter 200
  citype mrci
  davidsonopt 0
  tsel 0 tpre 0 tnat 0
  Etol 1e-8 Rtol 1e-8
  RejectInvalidRefs false
```

```
newblock 5 *
  nroots 10
  excitations none
  flags[is ] 1
  flags[sa ] 1
  flags[ia ] 0
  flags[ijss] 1
  flags[ijsa] 0
  refs cas(8,6) end
  end
```

MREOM-T|T$^+$|SXdcalculation: quintet states

Number of states: 10 (a^{5}F, a^{5}P)

The diagonalization space:
1p, 1h, 2h

```
newblock 3 *
  nroots 48
  excitations none
  flags[is ] 1
  flags[sa ] 1
  flags[ia ] 0
  flags[ijss] 1
  flags[ijsa] 0
  refs cas(8,6) end
  end
```

MREOM-T|T$^+$|SXD calculation: triplet states

Number of states: 10 (a^{3}F, b^{3}F, a^{3}P, a^{3}G, b^{3}P, c^{3}P, a^{3}H, a^{3}D)

The diagonalization space:
1p, 1h, 2h

```
newblock 1 *
  nroots 42
  excitations none
  flags[is ] 1
  flags[sa ] 1
  flags[ia ] 0
  flags[ijss] 1
  flags[ijsa] 0
  refs cas(8,6) end
  end
```

MREOM-T|T$^+$|SXD calculation: singlet states

Number of states: 10 (a^{1}D, a^{1}G, b^{1}G, a^{1}P, a^{1}H, b^{1}D)

The diagonalization space:
1p, 1h, 2h

```
soc
   DoSOC true
  end
end
```

include the SOC contribution

Appendix 4

Experiment- and computation-vibrational energies for A, B, and C excited states of $Co^+ \cdot Ar$

Vibration	Transition Frequency (eV)					
	A Exp	A Calc	B Exp	B Calc	C Exp	C Calc
0		1.572		1.524	1.803	1.690
1	1.739	1.591		1.540	1.824	1.708
2	1.754	1.608		1.556	1.844	1.725
3	1.769	1.622		1.572	1.864	1.741
4	1.782	1.635		1.587	1.882	1.757
5	1.796	1.646		1.601	1.900	1.771
6	1.807	1.656	1.745	1.615	1.917	1.785
7	1.820	1.665	1.757	1.627	1.933	1.798
8	1.831	1.673	1.767	1.639	1.949	1.811
9		1.682	1.778	1.650	1.964	1.822
10		1.690	1.788	1.660	1.978	1.833
11		1.697	1.797	1.670	1.992	1.843
12		1.705	1.806	1.678	2.004	1.853
13		1.711	1.815	1.686	2.017	1.861
14		1.718	1.823	1.693	2.028	1.870
15		1.723	1.830	1.699	2.039	1.877
16		1.729	1.837	1.705	2.049	1.884
17		1.734	1.844	1.711	2.059	1.890
18		1.738	1.851	1.716	2.068	1.896
19		1.742	1.857	1.720	2.078	1.901
20		1.745	1.863	1.725	2.084	1.906
21		1.749	1.868	1.729	2.091	1.911
22		1.752	1.873	1.732	2.098	1.914
23		1.754	1.877	1.735	2.104	1.918
24		1.756	1.881	1.738	2.110	1.921
25	1.921	1.758	1.885	1.741	2.115	1.923
26	1.926	1.760	1.889	1.743	2.119	1.926
27	1.929	1.761	1.892	1.745	2.124	1.928
28	1.933	1.763	1.895	1.747	2.127	1.930
29	1.936	1.764	1.897	1.748	2.131	1.931
30	1.938	1.765	1.899	1.750	2.134	1.933
31	1.941	1.766	1.901	1.751	2.136	1.934
32	1.943	1.766	1.903	1.752	2.139	1.935
33	1.944	1.767	1.905	1.753	2.141	1.936
34	1.946	1.767	1.906	1.753	2.143	1.936
35	1.947		1.907	1.754	2.144	1.937
36			1.908	1.755	2.146	1.938
37					2.147	
38					2.148	
39					2.149	
40					2.150	
41					2.150	
42					2.151	

43	2.151
44	2.151

Experiment- and computation-vibrational index to the 4/3 power for A, B, and C excited states of $Co^+ + Ar$

Vibration levels	**Transition Frequency (eV)**					
	A_Exp	A_Calc	B_Exp	B_Calc	C_Exp	C_Calc
0		0.097		0.081	0.116	0.091
1	0.075	0.088		0.084	0.111	0.088
2	0.070	0.070		0.075	0.104	0.083
3	0.065	0.059		0.075	0.098	0.077
4	0.067	0.050		0.070	0.093	0.072
5	0.049	0.042		0.064	0.088	0.067
6	0.057	0.038	0.050	0.059	0.083	0.062
7	0.050	0.036	0.048	0.054	0.078	0.057
8		0.034	0.045	0.049	0.073	0.053
9		0.032	0.043	0.045	0.069	0.048
10		0.030	0.040	0.040	0.065	0.044
11		0.028	0.038	0.035	0.061	0.040
12		0.026	0.035	0.031	0.056	0.036
13		0.024	0.032	0.027	0.052	0.033
14		0.021	0.030	0.024	0.048	0.029
15		0.019	0.028	0.021	0.044	0.026
16		0.016	0.026	0.019	0.042	0.023
17		0.014	0.024	0.018	0.037	0.021
18		0.012	0.022	0.016	0.048	0.019
19		0.011	0.021	0.014	0.020	0.016
20		0.010	0.018	0.012	0.028	0.014
21		0.008	0.016	0.011	0.025	0.012
22		0.007	0.015	0.009	0.022	0.010
23		0.006	0.014	0.008	0.020	0.009
24		0.005	0.012	0.007	0.018	0.008
25	0.014	0.004	0.011	0.006	0.015	0.006
26	0.011	0.003	0.009	0.005	0.014	0.005
27	0.010	0.003	0.008	0.004	0.012	0.005
28	0.009	0.002	0.007	0.004	0.010	0.004
29	0.007	0.002	0.006	0.003	0.009	0.003
30	0.006	0.001	0.005	0.002	0.007	0.002
31	0.005	0.001	0.004	0.002	0.006	0.002
32	0.004	0.001	0.004	0.002	0.005	0.002
33		0.001	0.003	0.001	0.005	0.001
34		0.001	0.002	0.001	0.004	0.001

35	0.002	0.001	0.003	0.001
36	0.002	0.000	0.002	0.000
37			0.002	
38			0.002	
39			0.001	
40			0.001	
41			0.001	
42			0.001	
43			0.000	

Appendix 5

The potential energy curves of $Co^{+} \cdot Ar$ as calculated by MREOM-T|T^{+}|SXD/Def2-TZVPPD with counterpoise correction by using the ORCA program

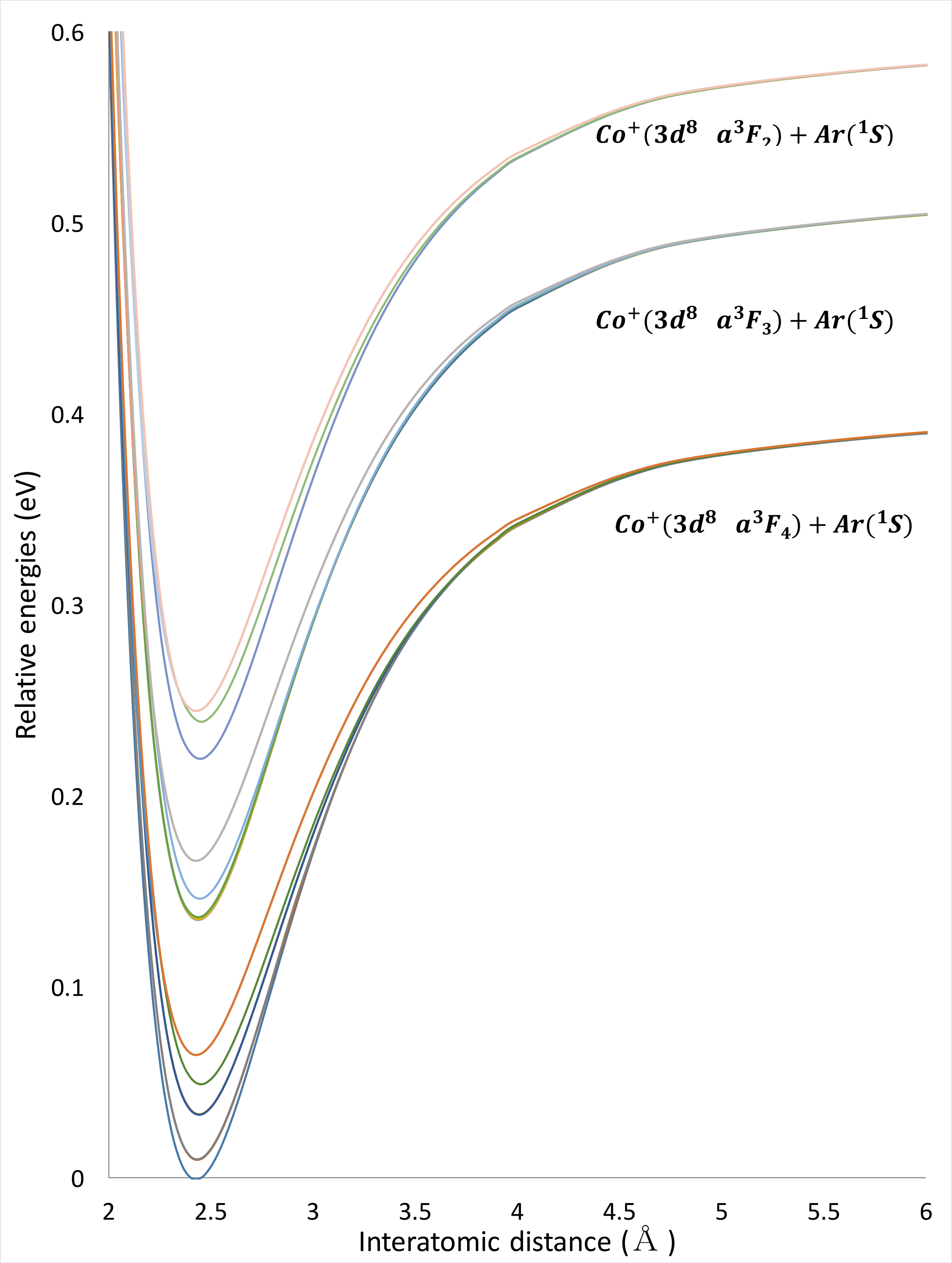
0.6
0.5
0.4
0.3
0.2
0.1
0
Relative energies (eV)
2
2.5
3
3.5
4
4.5
5
5.5
6
Interatomic distance (Å)
$Co^+(3d^8\ \ a^3F_2) + Ar(^1S)$
$Co^+(3d^8\ \ a^3F_3) + Ar(^1S)$
$Co^+(3d^8\ \ a^3F_4) + Ar(^1S)$

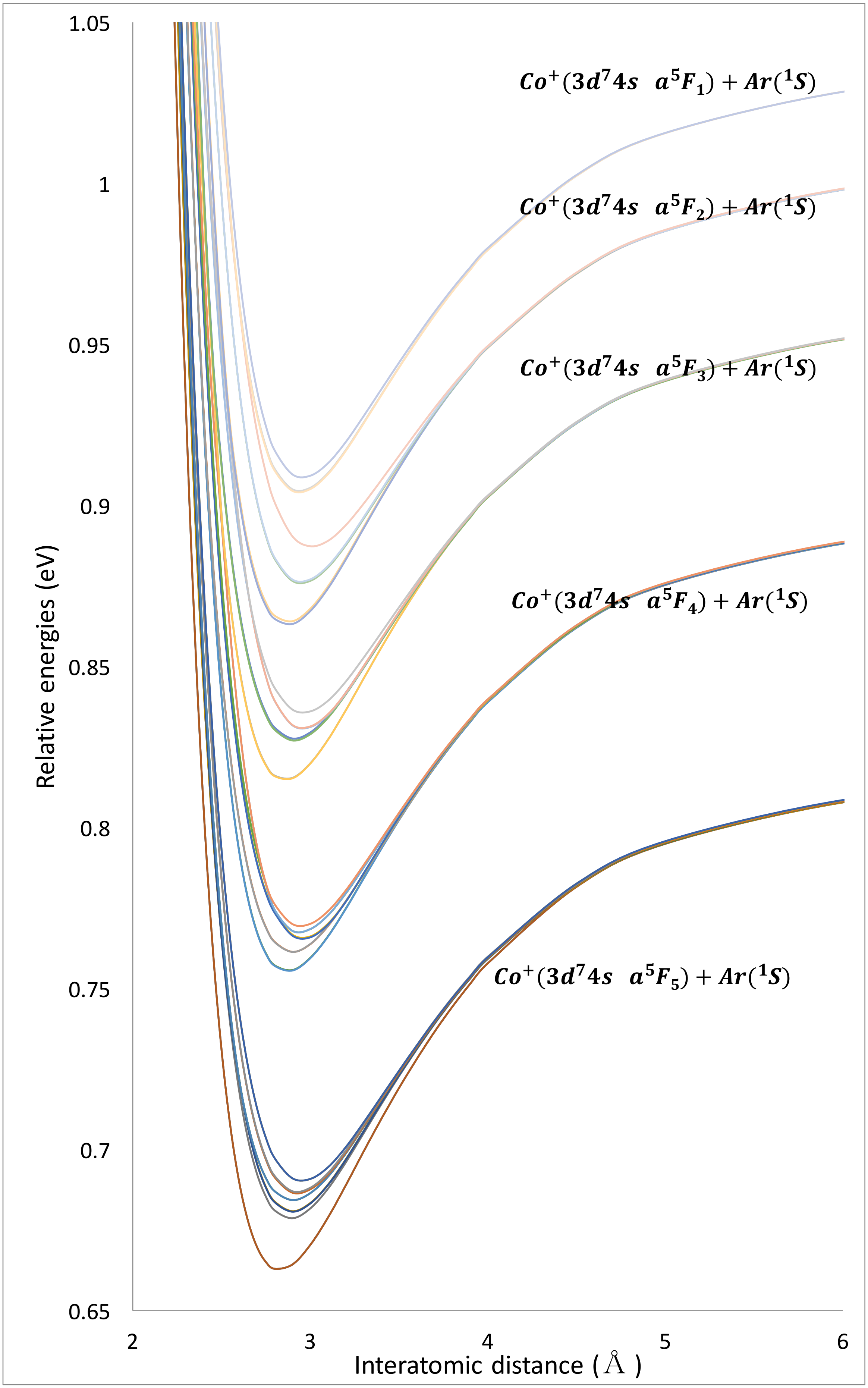

$Co^+(3d^7 4s\ \ a^5F_1) + Ar(^1S)$
$Co^+(3d^7 4s\ \ a^5F_2) + Ar(^1S)$
$Co^+(3d^7 4s\ \ a^5F_3) + Ar(^1S)$
$Co^+(3d^7 4s\ \ a^5F_4) + Ar(^1S)$
$Co^+(3d^7 4s\ \ a^5F_5) + Ar(^1S)$
Relative energies (eV)
1.05
1
0.95
0.9
0.85
0.8
0.75
0.7
0.65
2
3
4
5
6
Interatomic distance (Å)

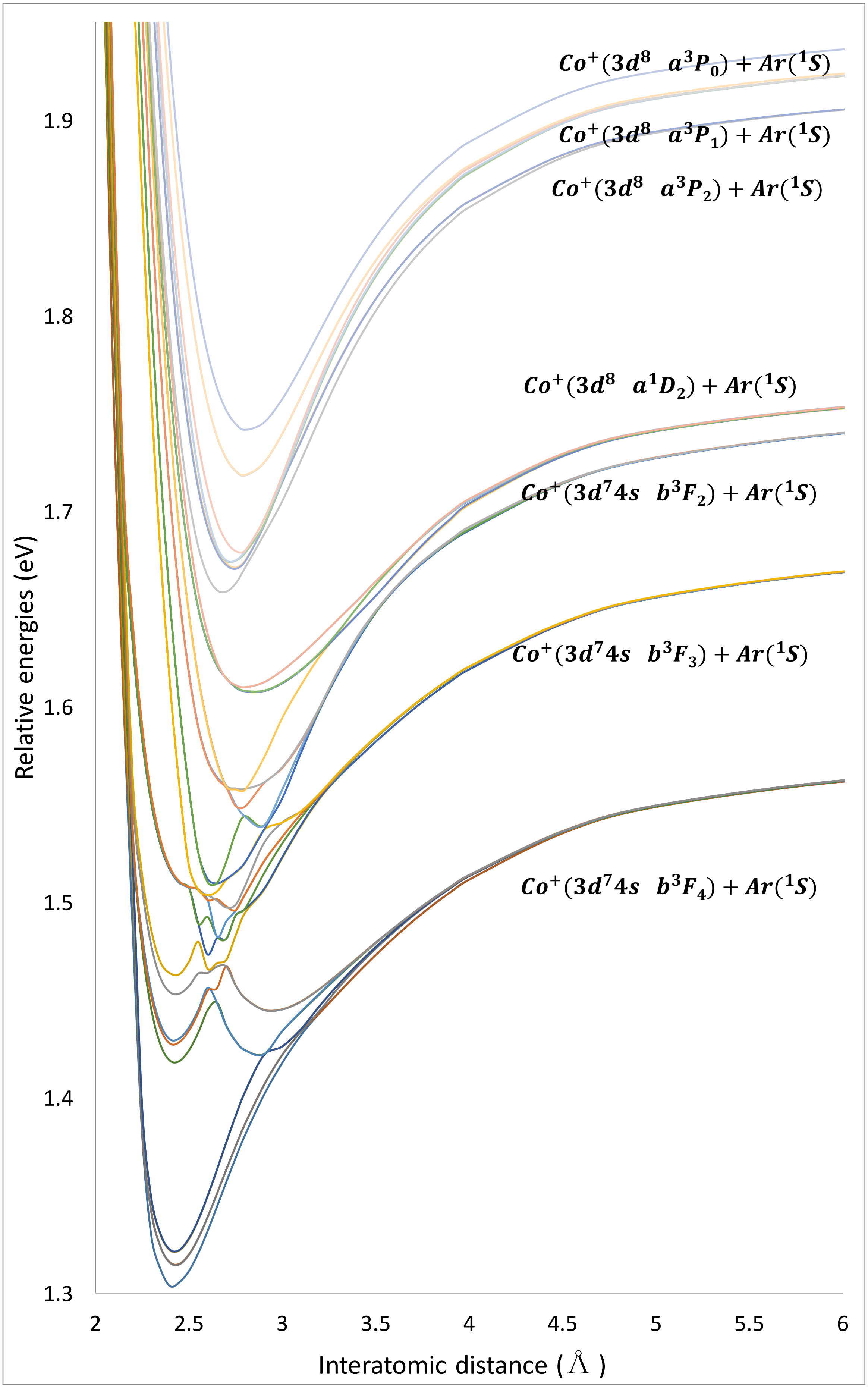
$Co^+(3d^8\ \ a^3P_0) + Ar(^1S)$
$Co^+(3d^8\ \ a^3P_1) + Ar(^1S)$
$Co^+(3d^8\ \ a^3P_2) + Ar(^1S)$
$Co^+(3d^8\ \ a^1D_2) + Ar(^1S)$
$Co^+(3d^74s\ \ b^3F_2) + Ar(^1S)$
$Co^+(3d^74s\ \ b^3F_3) + Ar(^1S)$
$Co^+(3d^74s\ \ b^3F_4) + Ar(^1S)$
Relative energies (eV)
1.9
1.8
1.7
1.6
1.5
1.4
1.3
2
2.5
3
3.5
4
4.5
5
5.5
6
Interatomic distance (Å)

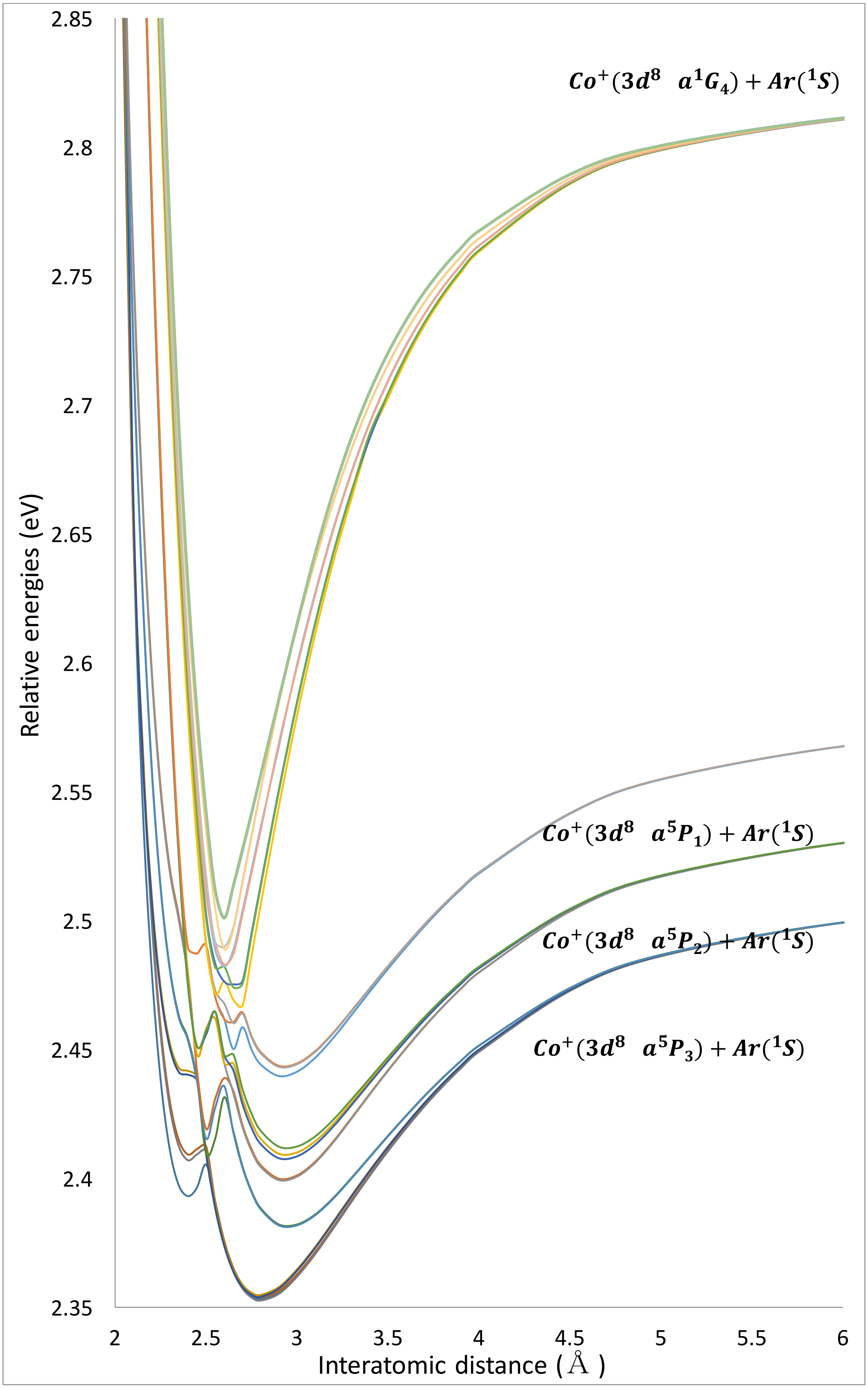
$Co^+(3d^8\ \ a^1G_4) + Ar(^1S)$
$Co^+(3d^8\ \ a^5P_1) + Ar(^1S)$
$Co^+(3d^8\ \ a^5P_2) + Ar(^1S)$
$Co^+(3d^8\ \ a^5P_3) + Ar(^1S)$
Relative energies (eV)
2.85
2.8
2.75
2.7
2.65
2.6
2.55
2.5
2.45
2.4
2.35
2
2.5
3
3.5
4
4.5
5
5.5
6
Interatomic distance (Å)

Appendix 6

STO-3G: each STO is expanded in three Gaussian primitives.

6-31G: each inner shell STO is expanded in 6 gaussians and each valance shell STO split into inner and outer parts described by 3 and 1 gaussian primitives, respectively.

6-31G*: the 6-31G basis set augmented with 6 d-type gaussian primitives on each (Z>2) atom, to permit polarization.

6-31G**: the 6-31G* basis set augmented with a set of gaussian p-type functions on H and He atoms to permit more polarization.

6-31G+*: the 6-31G* basis set augmented with a set of diffuse s- and p-type gaussian functions on each heavy atom, to permit representation of diffuse electronic distribution.

cc-pVnZ, n-D,T,Q,5: correlation consistent polarized valance n-zeta gaussian basis sets. The inner shell STOs is expanded by single contract gaussian functions while the valance STOs are described by n contracted gaussian functions. The polarization functions are added.

Aug-cc-pVnZ: the cc-pVnZ basis sets augmented with a set of diffuse primitive gaussian functions.

Def2-TZVPPD: Def2-XYZ are new sets of basis functions. The def2 basis sets for 5p and 6p block elements are designed for small core ECPs. TZVPPD means the valance triple zeta plus doubly-polarized and diffuse functions.